

2D Acoustic Full Waveform Inversion of the Asse II Mine Model

Master Thesis
by

Alexander Potthast

at
Geophysical Institute (GPI)

Reviewer:	Professor Thomas Bohlen
Second Reviewer:	Professor Joachim Ritter
Advisor:	Dr. Thomas Hertweck

Processing Time: 31.03.2023 - 31.03.2024

Declaration of Self-reliance

I certify that I have written this paper independently and have not used any sources and aids other than those indicated, that I have marked as such the passages taken over verbatim or as regards content and the KIT Statutes for the Safeguarding of Good Scientific Practice in the valid version of 17.05.2010.

Karlsruhe, 31.03.2024, _____
Alexander Potthast

Approved as a viewing copy by

Karlsruhe, 31.03.2024, _____
Professor Thomas Bohlen

Abstract

The Asse II is a salt mine in the district of Wolfenbüttel that lies within the Asse Hesseberg Hill. In the 1960s, the German federal government bought the mine and converted it into a nuclear waste storage facility. The salt chambers were filled with radioactive waste and intended to be used as a storage facility for millions of years. This idea of progressive waste disposal became a nightmare when ground water surrounding the geologic overburden of the mine began leaking into it. The widespread implications and potential damage of the water leaking into the chambers of the mine has caused the German government to devote significant resources into the mitigation of any potential escalation of the situation. The Bundesgesellschaft für Endlagerung (BGE), a German federal company responsible for research and extraction of the waste, in collaboration with the Karlsruhe Institute of Technology (KIT)'s Geophysics Institute, has preformed numerical modelling and geological research to gain insight on the geologic structure that makes up the Asse Heeseberg Hill.

Using data provided by BGE, a subsurface model referred to in this thesis as the Asse II Mine Model was developed by (Mendez, 2024). To test the integrity and potential limits of inverse modelling with the Asse II Mine Model, 2D acoustic full waveform inversion (FWI) of the Asse II Mine Model was preformed in this thesis. FWI, as the name implies, is an inverse modelling technique that utilizes the comparison of complete seismic waveforms to recreate observed synthetic data or observed field data. All forward and inverse modelling was preformed by discretizing the p-wave velocity values on a 2D numerical grid. After it was clear that forward modelling could be accurately preformed on the model, attempts at inverse modelling began. All inverse modelling done in this thesis was done with FWI. Detailed inversion parameters tests were made in order to obtain the best possible inversion models. These parameters, among others, included gradient method, step length, LNORM, tapering, frequency filter, and abort criteria.

Once these parameters were set and able to get an accurate result other parameters such as starting model, shot frequency, acquisition geometry, and time windowing were tested. After combining these parameters and running numerous inversions, accurate inversion were obtained. Thus the question, "could acoustic 2D full waveform inversion could be used to successfully and accurately reconstruct the Asse II Mine Model?" was confirmed. The results of the inversions are indicative of the successful recreation of the observed synthetic model, and potential for further application of acoustic numerical modelling to 3D scenarios and even field data.

Contents

1	Introduction	1
1.1	History of Asse	1
1.1.1	Future of Asse II	3
1.2	Geology of the Region	4
1.2.1	Geologic History	5
1.2.2	Asse-Heeseberg Geology	6
1.3	Goal of Thesis	7
1.4	Outline	7
2	Theoretical Background	9
2.1	Seismic wave propagation	9
2.1.1	The equation of motion	9
2.1.2	The stress-strain relation	9
2.1.3	The Acoustic Case	10
2.2	Numerical Modelling	12
2.2.1	Discretizing the Acoustic Wave Equation	14
2.2.4	Initial and boundary conditions	15
2.2.5	Grid Dispersion	15
2.2.6	Courant Instability	16
2.3	Inverse Theory	17
2.3.1	The Inverse Method	18
2.3.2	Misfit Definition	19
2.3.3	Adjoint Gradient	20
2.3.3	Adjoint Gradient for the Acoustic Case	22
2.3.4	Gradient Preconditioning	22
2.3.5	Step Length Estimation	23
3	Forward Modelling	25
3.1	Observed Model	25
3.1.1	Model Parameters	25
3.1.2	Numerical Tests	28
3.2	Starting Model	30
3.2.1	Smoothing Workflow	30
3.2.2	Cycle Skipping Analysis	31
4	Inverse Modeling	37
4.1	Inversion Parameters	37
4.2	Checkerboard Test	38

4.3 Further Inversion Parameters	39
4.3.1 Different Frequency Tests	39
4.3.2 Different Starting Models	42
4.3.3 Different Acquisition Geometries	42
4.3.4 Inversions with Time Windowing	47
4.4 Comparison to Observed Model	50
5 Conclusion & Outlook	59
6 Acknowledgements	61
Appendix	66

List of Figures

1.1	Asse II Mine	2
1.2	Geologic setting of Subhercynian Basin	3
1.3	Harz Uplift and Subhercynian Basin	4
1.4	Asse Mine Cross Section	5
1.5	3D Seismic Survey Area	6
2.1	Finite Difference Grid Space Discretization	13
2.2	Finite Difference Grid Time Discretization	13
2.3	Finite Difference Boundaries	15
2.4	Full Waveform Inversion Workflow	17
2.5	Example of Misfit Functions	20
2.6	Forward and Adjoint Modelling	23
3.1	Geologic Layers Surrounding Asse II Mine	26
3.2	Vp Observed Model	29
3.3	Forward Modelling Observed Synthetic Shot	29
3.4	Cycle Skip Analysis Figure 1	32
3.5	Cycle Skip Analysis Figure 2	33
3.6	Sigma Comparisons	34
3.7	Comparison of Observed and Starting Vp Model	35
3.8	Observed Wavefield	36
3.9	Sigma 100 Wavefield	36
4.1	Checker Board Test	40
4.2	Source Frequency Comparison	41
4.3	Sigma Comparison Plots	43
4.4	Shot Geometry Comparison	44
4.5	Data Fit Comparison	45
4.6	Sigma 200 Model Shot Geometry Comparison	46
4.7	Time Windowing Example	47
4.8	Residual of Without and With Time Window Inversion	48
4.9	Residual of Without and With Time Window Inversion	49
4.10	Comparison between Observed Model and Sigma 100 Inversion	52
4.11	Comparison between Observed Model and Sigma 200 Inversion	53
4.12	Comparison between Observed Model and Time Window Inversion	54
4.13	Observed vs. InverseionTraces	55
4.14	Trace 301: Observed vs Inversion	56
4.15	Trace 350: Observed vs Inversion	56
4.16	Observed vs. Sigma 200 Inversion Traces	57
4.17	Trace 350: Observed vs Sigma 200 Inversion	58

A.1	Observed Rho Model	66
A.2	Synthetic and Starting Model Comparison	67
A.3	Histogram Comparison of Inversion of Different Starting Models . . .	68
A.4	All Shot Geometries	69
A.5	All Shot Geometries with Time Window	70
A.6	Without and With Time Window Inversion Comparison	71
A.7	Sigma 300 Acquisition Geometry Comparison	72

List of Tables

2.1	FD Order	16
3.1	Asse II Model v_p Values	26
3.2	Acquisition Parameters	27
3.3	Source Geometry	28
4.1	Full Waveform Inversion Parameters	38
4.2	Relative Model Error	51

1. Introduction

Safe deposition and long term storage of radioactive waste is an imperative part of any past and future utilization of nuclear energy. While nuclear power in Germany has seen nationwide decommission because of its potential environmental and humanitarian impact, the energy source had widespread use in Germany until early 2023 (Gauto, 2023). The extended and proficient use throughout the last 60 years begs the question, 'where should the produced hazardous waste be stored?' Today, the overwhelming consensus is that repository sites with storage capabilities of at least one million years should be used (Bundesministerium für Umwelt, Naturschutz, nukleare Sicherheit und Verbraucherschutz, 2013). However, this is a new development that is still currently unavailable. In the mid to late 20th century, the consensus among German scientists and politicians was that salt mines were the most appropriate candidates for the long term storage of nuclear waste. This is one of the reasons as to why Asse II was selected for active storage in the 1960s. However, due to structural deficiencies that in hindsight may have been preventable, the Asse II has become an expensive headache and safety concern for the German government. The Asse II mine lies within the Asse-Heeseberg Hill in Lower Saxony, south east of the district of Wolfenbüttel. The hill, oriented in the northwest/southeast direction, is about 8km long, is 234 m above sea level (Sortan, 2022), and lies between the Harz Mountains and Flechtingen basement high of the Subhercynian Cretaceous Basin. The Asse-Heeseberg hill is constructed of a salt diapir covered in sedimentary rocks from the Mesozoic and Cenozoic epochs that also fills the SCB (Brandes et al., 2013). Surrounding the hill, are various municipalities which either intersect the hill or lie on its outskirts. The entrance to the mine is located within the eastern part of the hill, within the Remlingen-Semmensted municipality. Part of the facility of the mine is shown in figure 1.1.

1.1 History of Asse

Public and political opinion of nuclear energy and waste in Germany in the 20th and 21st century has been largely impacted by Asse II. Since the hopeful inception of the facility, the mine has become a tremendous burden for the German government, and significant safety concern for the people living in the region. Industrial development of the area began in 1899 when Asse I, the first shaft of the mine, was built. However, uncontrollable flooding caused the mine to close (Szymaniak and Shaefer, 2002). To replace Asse I, the planning for Asse II began. In 1916, the mine began production of salt and potash which would continue until the mine was bought by the German federal government in 1964. With the mine under its operation, the German government assigned the Association of Radiation Research to use Asse II to store and run tests on nuclear waste. From 1964 to 1967 accommodations for the storage of radioactive material were made, and in 1967, operation began. By the time the storage of the



Figure 1.1: An image of the eastern flank of the Asse hill. The facility of the mine can be seen on the hillside. This image was taken from (Bundesamt für Strahlenschutz, 2016).

low to intermediate radioactive waste had ended, 47 000 m³ or ~125 000 drums of waste had been placed into the mine.

During the period of alteration into a storage facility, attempts to maximize storage capabilities caused stability issues on the south western flank of the mine. These stability issues become apparent in 1988 when water began to intrude the facility. (Trela et al., 2018). In hopes to stop the water and stabilize the walls of the chambers, cavities of the southern flank were filled with salt. These attempts continued from 1995 to 2004, but ultimately proved to be ineffective. Currently the mine has about 12.5 m³ of water flowing in every day (Pollok et al., 2018). This issue was kept secret from the public until 2008, twenty years after the intrusion of water had begun. In 2009, Asse II was taken under nuclear law and operation was given to the Federal Office for Radiation Protection (BfS) with the task to decommission Asse II as quickly and as safely as possible. In 2010, after reviewing possible decommission and retrieval methods, BfS decided that the safest option for extracting the waste was to store it in a new repository (Geckeis, 2017). This plan was approved by the German Parliament in 2013 by passing the *Gesetz zur Beschleunigung der Rückholung radioaktiver Abfälle und der Stilllegung der Schachtanlage Asse II* or *Lex Asse*. Later that year legislation was passed to begin the search for a repository of where the waste could be stored. This was the *Gesetz zur Suche und Auswahl eines Standortes für ein Endlager für Wärme entwickelnde radioaktive Abfälle* (Bundesministerium für Umwelt, Naturschutz, nukleare Sicherheit und Verbraucherschutz, 2013). In 2017, to improve oversight, operation and regulation of the mine was split into two different roles. The role of operator of the mine would be assigned to the newly founded *Bundesgesellschaft für Endlagerung (BGE)*. While the BfS would take over the role of regulator. Future decisions would be made by BGE, assessed by BfS, and set into law by the German parliament (Geckeis, 2017).

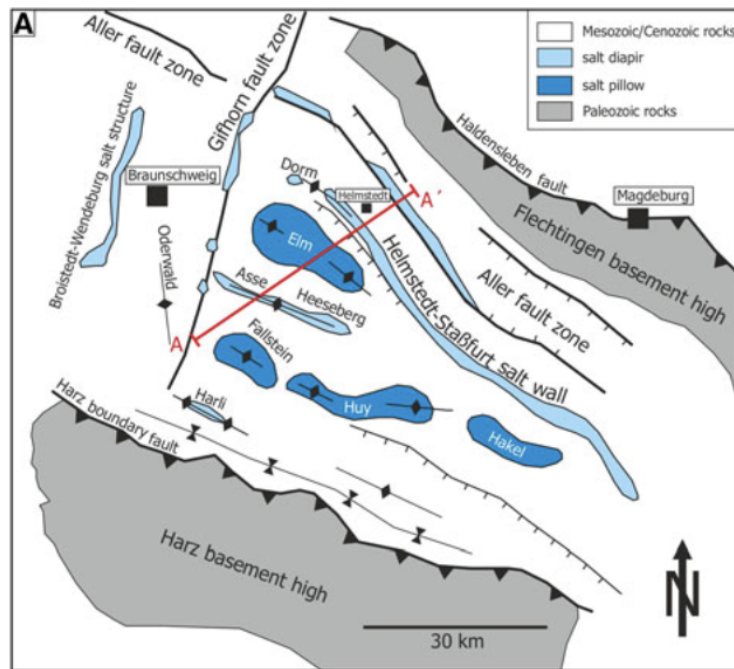


Figure 1.2: Geologic setting of the Subhercynian Basin. The Asse-Heeseberg structure is located centrally within the basin, and is surrounded by several other salt structures. The cross section A-A' is not relevant for this thesis. This image is part of a larger figure taken from (Brandes et al., 2013).

The *Bundesanstalt für Geowissenschaften und Rohstoffe* (BGR) has been conducting geophysical and geological surveys of the Asse II mine and its surrounding structure on the behalf of BGE since 2014. The data collected from these surveys is set to compliment and replace existing data of the area, and is set to be used to create a high resolution 3D geological model that will provide insight into the structure of the chambers of the mine and the surrounding salt. This model is set to be complete in 2025, and will be an effective tool for determining structural areas appropriate for building necessary infrastructure for the extraction of the nuclear waste. The geophysical data acquired during this period is planned to help with imaging areas where work is currently being done, exploration is set to take place, and new shafts will be made. This in conjunction with geologic data obtained from the interpretation of drill cores from boreholes is planned to provide a thorough overview of the mine. BGR will also be responsible for quality checks and processing of the obtained data. (Bundesanstalt für Geowissenschaften und Rohstoffe, 2014)

1.1.1 Future of Asse II

Several large steps still lie ahead of safely decommissioning Asse II. Before extraction of the nuclear waste can be done, a thorough understanding of the overburden and salt structure is needed. While the thickness of strata, geologic boundaries, and layout of the mine have been recorded by numerous studies, these properties must be reconfirmed in order to have a confident understanding of the geology. The importance of this is due to the need for the excavation of salt during the retrieval process (Bundesgesellschaft für Endlagerung, 2023). New mine shafts must be built to accommodate the outgoing nuclear waste, and new tunnels will be dug in order to

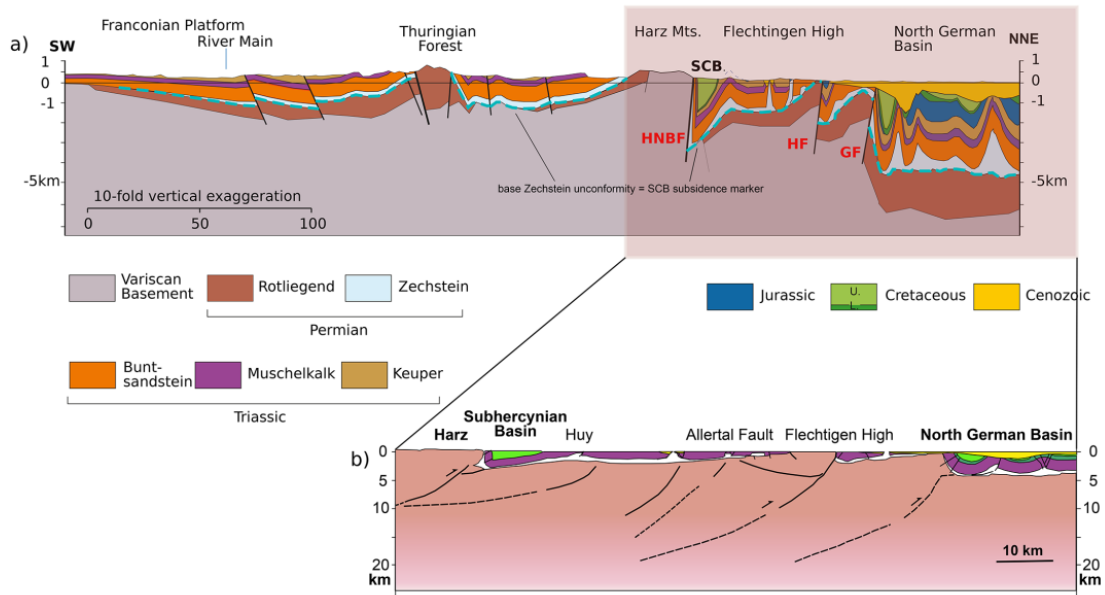


Figure 1.3: A cross section of the geologic region that encompasses the Harz Uplift, Subhercynian Basin, and the surrounding area. The layers of sediment from corresponding geologic epochs are shown as well. This image is taken from (Hindle and Kley, 2021).

access hard to reach waste (Pollok et al., 2018). In order to get an understanding of the mine and its overburden, numerous types of surveys have and still need to be done. From 2019 to 2020, a rigorous 3D seismic survey in the region surrounding the mine was made by BGE. This 3D survey covered an area of 36.5 km² and used over 40 000 active receiver nodes. It was the largest active channel survey ever to have been conducted in Europe (Bundesgesellschaft für Endlagerung, 2023). The area of this survey is shown in figure 1.5. Additionally, a new repository for the recovered nuclear waste must be constructed. According to the legislation passed in 2013, this new repository will be able to fit and store low to intermediate radioactive waste for at least one million years. For the waste in the Asse II mine, the Konrad Repository in Salzgitter, Lower Saxony, has been licensed for this purpose. It is planned to be available for nuclear waste storage in 2027 (Bundesgesellschaft für Endlagerung, 2023). The beginning of the retrieval and transport of the Asse II nuclear waste is planned to commence in 2033.

1.2 Geology of the Region

The Asse II mine resides just outside of the Subhercynian Cretaceous Basin (SCB), a small basin southeast of the Lower Saxony Basin (Szymaniak and Shaefer, 2002). Both basins lie in the larger surrounding North German Basin, a part of the Central European Basin System (CEBS). To the southwest of the Asse-Heeseberg Hill and the SCB are the Harz Mountains, a section of the Rhenohercynian belt of the European Variscides called the Variscan Basement. It was thrust upwards along the Harz Northern Boundary Fault (HNBF) about 82-86 Ma (T. Voigt and H. Eynatten and H.-J. Franzke, 2004). The local region of the Asse the Hill and SCB can be seen in figure 1.2. The HNBF thrust fault played an important role in the North German Basin during intraplate deformation of the Late Cretaceous (K. Müller and U. Polom

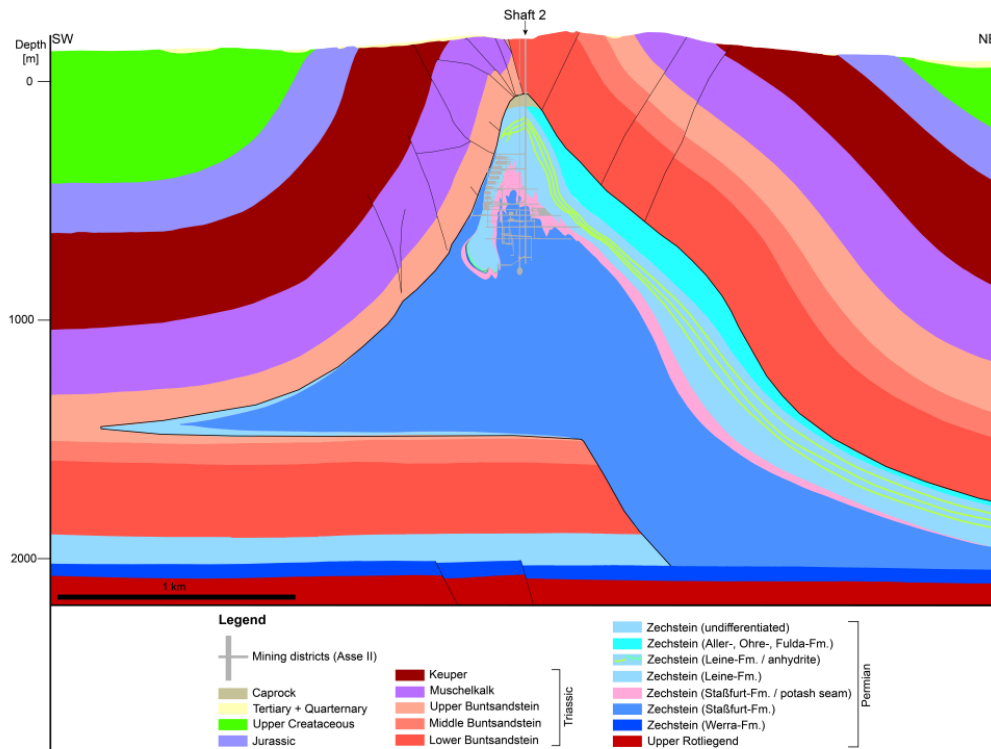


Figure 1.4: A cross section of the Asse II mine. Here the Zechstein formations as well as the overburden in the area can be clearly seen. The salt structure's clear wedge like shape that breaks the continuity of the Buntsandstein layers can be seen. This image was taken from (Pollok et al., 2018).

and J. Winsemann and H. Steffen and S. Tsukamoto and T. Günther and J. Igel and T. Spies and T. Lege and M. Frechen and H.-J. Franzke and C. Brandes, 2020). Today, it is a major fault zone in Central Europe. It is estimated to have a 4 km long vertical displacement, and plays a role in the crustal shortening in the Lower Saxony Basin (W. Voigt, 1910). In regards to sedimentation, the fault is also important as it is the depocenter of the SCB. Along it lies ~ 2.5 km worth of infill of the SCB. The Harz Mountains in conjunction with the Flechtingen basement high, an uplift northeast of Asse, surround the SCB and Asse hill (Brink, 2011). The basin itself is filled with thick Mesozoic cover that varies in a range of several hundred meters of thickness.

1.2.1 Geologic History

During the Permian, the entire area of the CEBS developed into a large continental depression, which lead to the development of a thick sequence of mobile Zechstein salt. This was followed by a sequence of rifting and subsidence during the Triassic that was eventually changed by a new regional stress regime of the late Triassic and early to mid Jurassic. The change in stress regime is what ultimately led to development of the Permian sub-basins, such as the SCB (Cacace et al., 2009). During the Late Cretaceous, a period of several compressional tectonic phases partially inverted the basin systems throughout the region (W. Voigt, 1910). Within the local region of the Asse hill and SCB, this compression affected the region by severely folding geologic layers and thrusting the Variscan Basement on the HNBF. Much of the deformation

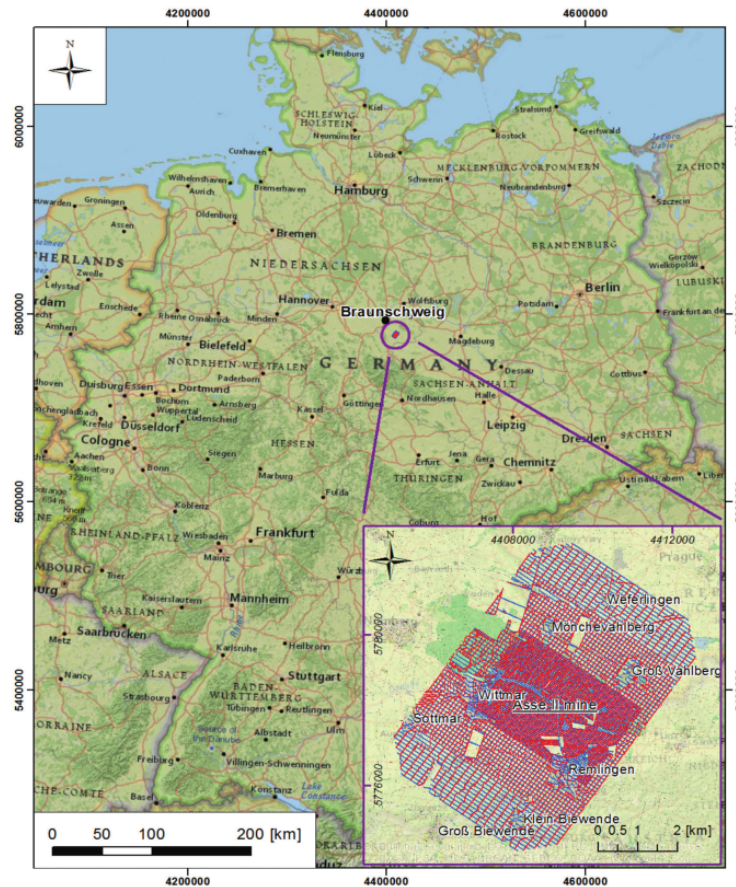


Figure 1.5: Survey area of the 2019-2020 3D seismic survey conducted by BGE. The location of the survey in Germany can be seen. A zoomed-in image shows the location in a regional context. This image was taken from (Trela et al., 2018).

that created the Harz Mountains and the Asse-Heeseberg salt structure, occurred during three main tectonic phases within the SCB. These were the Peine in the early Campanian, Wernigerode in the Late Santonian, and Ilsede in the Late Turonian and Early Coniacian (Mortimore and Pomerol, 1997). A cross section of the region in figure 1.3 shows evidence of compression of the Mesozoic layers beneath the SCB (Hindle and Kley, 2021). After the period of basin inversion, the Cenozoic saw rather strong instances of regional subsidence (Cacace et al., 2009).

1.2.2 Asse-Heeseberg Geology

The Asse-Heeseberg salt structure as well as other salt structures in the region, are composed of rock salt that comes from Zechstein evaporite group deposited during the Late Permian. The Asse salt structure is composed predominantly of the Staßfurt-Formation, but has traces of other salt deposits such as the Leine, Aller, Ohre, Friesland, and Fulda evaporite structures. The salt deposited during the Permian initially rested below the overburden from later geologic epochs, however, during the Jurassic it began to shape into a salt pillow. During the series of compressional phases during the Late Cretaceous, this salt pillow developed a wedge like shape which pierced the Triassic Bundsandstein layers. A visualization of the overburden and salt formations can be seen in figure 1.4. On the northeastern flank of the cross section in figure 1.4, the salt formation lies below a natural sequence of Cretaceous,

Jurassic, and Triassic layers. However, on the southwestern side of the cross section, the penetrated Zechstein creates a break in the sequence of the layers. The wedging of the salt structure between the Bundtsandstein shows how the compressive force during the Late Cretaceous influenced the region. The wedge or saddle like shape of the Asse salt structure has a thickness of about 2 km. The mine itself is built into the uppermost part of the salt structure, running through several of the different Zechstein formations. The shaft of the mine first goes through a layer of caprock, and then into the Zechstein formations. Most of the chambers of the mine lie on its south western flank in the Leine Formation. (Pollok et al., 2018)

1.3 Goal of Thesis

To gain insight of how a model of the geology of the region can be recreated with inverse modelling, computer generated forward and inverse simulations of the region were made. Previous studies, such as (Sortan, 2022), have shown that forward modeling of the Asse salt structure allows the possibility to recreate seismic data of the region. Parameters such as anisotropy and attenuation can be recreated in forward modelling simulations. With the Asse II Mine Model, a model created by (Mendez, 2024), this thesis focuses on the next step of seismic modeling. Using low frequency full waveform inversion, model parameters will be tested in order to obtain inversion results. Specifically, depth and boundary resolution depending on different model parameters will be investigated. Things such as the acquisition geometry, frequency, and inversion parameters will be changed throughout the assessment of the simulations. Inversion parameters such as misfit definition, step length, frequency filter, and time windowing will be tested. If the inverse modelling parameters can recreate an optimized model that accurately represents the observed data, the developed inverse parameters and work flow model from this thesis could be used as a foundation for further studies. It is important to remember that all simulations run in this thesis are acoustic in nature. This means that modelling done here is inelastic and represents a strong simplification of the geologic conditions in the model.

Future applications could include an application to Asse II field data and 3D scenarios. These future studies could adopt the workflow created in this thesis as a basis to developing their own workflows. Understanding obtained from this thesis, and future studies, could play an important role in planning the appropriate locations for creating new mine shafts as well as tunnels for the future extraction of the nuclear waste.

1.4 Outline

This thesis is laid out in the following manner. Chapter 1 covers all necessary background information for the reader to understand what they need to know about the Asse II mine. Chapter 2 dives into the theoretical background of the thesis. Here everything needed to understand the methods used in this thesis are explained in detail. Chapter 3 then goes into detail about forward modelling. The model setup, acquisition geometry, and how the starting model was determined is covered here. Next, in Chapter 4, the inverse modelling parameters and results of inversions are shown. Numerous comparisons between different model types are made in this chapter as well. Some of these results are included in the appendix. Chapter 5 and 6 are the Conclusion & Outlook and Acknowledgements, respectfully.

2. Theoretical Background

This chapter outlines the necessary theory needed to understand the methods used in this thesis. This includes the basics of seismic wave propagation, how seismic waves behave in acoustic media, the modelling of seismic waves, inverse theory, and an explanation on full waveform inversion.

2.1 Seismic wave propagation

The theoretical background of seismic wave propagation is built off of two equations, the equation of motion and the stress-strain relation. These equations are used to derive the wave equation, which is necessary to describe the behaviour of seismic waves. The combination of the wave equation and its boundary conditions are fundamental to creating a complete picture of seismic wave propagation. The majority of the knowledge in this section comes from the technical report of (Müller, 2007).

2.1.1 The equation of motion

To understand the nature of seismic wave propagation, the equation of motion is fundamental. It represents the relationship between the inertia, body forces, and surface forces that are exhibited during seismic wave propagation. Body forces refer to the forces that are acting within a finite volume, and are proportional to the volume of that element. Surface forces are the forces acting upon the surface of the element and come from the volume of neighboring structures. The equation of motion is shown in equation 2.1

$$\rho \frac{\partial^2 u_i}{\partial t^2} = \frac{\partial p_{ij}}{\partial x_j} + f_i. \quad (2.1)$$

Here u_i represents displacement, ρ is density, p_{ij} is stress, and f_i represents body forces. The left hand side of the equation represents the force of inertia while the right hand side represents surface forces and body forces. These forces are described by the terms $\frac{\partial p_{ij}}{\partial x_j}$ and f_i , respectfully.

2.1.2 The stress-strain relation

The stress-strain relation in the context of seismic wave propagation describes elastic deformation of the rock within which a wave is propagating. This type of deformation occurs within the scope of Hooke's Law and can be described by the deformation tensor

$$\epsilon_{ij} = \frac{1}{2} \left(\frac{\partial u_i}{\partial x_j} + \frac{\partial u_j}{\partial x_i} \right).$$

In seismic wave theory, and in the context of this thesis, a linear relationship is assumed for the stress-strain relationship. This means that the stress and strain that a rock experiences while a seismic wave passes through it are proportional. This relation, for the anisotropic case, is shown in equation 2.2

$$\sigma_{ij} = c_{ijkl}\epsilon_{kl}. \quad (2.2)$$

Here σ_{ij} is the stress tensor, c_{ijkl} is the stiffness tensor, and as previously mentioned, ϵ_{kl} is the deformation tensor. Within the deformation tensor $\epsilon_{kl} = \frac{1}{2} \left(\frac{\partial u_k}{\partial x_l} + \frac{\partial u_l}{\partial x_k} \right)$, u , represents particle displacement. Particle displacement is the deformation of the rock particles in which the wave is propagating through. It is common to use the derivative of the deformation tensor $\dot{\epsilon}_{kl}$. In this case, particle displacement becomes particle velocity when differentiating with respect to time. The resulting equation is

$$\dot{\epsilon}_{kl} = \frac{1}{2} \left(\frac{\partial v_k}{\partial x_l} + \frac{\partial v_l}{\partial x_k} \right). \quad (2.3)$$

When the medium in which a wave is propagating is isotropic, the stress-strain relation is

$$\sigma_{ij} = \lambda\theta\delta_{ij} + 2\mu\epsilon_{ij}. \quad (2.4)$$

Here λ and μ are the material parameters, also called Lamé parameters, and θ represents cubic dilatation. For the Lamé parameters, μ represents the shear modulus and in combination with λ yields the p-wave modulus. Cubic dilatation represents the divergence of \vec{u} and can be written as $\theta = \epsilon_{11} + \epsilon_{22} + \epsilon_{33}$.

2.1.3 The Acoustic Case

In this study acoustic wave propagation is used for 2D forward and inverse modelling of the Asse mine. Acoustic waves, also frequently referred to as compressional or pressure waves, change due to disturbances in pressure of a local system. Here pressure p and density ρ are the parameters that help describe seismic wave propagation. The main similarity that acoustic waves have in common with elastic waves is that velocity of the pressure particles v_p determines kinetic energy and displacement from equilibrium pressure p_0 describe potential energy (Sahin et al., 2023).

All further mathematical calculations will be adjusted to fit the acoustic case. The following derivation was made with the help of (Morse, 1953). In the stress-strain relation this means that the shear modulus of the stress-strain relation is zero. Thus $\mu = 0$, and the stress tensor, now p_{ij} , simplifies to

$$p = \begin{pmatrix} -p & 0 & 0 \\ 0 & -p & 0 \\ 0 & 0 & -p \end{pmatrix}.$$

This also means that an isotropic geology is considered. The rocks within which the seismic waves will propagate through do not have a specified orientation, i.e. there is

no anisotropy. Thus the stress-strain relation for the isotropic case is used. With the aforementioned criteria, this simplifies the isotropic stress-strain relation to

$$-p = \lambda \operatorname{div}(\vec{u}) \quad (2.5)$$

Consequently, in the equation of motion the body forces represented by f_i in equation 2.1 are obsolete, resulting in

$$\frac{\partial^2 u_i}{\partial t^2} = -\frac{1}{\rho} \frac{\partial p}{\partial x_i} \quad (2.6)$$

By combining the two cases, the simplification of the stress-strain relation, equation 2.5 and equation of motion, equation 2.6, the acoustic wave equation can be derived. To do this, first the stress-strain relation must be differentiated with respect to time

$$-\frac{\partial p}{\partial t} = \lambda \operatorname{div}(\vec{v}) \quad (2.7)$$

and particle velocity must be introduced to the equation of motion, $v_i = \frac{\partial u_i}{\partial t}$, to get

$$\frac{\partial v_i}{\partial t} = -\frac{1}{\rho} \frac{\partial p}{\partial x_i}. \quad (2.8)$$

Equation 2.7 and 2.8 give the first order acoustic wave equations. To get the second order acoustic equation, the derivative of equation 2.7 is taken. Then equation 2.8 is plugged into this derivative, which results in

$$-\frac{\partial^2 p}{\partial t^2} = \lambda \left(\frac{\partial}{\partial x_1} \frac{\partial v_1}{\partial t} + \frac{\partial}{\partial x_2} \frac{\partial v_2}{\partial t} + \frac{\partial}{\partial x_3} \frac{\partial v_3}{\partial t} \right). \quad (2.9)$$

Then by plugging in equation 2.8 into 2.9, equation 2.10 is obtained

$$-\frac{\partial^2 p}{\partial t^2} = -\lambda \left(\frac{\partial}{\partial x_1} \left(\frac{1}{\rho} \frac{\partial p}{\partial x_1} \right) + \frac{\partial}{\partial x_2} \left(\frac{1}{\rho} \frac{\partial p}{\partial x_2} \right) + \frac{\partial}{\partial x_3} \left(\frac{1}{\rho} \frac{\partial p}{\partial x_3} \right) \right). \quad (2.10)$$

Which can be simplified by assuming constant density

$$\frac{\partial^2 p}{\partial t^2} = v_p^2 \nabla^2 p. \quad (2.11)$$

This is the common version of the second order acoustic wave equation. Here $v_p = \sqrt{\frac{K}{\rho}}$ and represents compressional velocity. The bulk modulus is represented by K .

2.2 Numerical Modelling

Numerical modelling refers to implementation of forward and inverse problems on numerical grids. These grids use time-domain finite difference (FD) schemes to solve equations by replacing partial derivatives with finite difference operators. While there are several numerical modelling approaches and methods, in this thesis, the finite-difference method, the most robust and popular, will be used. To perform the forward modelling and implement the FD method the software IFOS2D (Inversion of Full Observed Seismograms) was used. The forward portion of this code was written by (Bohlen, 1998), and the inverse portion was written by (Köhn, 2011).

The finite difference approximation is used to replace the partial derivatives of the parameters of the equation in question in the space and time domain. This is done for models that have been discretized on numerical grids which have equidistant grid point spacing and a rectangular geometry. In order to increase the accuracy of the approximation, a standard staggered grid (SSG) layout is used (Virieux, 1986). In a SSG layout, model parameters are spread out between half points and full points. By distributing the grid points in this way, the model parameters of the forward problem can be solved separately and thus give a more accurate result. The basic discretization in time and space is given by

$$\begin{aligned}x &= i \, dh \\y &= j \, dh \\t &= n \, dt.\end{aligned}\tag{2.12}$$

Here (i, j) signifies grid point position and n is the time index. On a SSG, the parameters of the acoustic wave equation are distributed as shown in figure 2.1. Here velocity v_x and v_y are solved for at staggered grid positions while p-wave velocity v_p , pressure p , and density ρ are solved for at full grid positions. The pressure and velocity elements are displayed below. Pressure is located at full grid positions in space and half grid positions in time

$$p = p^{\frac{n}{2}}(i, j)\tag{2.13}$$

and particle velocity is located at staggered positions in space and half positions in time

$$v_x = v^n\left(\frac{i}{2}, j\right) \quad \text{and} \quad v_y = v^n\left(i, \frac{j}{2}\right).\tag{2.14}$$

Since density is constant, it is negligible and can be ignored. Other than using half points, the characteristics of a SSG are similar to that of a regular grid. The finite difference equations for a SSG are shown below

$$\frac{\partial f}{\partial x}(n, i) = \frac{f\left(n, i + \frac{1}{2}\right) - f\left(n, i - \frac{1}{2}\right)}{\Delta h} + O(\Delta h^2)\tag{2.15}$$

$$\frac{\partial f}{\partial t}(n, i) = \frac{f\left(n + \frac{1}{2}, i\right) - f\left(n - \frac{1}{2}, i\right)}{\Delta t} + O(\Delta t^2).\tag{2.16}$$

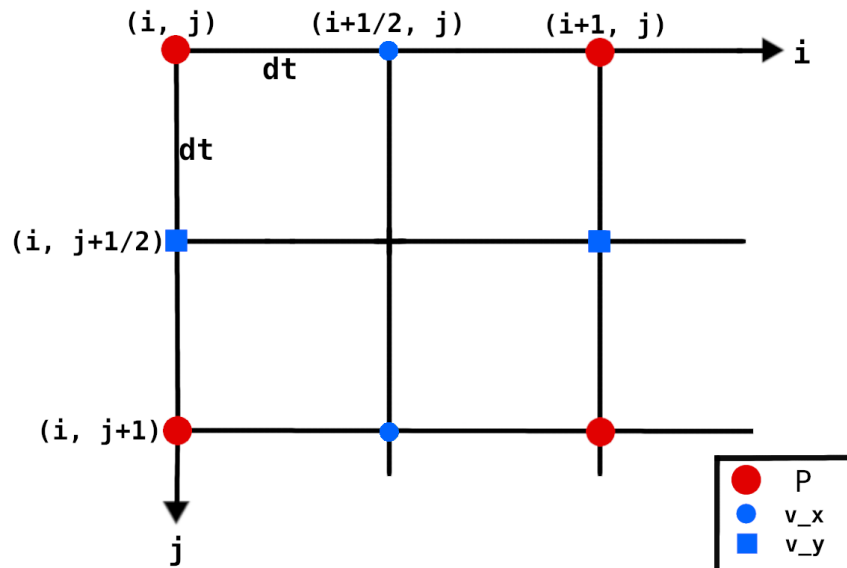


Figure 2.1: FD staggered grid showing points for pressure and velocity. This grid shows how in a standard staggered grid half points are placed between full points. The different grid points are dependent on each other for further calculations. The mathematical theory for this is seen in detail in section 2.

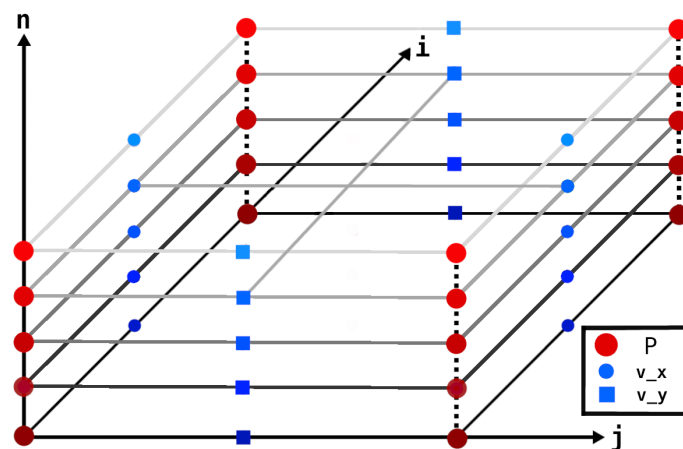


Figure 2.2: A figure showing the update scheme for a FD standard staggered grid now with time indexing. This is a 2D figure that shows the time update scheme represented by the n axis. Figure 2.1 represents one layer, n , of figure 2.2. This figure depicts $n + k$ and $n - k$.

Equation 2.15 and 2.16 show that in a SSG layout, adding or subtracting from the position i for spatial discretization and n for temporal discretization by $\frac{1}{2}$ can be used to approximate a continuous function f .

2.2.1 Discretizing the Acoustic Wave Equation

For the acoustic wave equation to be discretized on a SSG, equations 2.7 and 2.8 must be discretized. The update scheme, the equation representing the calculation needed to portray the next grid point, can then be derived. It is important to note that in the numerical grid, $dx = dz = dh$. The following equations were derived with the help of (Pontius, 2016) and (Igel, 2017).

$$\begin{aligned} \frac{v_x^{n+1}(i + \frac{1}{2}, j) - v_x^n(i + \frac{1}{2}, j)}{dt} &= \frac{1}{\bar{\rho}(i + \frac{1}{2}, j)} \frac{(p^{n+\frac{1}{2}}(i, j) - p^{n+\frac{1}{2}}(i + 1, j))}{dh} \\ \frac{v_y^{n+1}(i, j + \frac{1}{2}) - v_y^n(i, j + \frac{1}{2})}{dt} &= \frac{1}{\bar{\rho}(i, j + \frac{1}{2})} \frac{(p^{n+\frac{1}{2}}(i, j) - p^{n+\frac{1}{2}}(i, j + 1))}{dh} \end{aligned} \quad (2.17)$$

$$\begin{aligned} \frac{p^{n+\frac{1}{2}}(i, j) - p^{n-\frac{1}{2}}(i, j)}{dt} &= \\ \rho(i, j) v_p^2(i, j) \frac{(v_x^n(i + \frac{1}{2}, j) - v_x^n(i - \frac{1}{2}, j) + v_y^n(i, j + \frac{1}{2}) - v_y^n(i, j - \frac{1}{2}))}{dh} \end{aligned} \quad (2.18)$$

The density while constant, is represented on the SSG due to it being needed to calculate v_x , v_y , and p . It is represented by the finite difference approximations,

$$\bar{\rho}(i + \frac{1}{2}, j) = \frac{\rho(i, j) + \rho(i + 1, j)}{2} \quad \text{and} \quad \bar{\rho}(i, j + \frac{1}{2}) = \frac{\rho(i, j) + \rho(i, j + 1)}{2}. \quad (2.19)$$

By solving for $v_x^{n+\frac{1}{2}}$, $v_z^{n+\frac{1}{2}}$, and $p^{n+\frac{1}{2}}$, the update schemes for the numerical grid are obtained

$$\begin{aligned} v_x^{n+1}(i + \frac{1}{2}, j) &= v_x^n(i + \frac{1}{2}, j) + \frac{1}{\bar{\rho}(i + \frac{1}{2}, j)} \frac{dt}{dh} (p^{n+\frac{1}{2}}(i, j) - p^{n+\frac{1}{2}}(i + 1, j)) \\ v_y^{n+1}(i, j + \frac{1}{2}) &= v_y^n(i, j + \frac{1}{2}) + \frac{1}{\bar{\rho}(i, j + \frac{1}{2})} \frac{dt}{dh} (p^{n+\frac{1}{2}}(i, j) - p^{n+\frac{1}{2}}(i, j + 1)). \end{aligned} \quad (2.20)$$

$$\begin{aligned} p^{n+\frac{1}{2}}(i, j) &= \\ p^{n-\frac{1}{2}}(i, j) + \\ \rho(i, j) v_p^2(i, j) \frac{dt}{dh} \left(v_x^n(i + \frac{1}{2}, j) - v_x^n(i - \frac{1}{2}, j) + v_y^n(i, j + \frac{1}{2}) - v_y^n(i, j - \frac{1}{2}) \right) \end{aligned} \quad (2.21)$$

These update schemes represent how the FD method calculates the value for the next grid point in the numerical grid. This can be visualized using figure 2.1 and figure 2.2. Figure 2.1 depicts the update scheme, without the time index n . It shows how the

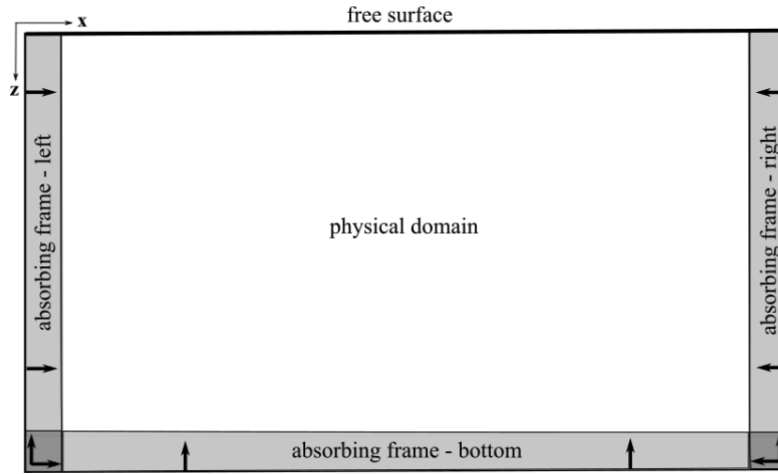


Figure 2.3: A representation of a standard FD grid, its absorbing boundaries, and free surface. The physical domain contains the FD grid. This figure was taken from (Sortan, 2022).

different points in the grid are related and dependent on each other. Incorporating the time index, values for pressure and the velocity at $n + \frac{1}{2}$ can be calculated via the positions from the prior time step n . This can be seen in the update scheme equations and in figure 2.2.

2.2.4 Initial and boundary conditions

Boundary conditions describe how seismic waves behave at interfaces and at boundaries. This refers to the geophysical laws that dictate how the wave responds to a boundary between a solid-solid, solid-fluid, and solid-vacuum. Different kinds of boundaries impact the continuity of stress and material parameters at the interfaces differently. When producing a numerical model, these boundaries conditions must be described by the geologic model. The boundary conditions must be prepared so that they best represent the studied area.

In order to prevent unnecessary reflections off the left, right, and lower outer frames of the grid, as seen in figure 2.3, absorbing boundary conditions are used to dampen wave propagation. The absorbing boundary conditions however are not set directly on the outer frames of the grid, but are extended outward from these frames in order to dampen waves before they reach the boundaries. For this thesis, a conventionally perfectly matched layer C-PML (Komatitsch and Martin, 2007) absorbing boundary condition was used to effectively dampen the waves approaching these boundaries.

2.2.5 Grid Dispersion

Grid dispersion is a prominent issue when dealing with numerical modeling. When a model is experiencing grid dispersion, it means that the numerical wavefield is not being adequately sampled due to a too high or low spatial grid point spacing (Köhn et al., 2005). When setting up a simulation for a model equation 2.22 and 2.23 show the maximum value dh that should be used for grid spacing

$$\lambda_{min} = \frac{v_{min}}{f_{max}}. \quad (2.22)$$

λ_{min} can then be used to solve for dh

$$dh \leq \frac{\lambda_{min}}{n}. \quad (2.23)$$

In equation 2.22 v_{min} is minimum velocity of the model and f_{max} is the maximum frequency of the source signal. λ_{min} is the minimum wavelength and n is based off of the order and type of FD operator. This can be viewed in table 2.1 and was taken from (Köhn et al., 2005). While it would seem intuitive to take the smallest possible grid spacing in order to get a more accurate solution, a trade off between grid size spacing and computational cost must be considered. Finer grid spacing requires more computation and should thus be chosen sensibly.

Table 2.1: The minimum number of grid points needed per wavelength depending on the FD order and operator type.

FD Order	n (Taylor)	n (Holberg)
2nd	12	12
4th	8	8.32
6th	6	4.77
8th	5	3.69
10th	5	3.19
12th	4	2.91

2.2.6 Courant Instability

While the FD grid covers the spatial discretization of the simulation, a temporal discretization is also necessary. In order for the FD simulation to be stable, temporal discretization must be less than that of the maximum value of the time step dt . This means that the duration of equal discrete time steps dt along a wave must be less than the time needed for the wave to travel between adjacent grid points that have a grid spacing dh (Courant et al., 1928). The following formula gives the necessary value for dt in a FD simulation. If this condition is not upheld then the simulation will break off.

$$dt \leq \frac{dh}{h\sqrt{2} v_{max}} \quad (2.24)$$

Here dh represents grid point spacing, h is dependent on the order of the FD operator, and v_{max} is the maximum velocity of the model.

2.3 Inverse Theory

Inverse modeling refers to using data in order to recreate a desired model. It can either be done by taking data obtained from a starting model and iteratively changing its parameters to fit a set of observed data, or by taking modelled data and using an algorithm to calculate a desired model (Ritter, 2020). In the case of FWI, the first option, an iterative workflow, is used to try to recreate reference models. This varies from other inverse problems in that full waveforms are used for forward and adjoint modeling during the inversion process.

In FWI, a numerical model is created to simulate the propagation of seismic waves through the subsurface. This model incorporates the desired parameters such as p-wave velocity and density. The goal is to find the subsurface model that minimizes the difference between the observed and starting seismic data of the numerical model. This is formulated as an optimization problem, where the model parameters are adjusted to achieve the best match. The gradient of the misfit function, representing the difference between observed and starting data, is calculated with respect to the model parameters. This gradient guides the inversion process towards a better-fitting model.

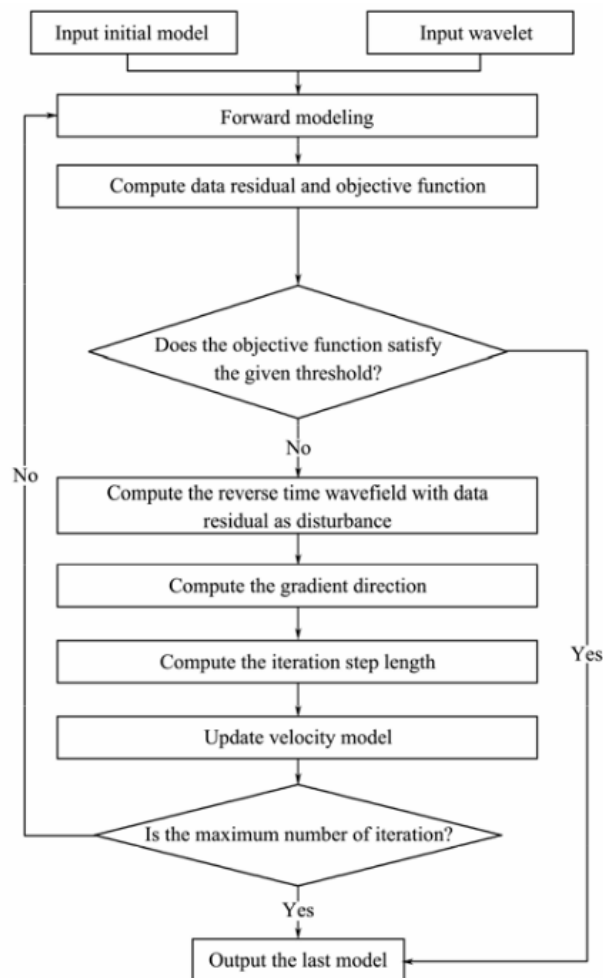


Figure 2.4: This figure demonstrates the typical workflow in a FWI run. Forward and adjoint modelling are used to reach an updated version of the model. This image is taken from (Peng et al., 2019).

An optimization algorithm is employed to update the model parameters in an attempt to minimize the misfit function. The inversion process is repeated iteratively until a convergence criterion is met, indicating that the model has reached a satisfactory fit to the observed data. The final result of the inversion is an optimal model of the subsurface, revealing details such as geological structures, fluid distribution, and other relevant properties (Tarantola, 1984, Virieux and Operto, 2009, Pratt and Shin, 1998). The iterative process that is underwent during FWI is displayed in figure 2.4.

2.3.1 The Inverse Method

The iterative approach to minimizing residuals between observed and starting data is essential to FWI. With help from (Köhn, 2011) and (Ritter, 2020) a general outline of the inverse theory and the theory behind FWI is given below.

In inverse theory, data d is obtained from a model m by an operator G . In this case, G is non-linear

$$d = G(m). \quad (2.25)$$

The acquisition of the data set d is done by forward modelling of the model m . This is done for the observed data d^{obs} and modelled data set d^{mod} . Intuitively, the model m for a data set d can be obtained by the inverse

$$m = G^{-1}(d). \quad (2.26)$$

To measure the difference between d^{obs} and d^{mod} , the residual δd can be calculated via

$$\delta d(m) = d^{obs} - d(m)^{mod}. \quad (2.27)$$

The difference between the two data sets can be measured by a misfit function such as

$$E(m) = \frac{1}{2} \delta d^T \delta d. \quad (2.28)$$

Here $E(m)$ refers to the residual energy in δd , the difference between the observed and modelled data for a model parameter m . It is desirable for $E(m)$ to be as small as possible as a low residual energy value indicates that the observed model has been recreated well. To derive the model update for m , it is first necessary to define m as m_1 ,

$$m_1 = m_0 + \delta m_0. \quad (2.29)$$

In equation 2.29, m_1 is the updated model parameter and m_0 is the unaltered model parameter based of a set of initial parameters. For m_1 to be updated appropriately, the perturbation or step direction must move δm_0 in a calculated matter. How step

length and direction are made is covered in further detail in section 2.3.5. Substituting equation 2.29 into m in equation 2.28, gives

$$E(m_0 + \delta m_0) \quad (2.30)$$

which when expanded in a Taylor series is

$$E(m_0 + \delta m_0) \approx E(m_0) + \frac{\partial E(m_0)}{\partial m} \delta m_0 + \dots \quad (2.31)$$

By taking the derivative of this Taylor series with respect to model parameters, the following is obtained

$$\frac{\partial E(m_0 + \delta m_0)}{\partial m_0} \approx \frac{\partial E(m_0)}{\partial m_0} + \frac{\partial^2 E(m_0)}{\partial m_0^2} \delta m_0. \quad (2.32)$$

The minimum of the misfit function would ideally be zero, thus equation 2.32 is set to zero. This makes it possible for the model update parameter δm_0 to be defined

$$\delta m_0 = - \left[\frac{\partial^2 E(m_0)}{\partial m_0^2} \right]^{-1} \frac{\partial E(m_0)}{\partial m_0}. \quad (2.33)$$

Here it possible to identify two important elements of the misfit function. The gradient $\frac{\partial E(m_0)}{\partial m_0}$ and the Hessian $\frac{\partial^2 E(m_0)}{\partial m_0^2}$ which can be depicted by H . Plugging equation 2.33 into equation 2.29 yields

$$m_{n+1} = m_n - H_n^{-1} \frac{\partial E(m_n)}{\partial m_n}. \quad (2.34)$$

Where m_0 has been replaced by m_n and m_1 is now m_{n+1} . The gradient is the first derivative of the misfit and represents the steepest descent of the misfit function from m_n towards m_{n+1} . The Hessian is the second derivative of the misfit function, and contains a large matrix of second order derivatives of the misfit function.

$$H_E = \begin{bmatrix} \frac{\partial^2 E}{\partial m_1^2} & \frac{\partial^2 E}{\partial m_1 \partial m_2} & \cdots & \frac{\partial^2 E}{\partial m_1 \partial m_n} \\ \frac{\partial^2 E}{\partial m_2 \partial m_1} & \frac{\partial^2 E}{\partial m_2^2} & \cdots & \frac{\partial^2 E}{\partial m_2 \partial m_n} \\ \vdots & \vdots & \ddots & \vdots \\ \frac{\partial^2 E}{\partial m_n \partial m_1} & \frac{\partial^2 E}{\partial m_n \partial m_2} & \cdots & \frac{\partial^2 E}{\partial m_n \partial m_n} \end{bmatrix} \quad (2.35)$$

Due to the size of the Hessian matrix, it is commonly replaced with P_n , a preconditioning operator, and α , the step length size. This results in equation 2.36 and is also known as the quasi-Newton Method

$$m_{n+1} = m_n - \alpha_n P_n \frac{\partial E(m_n)}{\partial m_n}. \quad (2.36)$$

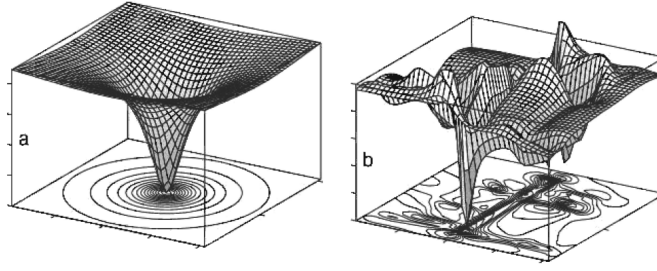


Figure 2.5: Both figures here represent misfit functions. The functions are shown as complex surfaces. **Figure a** shows a misfit function with one global minimum. An easily definable minimum value for the function. **Figure b** shows a function with many local minimums and one global minimum. Theoretically, it is more difficult to find the global minimum for **b**, since there is a higher likelihood of getting 'lost' in one of the many local minima. A correct step length and misfit definition are necessary to avoid this. This figure is taken from (Ritter, 2020).

2.3.2 Misfit Definition

In the previous section, the iterative approach of the L2 norm, has been described. For FWI, the 'precedent' entails frequent usage of the L2 norm during inversion. However, this is not always the case, and the misfit of an inversion can be defined with other functions. For instance, in this thesis, the global correlation (Choi and Alkhalifah, 2012) definition is used. The global correlation differs from the L2 norm in that it takes the cross-correlation of the normalized observed d^{obs} and modelled signal d^{mod} , as shown below

$$E = \sum_s \sum_{rec} [-\hat{d}^{mod} \cdot \hat{d}^{obs}]. \quad (2.37)$$

By taking the derivative of 2.37 with respect to the model parameters, the following is obtained

$$\frac{\partial E}{\partial m} = \sum_s \sum_r \left[\frac{\partial d^{mod}}{\partial m} \cdot \delta \bar{d} \right] \quad (2.38)$$

where

$$\delta \bar{d} = \frac{1}{\|d^{mod}\|} \left(\hat{d}^{mod} (\hat{d}^{mod} \cdot \hat{d}^{obs}) - \hat{d}^{obs} \right). \quad (2.39)$$

This is the residual trace, and it is used to obtain the gradient in equation 2.38 by being back propagated.

2.3.3 Adjoint Gradient

The model parameter update is shown in equation 2.36. It is now important to calculate the gradient for the model parameters m_n , and apply the acoustic case to the calculations. Once the gradient of the correct model parameters has been calculated, the other terms within equation 2.36 can be addressed. In the following a general description of the adjoint state method is made (Köhn, 2011). In this

study, the method used to calculate the gradient is the adjoint state method (Plessix, 2006). This method is unique from other gradient calculation methods in that it uses forward and backward propagated wavefields to effectively map changes between data and model space. This means that whenever perturbations within the model or data space occur they can be accurately represented in the other corresponding model or data space. In order for it to be possible to use the adjoint state method there are two criteria that need to be fulfilled. Firstly, there needs to be a solution to the forward problem. Without a forward modelled wavefield there cannot be a backward wavefield. Also called the adjoint wavefield. Secondly, the adjoint state method can be used only if the misfit function does not directly depend on the model parameters. The misfit function must only depend on the model parameters through state variables, solutions of the forward problem. In the acoustic case this refers to ρ and v_p (Pontius, 2016). The following from (Köhn, 2011) demonstrates a general approach to the adjoint method which successfully maps perturbations between models and data.

Take equation 2.28 and expand it to its misfit definition

$$E = \frac{1}{2} \sum_{\text{sources}} \int dt \sum_{\text{receiver}} \delta d^2(x_r, x_s, t). \quad (2.40)$$

By deriving with respect to the model parameters, the following is obtained

$$\frac{\partial E}{\partial m} = \sum_{\text{sources}} \int dt \sum_{\text{receiver}} \frac{\partial d^{\text{mod}}(m)}{\partial m} \delta d. \quad (2.41)$$

Here δd is a perturbation in data space and $\frac{\partial d^{\text{mod}}(m)}{\partial m}$ is the Frechet derivative. The Frechet derivative and data perturbation are summed over all receiver and source positions. With a known model perturbation δm and Frechet derivative, all perturbations in the model space can be integrated over the volume of the model (Tarantola, 2005) to get the total change in data space δd

$$\delta d = \int_V dV \frac{\partial d}{\partial m} \delta m. \quad (2.42)$$

Thus with the Frechet derivative, data perturbation, and a sum over all receiver and source positions, the model perturbation can be calculated

$$\delta m' = \sum_{\text{sources}} \int dt \sum_{\text{receiver}} \left[\frac{\partial d}{\partial m} \right]^* \delta d. \quad (2.43)$$

Here $\left[\frac{\partial d}{\partial m} \right]^*$ represents the adjoint wavefield. Going back from data to model space. It is important to note that in equations 2.43 and 2.42, the variables δm and δd are not identical.

Since equations 2.43 and 2.42 are both linear, it can be said that

$$\frac{\partial E}{\partial m} = \left[\frac{\partial d}{\partial m} \right]^* \quad (2.44)$$

the kernel $\frac{\partial d}{\partial m}$ in equation 2.42 and 2.43 are identical, thus the mapping from data to model space is equal to the gradient of the residual energy (Tarantola 2005)

$$\delta m' = \frac{\partial E}{\partial m}. \quad (2.45)$$

To visualize adjoint modelling and wavefields, figure 2.6 shows a simple diagram of forward and backward wavefields.

2.3.3 Adjoint Gradient for the Acoustic Case

To apply the aforementioned process to the acoustic case, the derived gradients from the master thesis of (Pontius, 2016) are used. This was done by taking the derived gradients from the elastic case in (Köhn, 2011) and adjusted for an acoustic wavefield. This resulted in

$$\begin{aligned} \frac{\partial E_{\text{FWI}}}{\partial K} &= - \sum_{\text{sources}} \int dt \frac{p \cdot \tilde{p}}{\rho^2 v_p^4}, \\ \frac{\partial E_{\text{FWI}}}{\partial \rho} &= - \sum_{\text{sources}} \int dt (v_x \tilde{v}_x + v_y \tilde{v}_y). \end{aligned} \quad (2.46)$$

Here p represents the forward propagated pressure field while \tilde{p} represents the adjoint pressure field. The same goes for the velocity, here the forward propagated particle velocity field is denoted by v_x and v_y , while the adjoint propagated particle velocity is \tilde{v}_x and \tilde{v}_y . The gradients of the misfit are the zero lag cross-correlation of the forward and backward propagated wavefield pressure and velocity fields. As previously mentioned in section 2.3.2, the misfit function should only depend on the model parameters through the state variables. Since the model parameters are ρ and v_p for the acoustic wavefield, the gradients must be rearranged. Doing this gives

$$\begin{aligned} \frac{\partial E_{\text{FWI}}}{\partial v_p} &= 2\rho v_p \frac{\partial E_{\text{FWI}}}{\partial K}, \\ \frac{\partial E_{\text{FWI}}}{\partial \rho'} &= v_p^2 \frac{\partial E_{\text{FWI}}}{\partial K} + \frac{\partial E_{\text{FWI}}}{\partial \rho}. \end{aligned} \quad (2.47)$$

2.3.4 Gradient Preconditioning

The gradient calculated by the derivation of the residual energy (equation 2.33) tends to suffer from illumination and geometric spreading in the forward and adjoint wavefields. Thus, within the FD model, geologic structures and interfaces deeper in the model or further from the source cannot be imaged as well as shallower structures in the model. Ultimately, this can lead to longer and less accurate inversion. In order to solve this issue, the inverse of the Hessian operator H_n is used in the misfit function. The Hessian is ideal for addressing this issue as it contains curvature information from the misfit function that helps decrease the effects of geometric spreading and poor illumination (Pratt and Shin, 1998). In theory, the Hessian matrix is ideal preconditioning operator for the gradient. However, as already stated in section 2.3.1, the Hessian's size and use of second order derivatives is very computationally

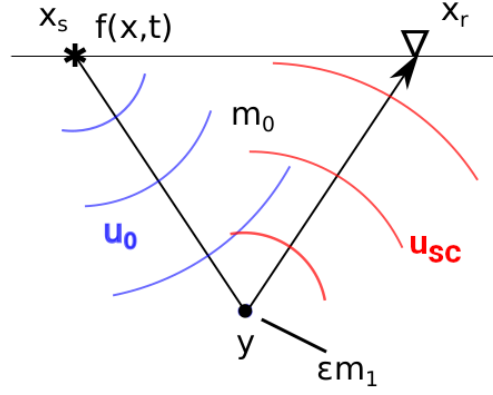


Figure 2.6: A simple diagram showing forward and adjoint modelling. The forward modelled wavefield is represented by u_0 and the backward propagated wavefield is shown by u_{sc} . The forward wavefield comes from the source at x_s while the adjoint wavefield comes from the receiver at x_r . A perturbation is shown at ϵm_1 and medium of propagation is represented by m_0 . This figure is taken from (Bohlen, 2022).

expensive and for this reason is not used. To negate this problem, the diagonal of the Hessian matrix must be calculated

$$H(\mathbf{x}, \mathbf{x}) = \sum_{\omega} \omega^4 \sum_{\mathbf{x}_s} |f_s(\mathbf{x}_s, \mathbf{x}, \omega)|^2 |G(\mathbf{x}_s, \mathbf{x}, \omega)|^2 \sum_{\mathbf{x}_r} |G(\mathbf{x}, \mathbf{x}_r, \omega)|^2. \quad (2.48)$$

Due to the computational cost, this diagonal element must be approximated by equation

$$H_a^{-1} = \left[\int dt |\vec{u}(\vec{x}_s, \vec{x}, t)|^2 \left(\operatorname{asinh} \left(\frac{x_r^{\max}(\vec{x}_s) - x}{z} \right) - \operatorname{asinh} \left(\frac{x_r^{\min}(\vec{x}_s) - x}{z} \right) \right) \right]^{-1}. \quad (2.49)$$

This approximation of the inverse diagonal Hessian matrix (Plessix and Mulder, 2004) is used to precondition the gradient in the misfit function.

2.3.5 Step Length Estimation

In order to properly estimate the step length α_n in equation 2.36, the parabolic fitting approach from (Nocedal and Wright, 2006) is used. In this approach, the step length is determined by a fitting algorithm. It is defined as

$$\alpha_n = \gamma * \frac{m_{max}}{grad_{max}}. \quad (2.50)$$

Here γ is a set value that represents the percentage change of the variables m_{max} and $grad_{max}$. Where m_{max} is the maximum value of the corresponding model parameter in the model and $grad_{max}$ is the maximum absolute value of the gradient (Köhn et al., 2005).

The misfit values are stored in a vector $L2t_n$ which correspond to the step length values in the vector α_n . The goal is that the misfit values $L2t_2 < L2t_1$ while $L2t_3 > L2t_2$. This way a parabolic line can be fit through the points $(L2t_n, \alpha_n)$, and can thus estimate an optimal step length at the minimum of the parabola.

If this method does not work, i.e. $L2t_3 < L2t_2$, then a new value for γ is determined by

$$\gamma += \gamma/\psi. \tag{2.51}$$

Where the variable ψ is a set scaling factor that reduces the percentage change between the values m_{max} and $grad_{max}$.

3. Forward Modelling

In this chapter, forward modelling is described in detail. The goal of forward modelling is to successfully implement the observed Asse model on a FD grid, and to be able to obtain data from this implementation. Which model parameters are used to discretize the model on the FD grid, as well as the acquisition geometry to generate data are described. In addition to gathering forward modeled observed data sets, the criteria for developing the starting model which is used for inversions in Chapter 4 is explained.

3.1 Observed Model

The observed synthetic geologic model of the Asse Heeseberg structure was created by (Mendez, 2024) on behalf of BGE . The software used to create the model was ArcGIS, and the velocity values in the model were obtained via measurements made by BGE in 2019-2020. The data was taken from borehole R05 on cross line 5045, and can be seen in figure 3.1 as the continuous red line running perpendicularly through the geologic layers. Using the depth profiles and velocity values gathered from the R05, the observed model was generated. Since the goal of this thesis is to preform acoustic modelling only v_p values were considered during model construction.

3.1.1 Model Parameters

The observed Asse model is 7200 m long and 2600 m deep. It represents a 2D southwest-northeast cross section of the Asse salt structure. As seen in figure 3.1, the observed Asse model shows the Zechstein salt formation and all other surrounding geology. The velocity of each layer was determined by averaging the velocity values obtained from the borehole for each layer. The geologic layers can be identified by matching its abbreviation in figure 3.1 to its full name in table 3.1.

To display the model on a FD grid, a grid spacing of two was used in the x and z direction. In the x direction, the model has 3600 grid points and 1300 grid points in the z direction. To emphasize a focus on the salt structure and nearby geology, model boundaries were set by dropping values outside of new the desired modelling zone. To get this cropped model, 300 m were dropped from either side of the model, and 900 m meters were dropped from the bottom. This resulted in a model with the dimensions 6000 m x 1700 m or 3000 grid points x 850 grid points. This cropped model is what was used in the forward modelling and full waveform inversion. It can be seen in figure 3.2. A density model was also generated and is viewable in the appendix.

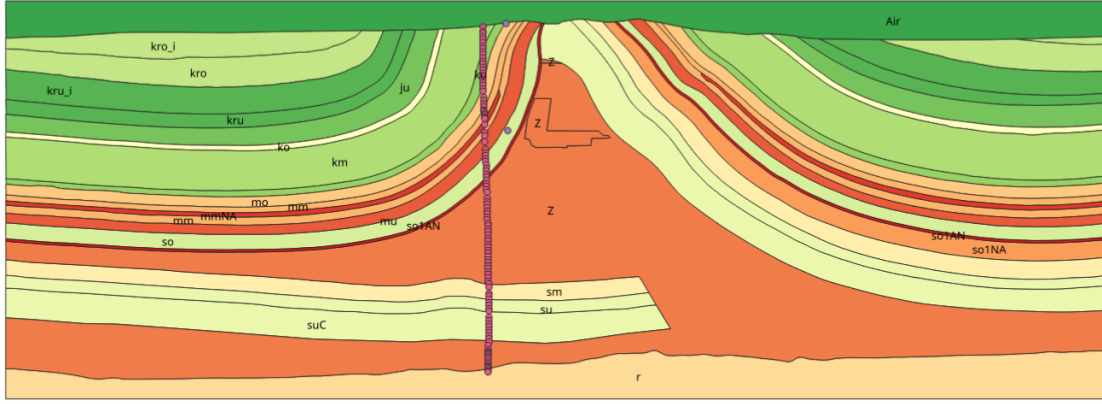


Figure 3.1: All geologic layers in the Asse II model with their corresponding label. Refer to table 3.1 for velocity information. This model was created by (Mendez, 2024) and was done with ArcGIS. It has total distance of 7200 m by 2600 m.

Table 3.1: P-wave velocity of geologic layers within designed Asse II model. The abbreviations in parenthesis match the abbreviations in figure 3.1

Model Layers	v_p (m/s)
Air	0.05
Oberkreide (kro)	2951.0
Unterkreide (kru)	2300.0
Jura (ju)	2400.0
Oberer Keuper (ko)	3550.0
Mittlerer Keuper (km)	3027.0
Unterer Keuper (ku)	2683.3
Oberer Muschelkalk (mo)	3974.4
Mittlerer Muschelkalk (mm)	483.6
Muschelkalk - Steinsalz (mmNA)	4584.0
Unterer Muschelkalk (mu)	5068.5
Röt (so)	3853.0
Röt 1 Anhydrit (so1AN)	5030.0
Mittlerer Buntsandstein (sm)	3996.7
Unterer Buntsandstein (su)	4196.4
Calvörde-Formation (suC)	4196.4
Zechstein (Z)	4583.2
Rotliegend (r)	4600.0

Within the FD grid of the observed model lies a free surface boundary. This free surface lies on top of the geologic structure, has a velocity of 0.05 m/s, and on average is about 250 m deep. The low velocity values of the free surface contrasted with the velocity of the geologic structure results in zero transmission or reflection of acoustic waves.

The sides and bottom of the observed model are both lined with a C-PML absorbing boundaries that extend inwardly from the model boundaries. Each absorbing boundary has a specified width of 15 grid points. To dampen the waves at the boundaries of the FD grid, a reference frequency of 6 Hz is used. A reference velocity of 3500 m/s is used.

Five different acquisition geometries for forward and inverse modelling were tested in order to see which setup would yield the best result. In these different geometries only source positioning and increment spacing was changed. The receiver geometry stayed the same throughout testing. The setups for the different source positioning can be seen in table 3.3.

The receiver positions and other acquisition parameters can be seen in table 3.2. All sources and receivers were set 10 m below the topography of the geologic structures. This was done so that the p-waves from the simulated source positions did not get 'caught' in the boundary between the topography and free surface. The total run time for the simulation is 2.5 s, and has a sampling rate of 1.0e-4 s. This resulted in a highly abnormal sampling rate total of 25000 samples per trace.

Table 3.2: The parameters used in forward and inverse modelling are listed here. Positioning is shown in grid points

Acquisition Geometry/Parameters	
FD Order	4
2-D Grid	NX = 3000 NY = 850 DH = 2.0
Sources	Variable
PML	FW = 15 VPPML = 3500 FPML = 8
Receiver	Start = 15 End = 2985 Spacing = 5
Time Stepping	Time = 2.5 s DT = 1.0e-4 s

Table 3.3: The different shot geometries are shown here. There is a 20, 40, 60, 81, and 103 shot model. Other parameters related to the shots are listed as well. The different shot geometries are used to test dependency of model resolution on shot number. All start, end, and increment units are in m.

Source Geometry	
20 sources	Start = 34 m End = 5950 m Increment = 300 m Ricker Wavelet Center Frequency = 6 Hz
40 sources	Increment = 150 m
60 sources	Increment = 100 m
81 sources	Increment = 74 m
103 sources	Increment = 58 m

3.1.2 Numerical Tests

An essential part of numerical modelling is checking for dispersion and ensuring stability during the modelling process. Forms of instability such as grid dispersion and inaccurate temporal discretization can be checked with the formulas from section 2.2.5 and 2.2.6. The maximum grid spacing value that should be allowed for the observed Asse model can be calculated by considering that the lowest velocity in the model, $\lambda_{min} = 2300$ m/s and max frequency $f_{max} = 12$ Hz yields

$$\lambda_{min} = \frac{2300 \text{ m/s}}{12 \text{ Hz}} \approx 50 \text{ m} \quad (3.1)$$

$$dh \leq \frac{191 \text{ m}}{8} \approx 24 \text{ m}. \quad (3.2)$$

This means that the grid spacing for this model can be up to 24 m. However, a similar grid spacing as used in the thesis of (Sortan, 2022) was used. In the thesis of Sonia Sortan, forward modelling tests were made to test the Asse II's response to the effects of attenuation and anisotropy. In her thesis, ultimately a grid spacing of $dh = 1$ was used to avoid the "staircase effect" (Moczo et al., 2007). To mitigate similar effects, a grid spacing of $dh = 2$ was used in this thesis. Such a small grid spacing causes long computation times due to the large number of grid points. While this is undesirable, a dense grid point spacing also ensures detailed data. To ensure stability of modelling, the Courant criterion must be checked. By taking the max velocity $v_{pmax} = 5068.528$ m/s, dh from equation 3.2, and setting β , the sum of the weighting coefficients of the FD Taylor operator, equal to one (Sortan, 2022) we get

$$dt \leq \frac{dh}{\beta\sqrt{2}v_{pmax}} \approx 3.34 \text{ ms}. \quad (3.3)$$

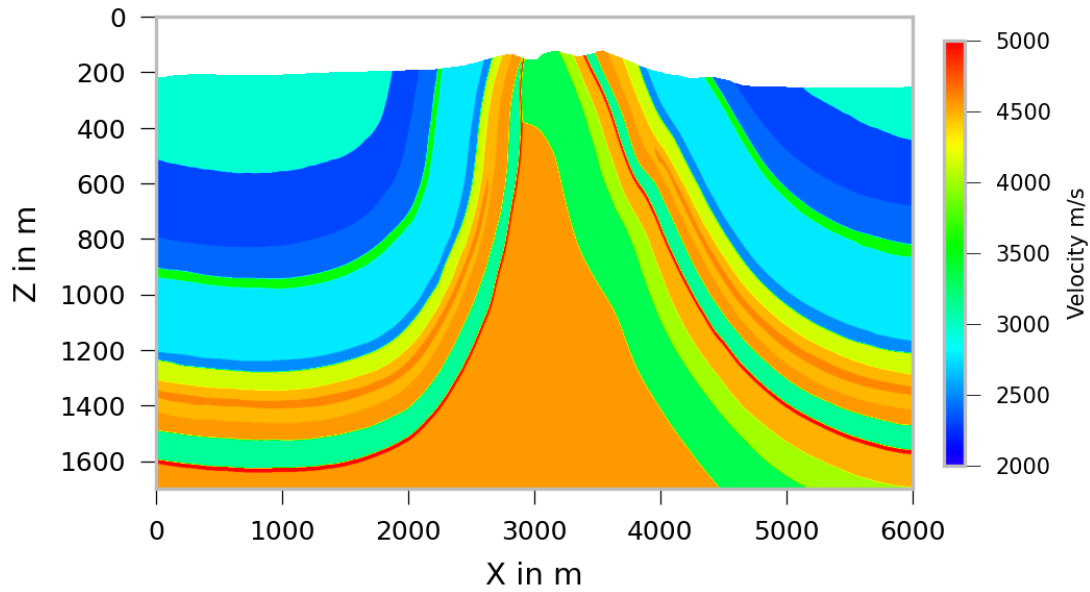


Figure 3.2: The observed velocity model created by Lenny Mendez is displayed. Here the model has been cropped to 6000 m by 1700 m. A velocity clip of 2000-5000 m/s has been applied.

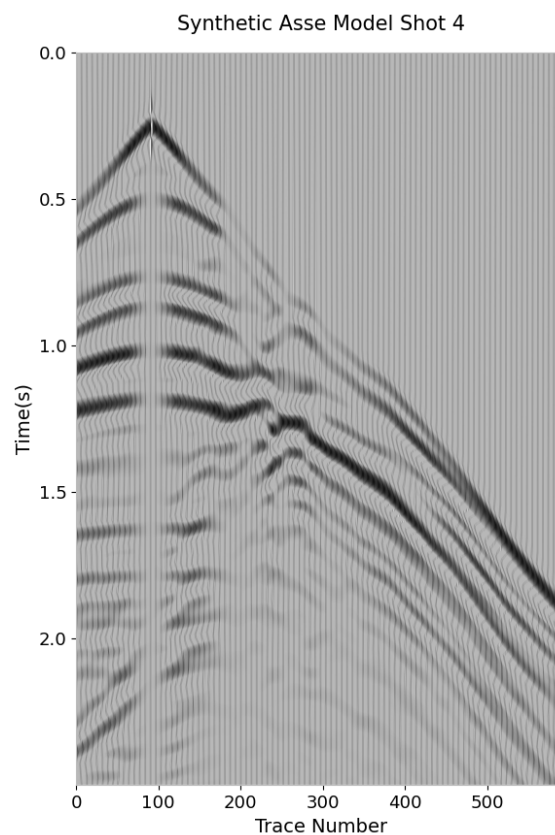


Figure 3.3: Wiggle plot of source number four in the observed Asse II model. The acquisition geometry with 20 shots and 595 receivers was used in this example.

3.2 Starting Model

In order for an inversion to be done, a starting model and an observed model are needed. The observed model is the Asse II Mine Model, figure 3.2. The starting model is created from the observed model by averaging the values of the observed model. For the Asse II Mine Model, a Gaussian blur function was used to do this. When determining the starting model, the following questions were addressed:

- How much smoothing can be used? When does the model no longer accurately converge?
- What can be expected in terms of resolution?

These questions were addressed with a cycle skipping analysis and time window inversion.

3.2.1 Smoothing Workflow

To create the starting model, a Gaussian filter function was applied to the original model. Ordinarily, this operation is quite straightforward. However, due to the free surface boundary being within the finite difference grid and it having a varying depth a few extra steps were needed. These are covered below.

1. The free surface values were extracted from the original matrix m_{org} , up to the point of the shallowest topography. This was extracted into a separate matrix, m_{sm} .
2. In this separate matrix the free surface values were separated from the other geologic values into two further matrices m_{fs} and m_{geo} .
3. The matrix with the geologic values m_{geo} was extrapolated upwards and then combined with the original matrix to create a new matrix m_{new} .
4. This new matrix was then smoothed with a Gaussian function.
 - a) To properly smooth the function, first the matrix was inverted to get the slowness.
 - b) Then a window size K and sigma value S were defined.
 - c) After the m_{new} was properly smoothed, the matrix was inverted again to return to velocity.
5. The matrices m_{new} and m_{fs} were combined.

Numerous different starting models were created with different values for sigma. The size of the kernel used for the average performed by the Gaussian function is defined below

$$K = 2 * R + 1 \tag{3.4}$$

where K is the kernel and R is the radius. Radius can be defined as

$$R = \text{round}(t * S). \tag{3.5}$$

Here $t = 1$. Ultimately, the size of K is predominately determined by the value of S . While density has been defined as constant for this thesis, it is necessary to smooth the density values as well. The same process shown above was used. All density figures are available in the appendix.

3.2.2 Cycle Skipping Analysis

When performing full waveform inversion it is important to be aware of an issue called cycle skipping. This problem arises when the waveforms from separate models are too different. Specifically, the first arrivals of the waveforms on each trace no longer lie within half a period of each other. Typically, this effect worsens the greater the offset of the receivers are from the seismic source. To address this issue, a cycle skipping analysis must be made to ensure that the first arrivals from both models are within half a period of each other. In the case of this thesis, the shots made on the observed model were compared to shots made on starting models that had varying values for sigma. One shot was taken, and four different traces were analyzed. The shot used was located at 934 m, and the receivers used were located at 2420 m, 3620 m, 4820 m, and 5920 m. Four values of sigma were tested: 100, 200, 300, and 400. All seismograms in the comparison were bandpass filtered from 5 to 8 Hz, and are shown in figures 3.4 and 3.5. The start models used to produce the seismograms are shown in figure 3.6.

As it can be seen in figures 3.4 and 3.5, the different values of sigma cause varying first breaks. In all of the comparisons, the difference is the most clear in traces 480 and 590. For sigma 100 and 200, for both comparisons, trace 590 is within a period and a half of the observed seismogram. This is however untrue for the comparisons for sigma 300 and 400. The delay between the two waveforms is at least half a period. Taking this into account, one can predict that the sigma 100 and 200 models will produce better inversions than the sigma 300 and 400 inversions. Taking the value of sigma 100 and plugging it into equation 3.4 and 3.5, gives a smoothing kernel that is 201 grid points long and wide. A sigma value of 200 gives a kernel that is 402 grid points long and wide. The comparison between the models in figure 3.6 shows the gradual simplification of the model due to the smoothing kernel. In figure 3.8 and 3.8 the wavefield propagation through the observed and sigma 100 starting model can be seen. The figure compares shows the difference of how a wavefield is influenced by a smoothing function. Since the geologic features have been smoothed, there is a more consistent travel time between the waves.

Cycle Skipping Analysis for Sigma 100 and 200

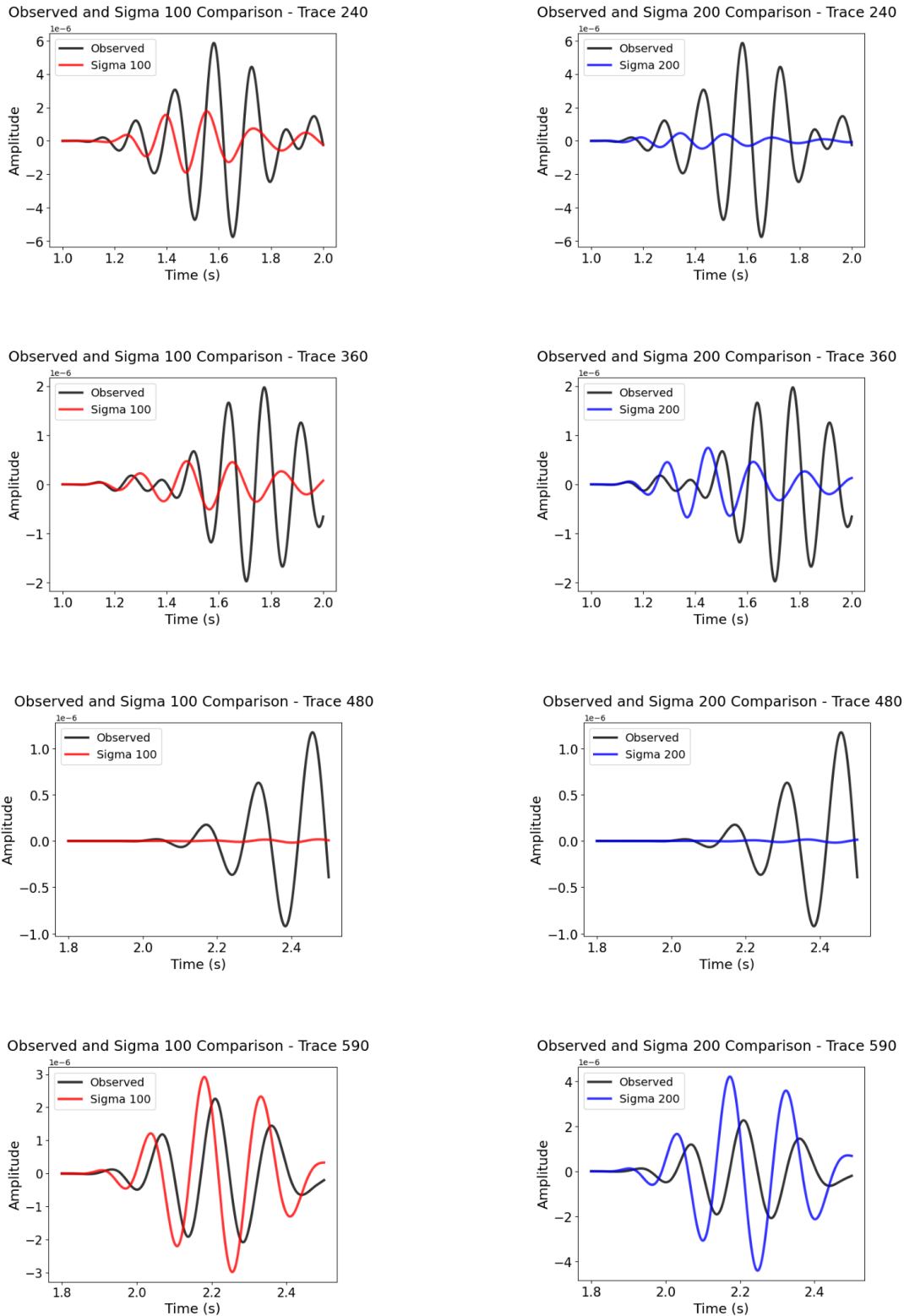


Figure 3.4: Cycle Skip Analysis. Here are the comparisons between the observed data and data obtained from sigma 100 and 200 models. A shortening of the time window of each trace has been done to focus on the first arrivals of the different shots. These seismograms show no indication of cycle skipping.

Cycle Skipping Analysis for Sigma 300 and 400

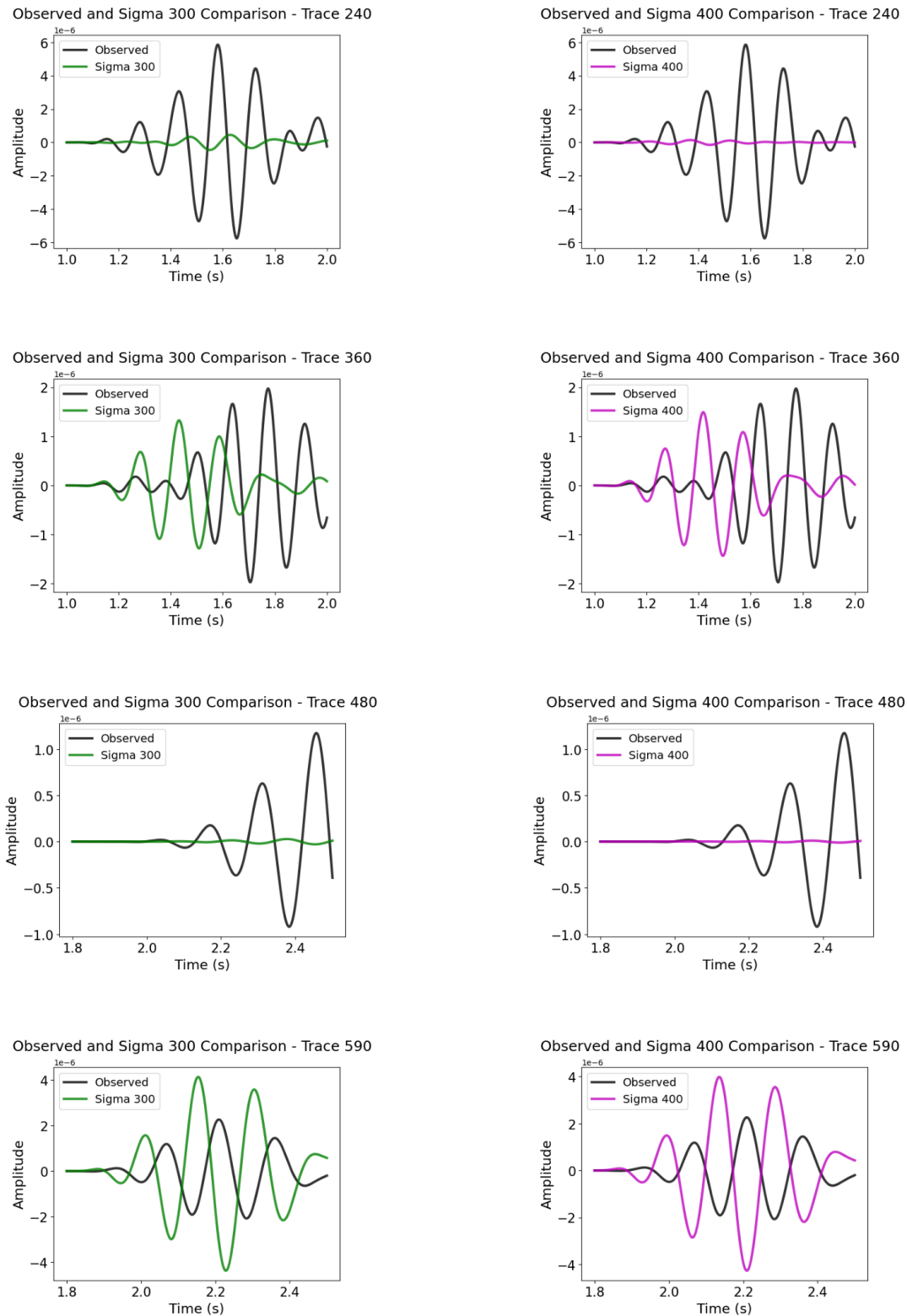


Figure 3.5: Cycle Skip Analysis. Here are the comparisons between the observed data and data obtained from sigma 300 and 400 models. A shortening of the time window of each trace has been done to focus on the first arrivals of the different shots. Both seismograms show potential cycle skipping.

Comparison of Different Starting Models

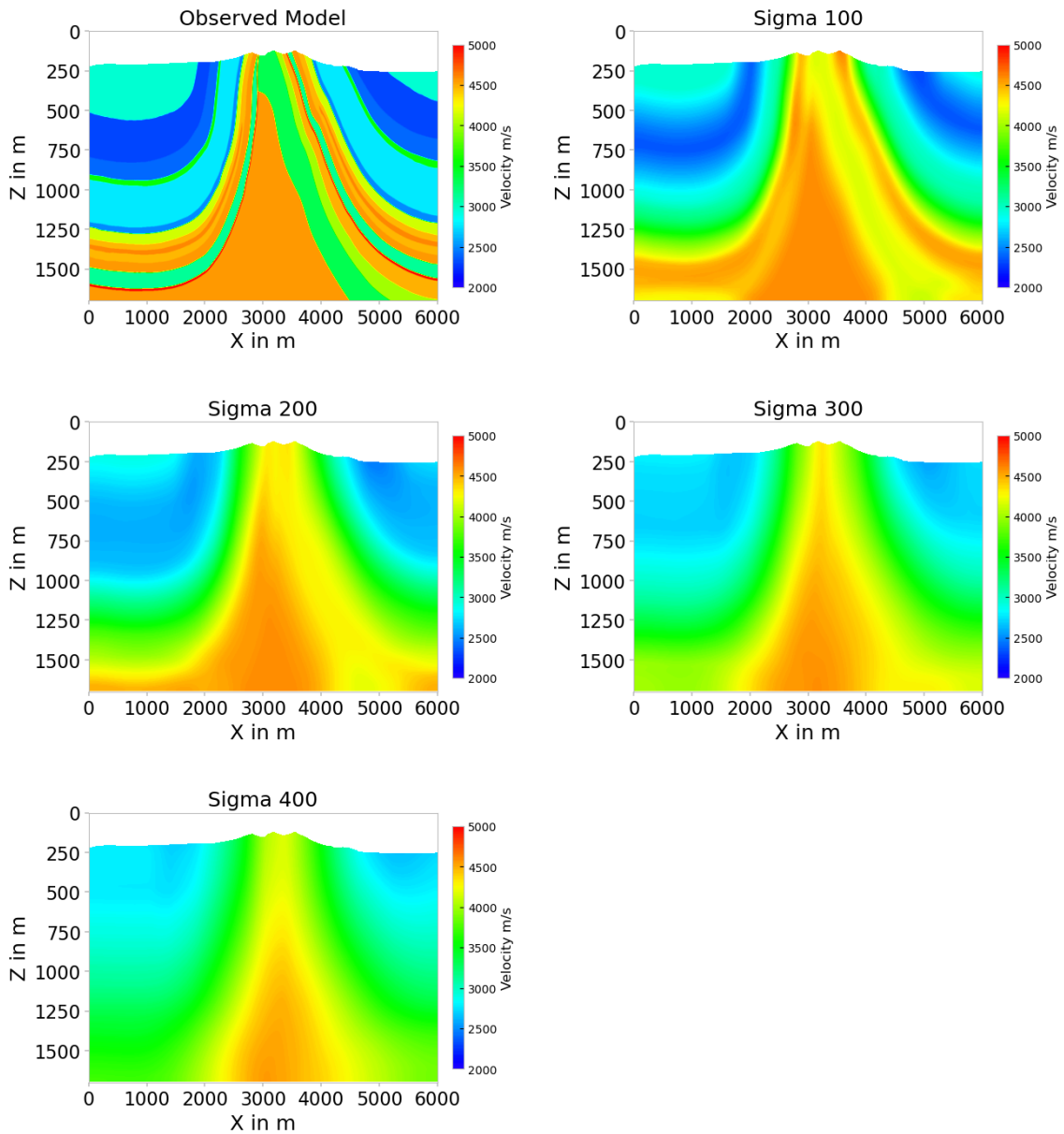


Figure 3.6: A comparison of the starting models created from using different values of sigma in the Gaussian function. These models were used for producing the data used in the cycle skipping analysis and correspond to the seismograms of the same sigma. The observed model is shown as a comparison to display how the model changes due to smoothing.

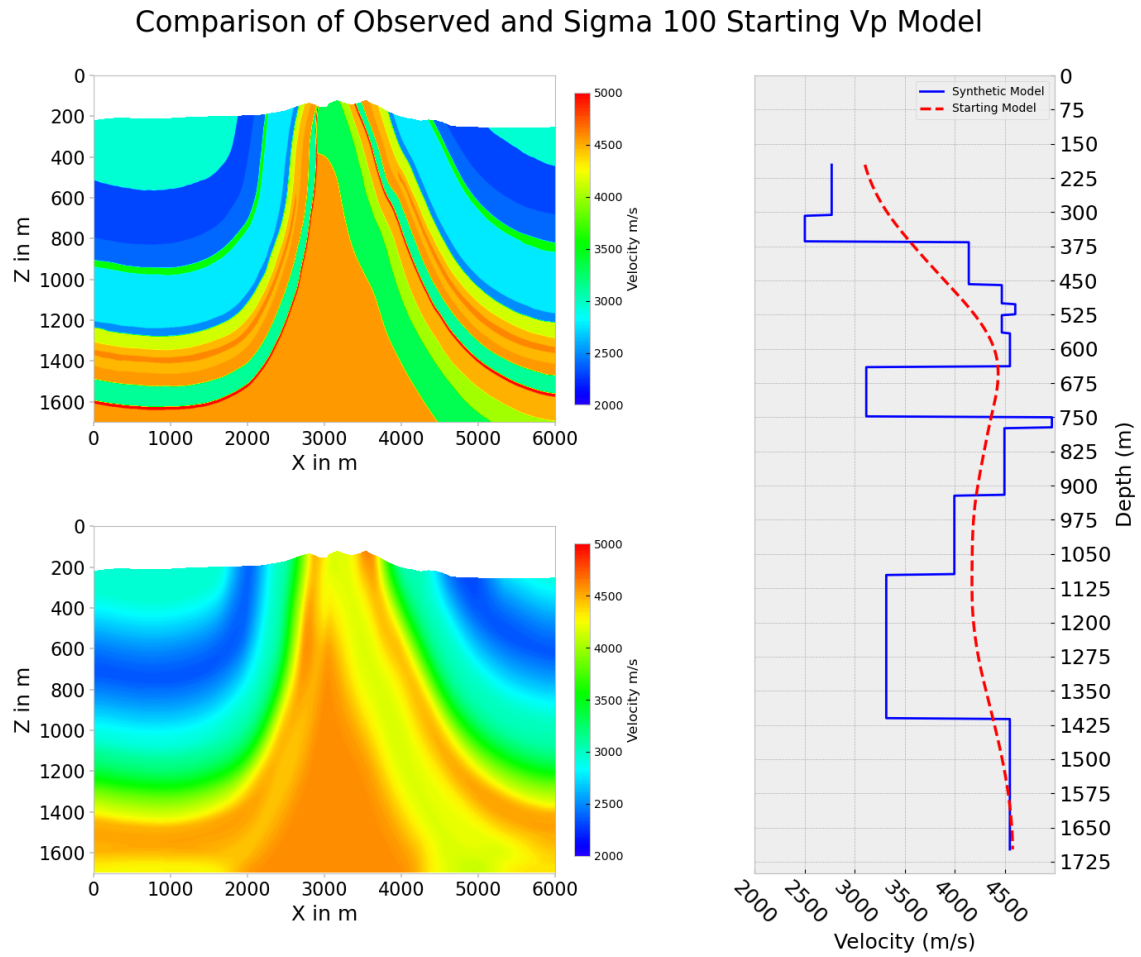


Figure 3.7: Comparison between the observed model and the starting model velocity model. A visual analysis can be made by comparing the images. The velocity profile at 4000 m allows understanding of how the geologic interfaces have changed via smoothing.

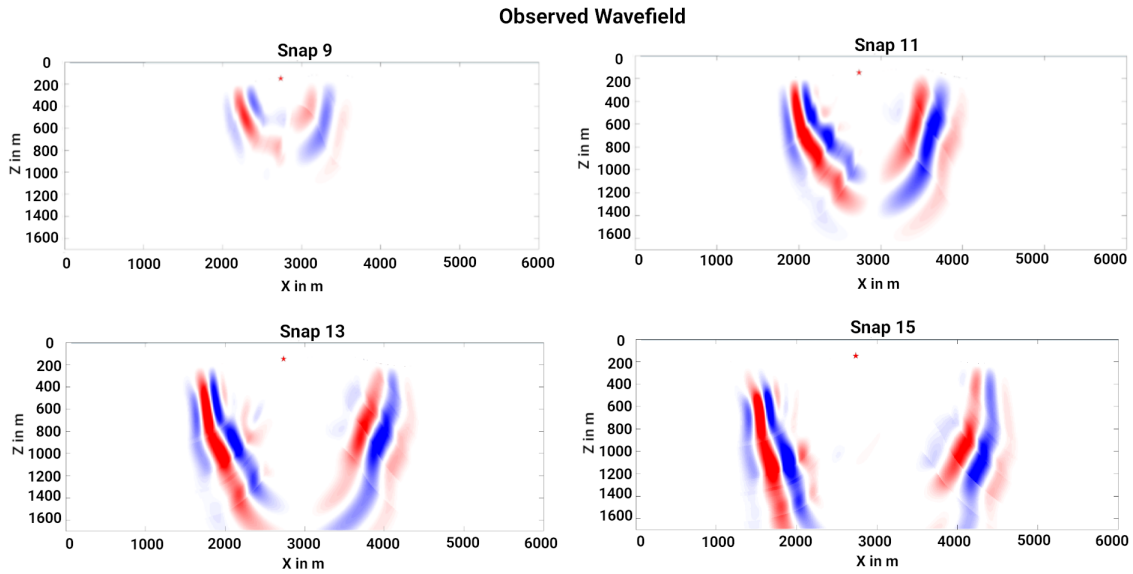


Figure 3.8: Different snapshots of the wavefield from the observed model are displayed. This wavefield is from shot 10 of the 20 shot acquisition geometry. The star represents the source position. It can be seen how the wavefield moves through the different geologic structures of the mine, and thus has a increase or decrease in its travel times. Below is the sigma 100 wavefield with the same snapshots.

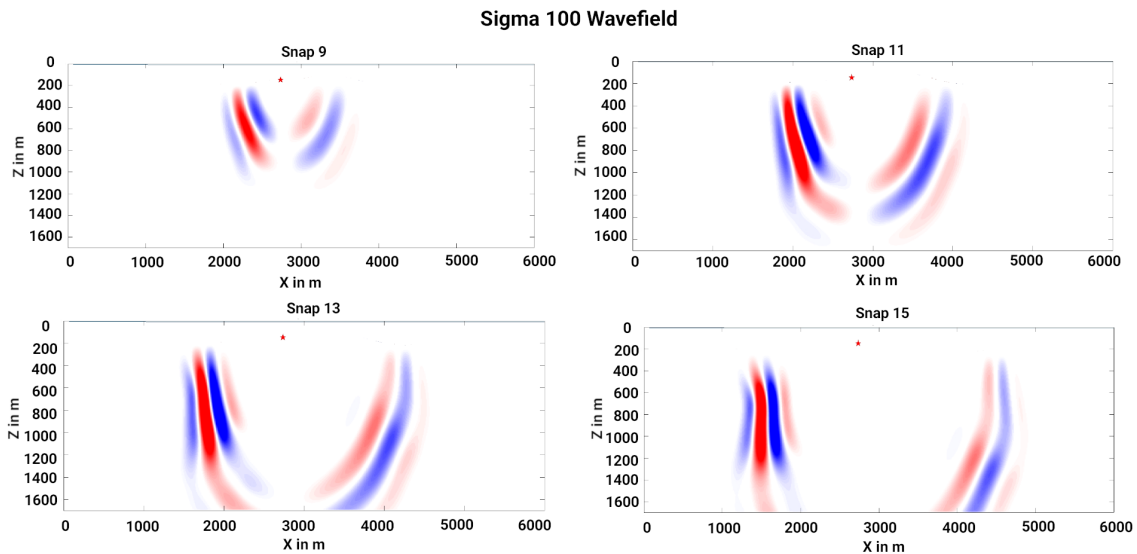


Figure 3.9: Different snapshots of the wavefield from the sigma 100 model. The star represents the source position. Due the smoothing of the interfaces the wavefield experiences less dispersion.

4. Inverse Modeling

Results from various inversions are covered in this chapter. In order to ensure that computationally efficient and accurate modelling was conducted, numerous different inverse modelling parameters were tested. These parameters are shown in table 4.1. Most of the parameters important for having a successful inversion are listed in this table. Other parameters that made significant differences in the inversions were the starting model, acquisition geometry, frequency, and time window. The testing of all parameters was thus split up into two parts. The first, setting the base necessary parameters for an inversion to run and not be too computationally expensive. A description of these is done in the following section. The second, those which focused more on data manipulation within the inversion. The results of these tests were compared when the inversions were completed in order to decide whether they made a difference and in which scenarios they could be applied to improve the results. By varying these parameters an understanding about the integrity and limits of the Asse II Mine Model were made.

4.1 Inversion Parameters

To focus the frequency content of the inversion on a certain bandwidth, a 2nd order Butterworth low pass filter of 5 Hz to 12 Hz was used. During inversions, the designated low pass frequency of 5 Hz was used until an appropriate step length was no longer found. IFOS2D then increased the bandwidth filter by a designated increment. This was done until the upper part of the frequency filter was reached. Using a larger range for the frequency filtering resulted in poor results and inversion instability. For the determination of the step length an initial guess was made and then improved through a process of trial and error. Equation 2.50 is used to determine step length. Here the percentage change and scale factor are the only parameters that can be set. The values for the estimation can be seen in table 4.1. In order to save computational time while testing parameters, 65 iterations were used per inversion. Each iteration made a total of 11 attempts to complete the parabolic line search. If this criteria was not met, the inversion would break off. The only other scenario in which this was the case, was when the abort criteria of an inversion was met. The abort criteria measures the difference of the misfit within the last two iterations. If the change between the two iterations is smaller than the abort criteria, the lower limit of the frequency filter bandwidth of the inversion was increased. If this did not resolve the issue, the simulation would end. In this case the abort criteria was set to 0.0001. For the boundaries between the geologic structures and the free surface, a taper was added to prevent waves from being 'trapped' in the boundary. This phenomena was observed in snap shot movies that were analyzed during parameter testing. Tapers were also applied to all sources in the acquisition geometries. Each source was given a radial taper of 25 grid points.

Table 4.1: The inversion parameters used to conduct full waveform inversion are listed. All parameters were set through trial and error. Keeping computation time in a reasonable time frame was a key element during selection of parameters. The formula to calculate the step length can be found in equation 2.50.

Inversion Parameters	
Iterations	65
Gradient Method	Preconditioned Conjugate Gradient (PCG)
Step Length	Eps scale = 5% Step Max=10 Scalefac = 3
LNORM	Global Correlation
Frequency Filter	Low pass = 5-12 Hz Increment = 2 Order = 2
Abort Criteria	0.0001

The general workflow of an inversion would typically run as follows. A total iteration number is set by the user. During an iteration, forward and backward modelling of the wavefield takes place for all shots within the model. When the modelling portion of the current iteration is complete, the program begins its step length estimation. Here a step length search along the misfit function is performed in order to determine the step length values for the model. After this is complete, the inversion continues to the next iteration. Before further parameters could be tested, the inversion parameters set in this section were assessed with a checkerboard test.

4.2 Checkerboard Test

To check the general stability of the Asse II Mine Model, a checkerboard test was made. In inverse theory checkerboard tests are commonly used to test the reliability of the model, inversion parameters, and the model resolution. By taking the velocity values of the model and adding or subtracting percentages in a pattern that resembles a checkerboard the checkerboard model is created. In this instance, 5% of the values in the model matrix were either added or subtracted to the original velocity values. The goal is ultimately that despite the unusual checkerboard pattern of the observed model, the inversion parameters will be robust enough to recreate it. Failure to do so is indicative of necessary improvement.

The observed checkerboard model created from figure 3.2 can be seen in figure 4.1. Along with the observed model, the inversion results and residuals of the inversion are displayed. The results of the checkerboard as well as the residuals and histogram show that inversion of the checkered pattern was successful. It seems that the only portions of the model that suffered during the assessment were the parts that were deeper than 1400 m for offsets smaller than 1500 m and over 4500 m. This issue may arise due to poor illumination because of acquisition geometry. When viewing the residuals in the third plot of figure 4.1, it can be seen that most of the error in the inversion is along the geologic interfaces.

Further insight into the accuracy of the checkerboard inversion can be gained from

the relative model error (RME). The formula shown in equation 4.1 gives the total percentage difference or error between the inversions and observed synthetic model. It was taken from (Thiel, 2013).

$$\text{RME} = \frac{1}{I \cdot J} \sum_{ij} \frac{|\text{mod}_{ij} - \text{obs}_{ij}|}{|\text{obs}_{ij}|} \quad (4.1)$$

Here *mod* are the inversion models and *obs* is the original synthetic model. *ij* represents the bounds of the model. In this case $i \times j = 850 \times 3000$ grid points. *I* and *J* represent the total grid points for depth and distance, respectively. In order to get the total error and not just the error per depth increment of the model, the matrices containing the velocity values of the models were flattened so that they could be properly summed. The free surface values were not included in the RME calculation. The relative model error of the checkerboard test is 5.37%

4.3 Further Inversion Parameters

To find the best possible inversion, different models and parameters had to be tested in order to further assess the integrity of the model. To do this the source frequency, starting model, acquisition geometry, and time window were changed. Changing these parameters resulted in the increase and decrease of resolution and illumination of the model. The quality of the geologic boundaries, depth resolution, and quality of the inversion were either improved or worsened. In some cases, erroneous artifacts could be removed from the inversions.

4.3.1 Different Frequency Tests

The parameter testing process began with determining a frequency which was reliable and gave the best inversion results. As this is a fundamental part of determining the quality of an inversion, it was the first inversion test. Having an ideal frequency is important due to its impact on the resolution of the inversion. A source with a low frequency, or long wavelength, in theory will have better depth resolution. However, in the case of full waveform inversion, and in this model, these wavelengths will most likely be too long to accurately pick up important details in the observed model. On the other hand, too high of a frequency will result in shorter wavelengths, i.e. more waves, and increase the likelihood that the inversion does not converge due to cycle skipping. The cycle skipping analysis done in section 3.2.2 was done with a source frequency of 6 Hz, however the influence of different frequencies on the inversion was tested as well. The frequencies which can be seen in figure 4.2 are: 2 Hz, 4 Hz, 6 Hz, 8 Hz, 10 Hz, and 12 Hz. These inversions were done with a sigma 100 starting model, and an acquisition geometry of 20 shots. No further alterations were made to the inversion parameters. As it can be seen in the figure 4.2, and as previously stated, the low frequency of 2 Hz has a low resolution quality. Many interfaces which can be seen in the 4-8 Hz inversions are not visible. Conversely, the frequencies of 10 Hz and 12 Hz clearly do not support an accurate inversion process. The frequencies between 4 Hz and 8 Hz show the best model resolutions. The inversions show an increase in detail in order from 4 Hz to 8 Hz. The 8 Hz source frequency inversion shows a high level of desired detail without a decrease in resolution quality. However, with larger acquisition geometries, stability problems were encountered. Thus, a frequency of 6 Hz was ultimately decided upon.

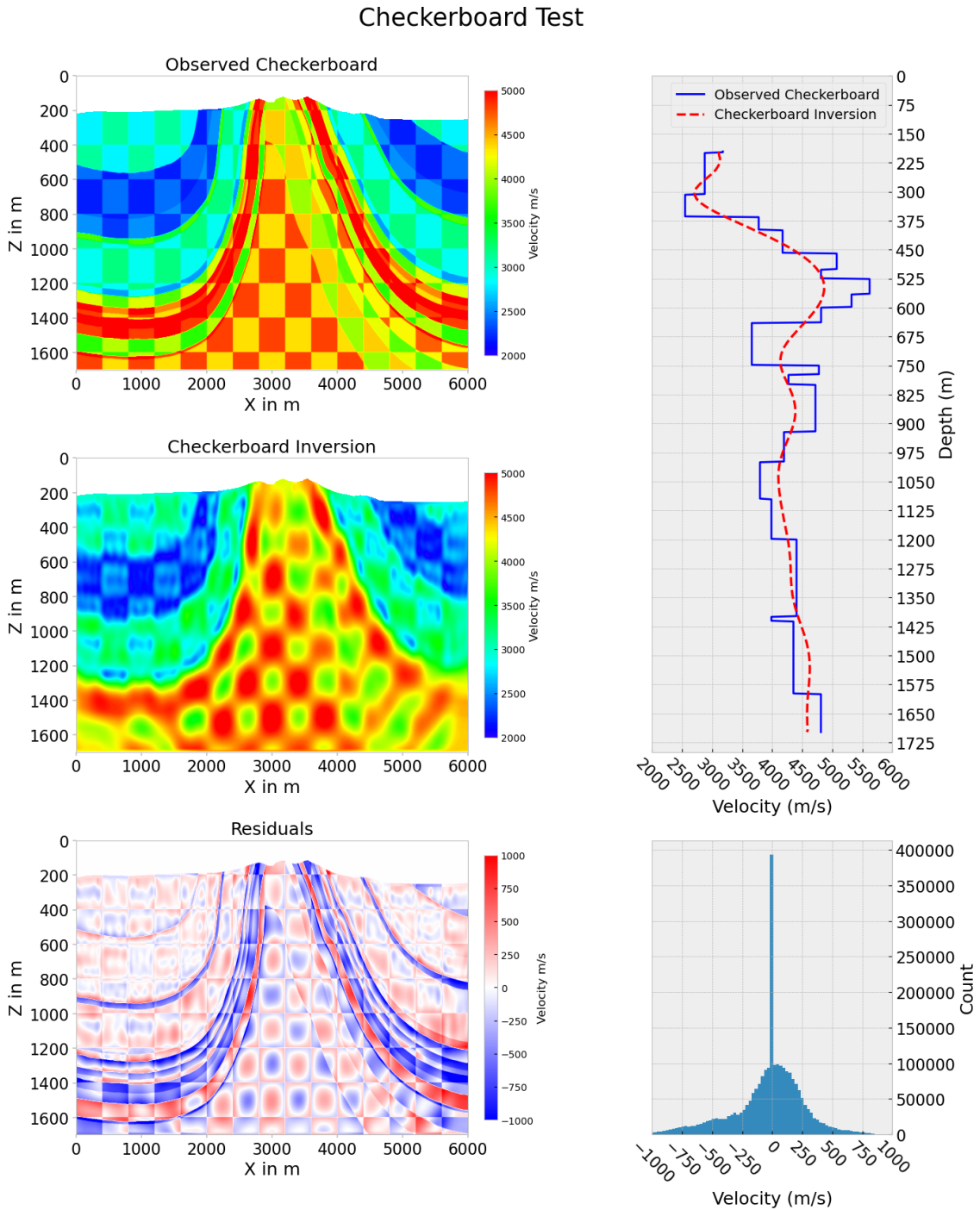


Figure 4.1: In order to test the integrity of the model and full waveform inversion, a checkerboard test was run. The sigma 100 starting model was used for the inversion. The velocity profile is taken at 4000 m. The results are indicative that model is suitable for FWI.

Comparison of Different Source Frequencies

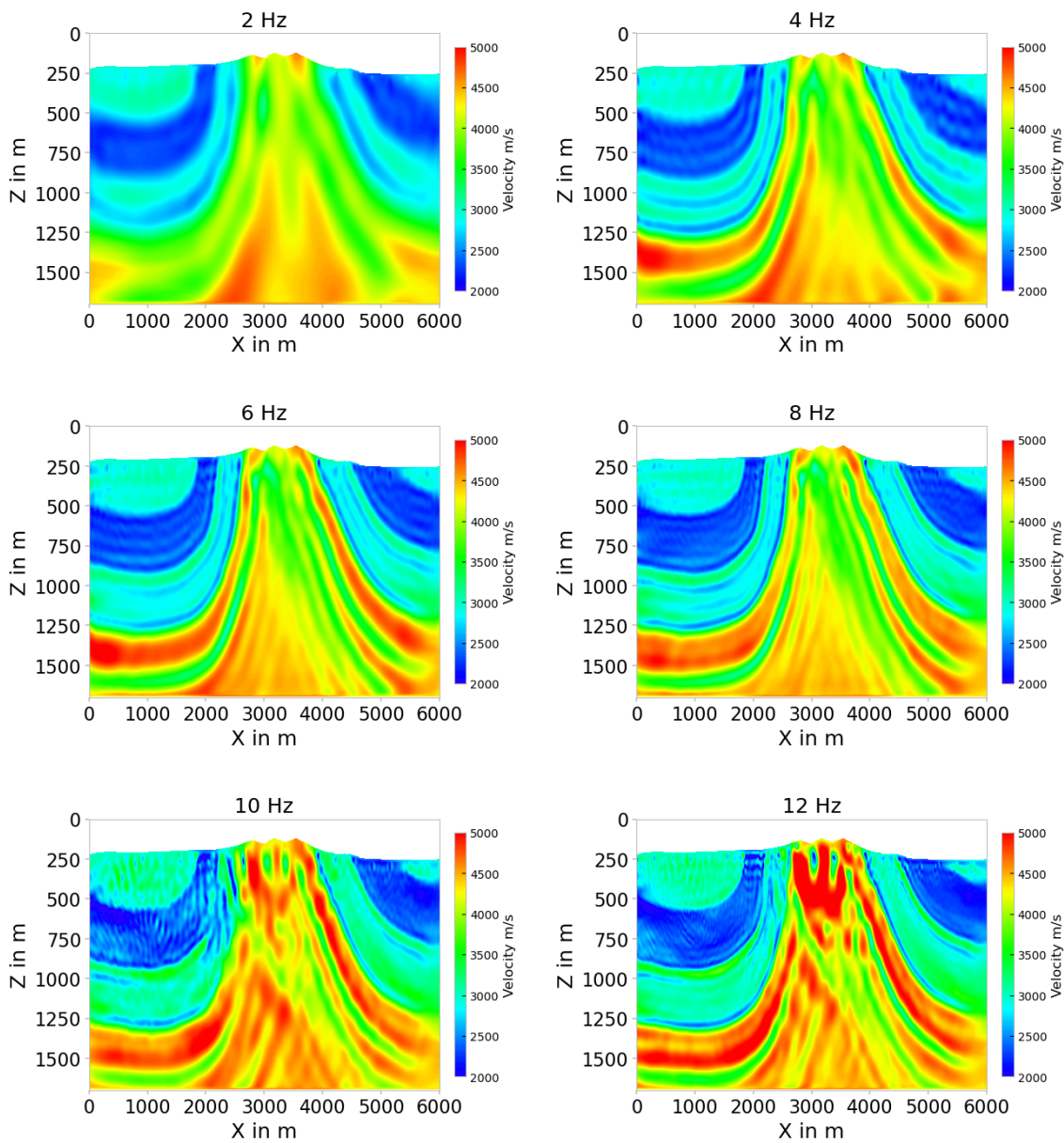


Figure 4.2: A comparison of the inversions with different source frequencies. The plots range from 2 Hz to 12 Hz. It can be seen that frequencies that are too low (2 Hz and 4 Hz), do not show enough detail. On the other hand, higher frequencies such as 10 Hz and 12 Hz do not converge to create a suitable inversion. Ultimately 6 Hz was used as the source frequency as it was more reliable than 8 Hz.

4.3.2 Different Starting Models

As was seen in the cycle skipping analysis in section 3.2.2, the smoothed sigma 100 and 200 seismograms exhibited little to no cycle skipping while the sigma 300 and 400 models seemed more prone. To confirm this conclusion and build the basis for testing done in further sections of this chapter, inversions using different starting models were performed. They can be seen in figure 4.3. Here, all the starting model inversions are compared in order to obtain a comparison of the effect of poor model convergence, and to decide which are fit for further analysis.

Clearly in the figure it can be seen that the sigma 100 and 200 models have inversions with far greater resolution than the sigma 300 and 400 models. All inversions done in this section were done with an acquisition geometry of 20 shots. To test further resolution capabilities of the different starting models, the impact of different acquisition geometries was tested as well. This was done for sigma 100, 200, and 300. The sigma 100 and 200 comparisons are covered in section 4.3.3, while the sigma 300 shot number comparison is shown in the appendix.

4.3.3 Different Acquisition Geometries

As previously mentioned in the forward modelling section, different shot geometries were compared to see whether the number of shots increased the quality of the inversions. All initial tests, as described in previous sections, were conducted with a 20 shot acquisition geometry. This was done in order to reduce computational costs. Further testing was done with 40 shot, 60 shot, 81 shot, and 103 shot acquisition geometries. This was done to see if increased shot number would result in improved interface and depth resolution. This was tested for numerous different inversion parameter combinations.

In figure 4.4 a comparison between a 20 shot and 103 shot inversion with a sigma 100 starting model was made. To simplify the figure, only the simplest, and densest acquisition geometry were used for the comparison. The inversions with the other shot geometries are included in the appendix. Along with the inversions, a residual, velocity profile, and histogram plot are shown. When analyzing the plots in the figure, it is clear that there is little to no improvement between the two acquisition geometries. This is especially clear when viewing the velocity profile and histogram. The velocity profiles are nearly identical and the histogram has approximately 500 000 zero values. In the inversions for both shot geometries, most of the geologic boundaries within the model are well defined, and there is good depth resolution. Unfortunately, the inversions suffer from geologic artifacts between the 4000 m and 5000 m mark. Originally, it was believed that a higher shot geometry would be able to get rid of this issue, however when examining the 20 and 103 shot inversions it is clear that this is not the case. The main improvement from the 20 to 103 shot acquisition geometries is that the low velocity geologic layers in the first 800 m depth of the model are more well defined in the 103 shot geometry inversion. Misfit and step length as a function of iteration number plots for both the 20 shot and 103 shot inversions are shown in figure 4.5. They show that the 65 iterations for the inversions are enough in maximizing the potential of both models, and are not dramatically different between the two acquisition geometries.

To further test the impact of denser acquisition geometries, the same test was done with the sigma 200 starting model. Here it can be seen, that there is a far greater

Inversions of Different Starting Models

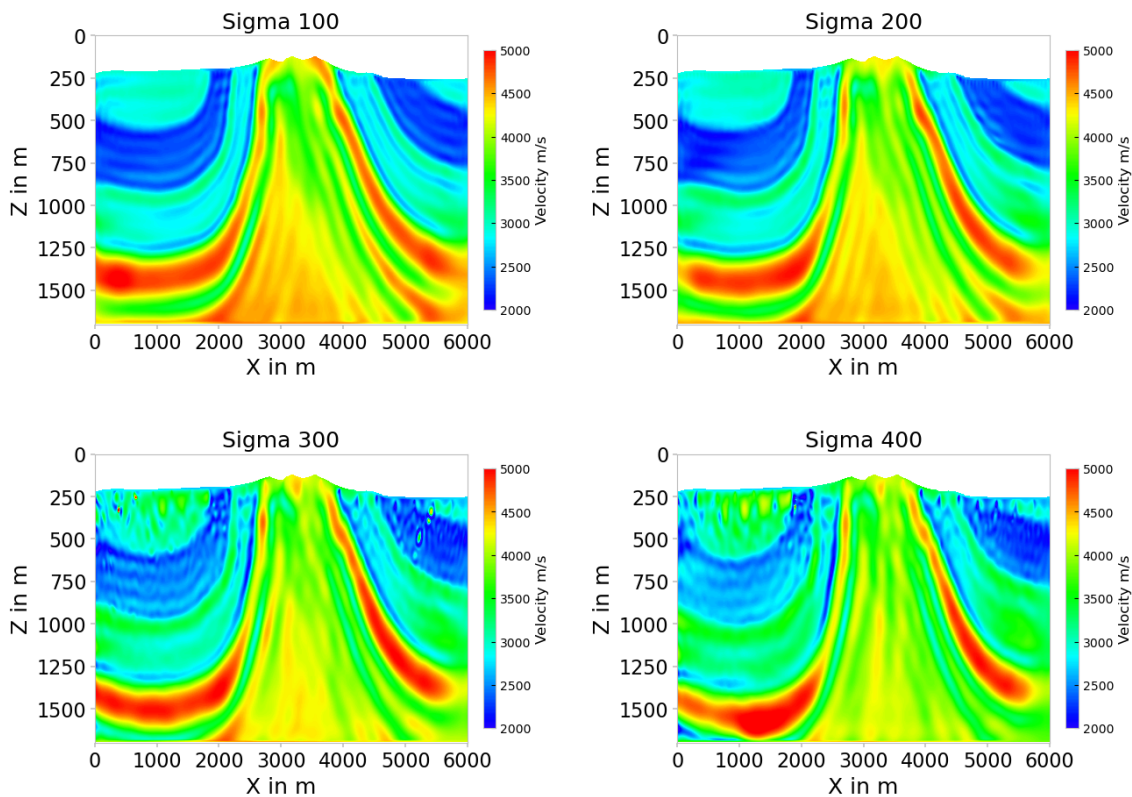


Figure 4.3: Comparison of inversions based on different starting models. The error distribution of each inversion can be seen in figure A.3, respectively. An acquisition geometry with 20 shots, and source frequency of 6 Hz was used for these inversions.

difference between the two acquisition geometry inversions. There is a noticeable improvement to the sigma 100 comparison. In the histogram it can be seen that instead of 500 000 zero values there are about 350 000. This improvement is due to the fact that the inversion from the sigma 200 model is poorer than the sigma 100 inversion. Thus, the denser acquisition geometry yields a greater improvement than in the sigma 100 case. Knowing this, it can be said that while it initially seemed like the acquisition geometry could be a negligible factor, it plays an important role in inversions that are generally less accurate. A similar comparison was done for the sigma 300 starting model, figure A.7, is listed in the appendix.

Comparison of Acquisition Geometriy - Sigma 100 Starting Model

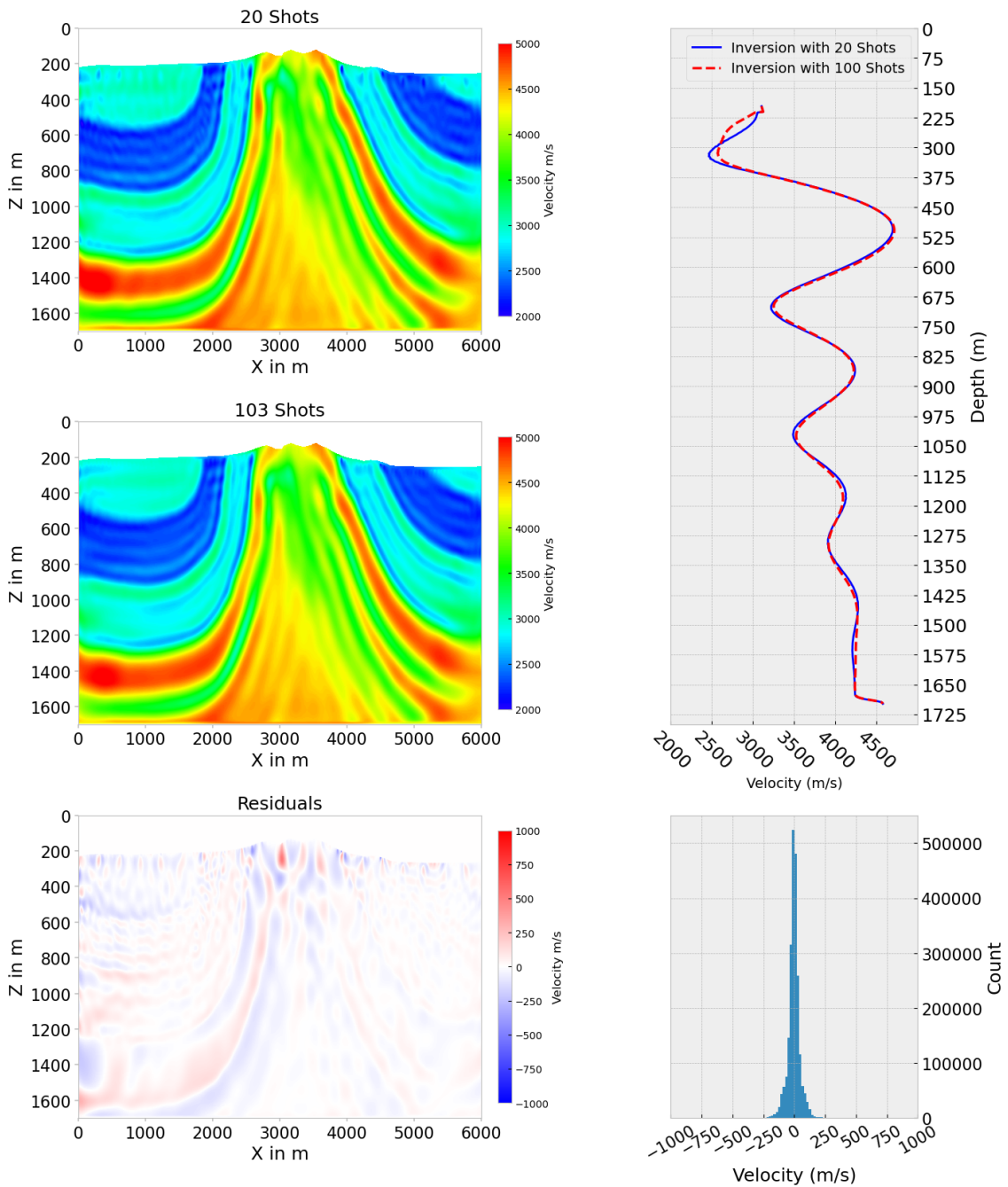


Figure 4.4: Here two inversions are shown. The top left image shows an inversion with acquisition geometry with 20 shots, and the image below has an acquisition geometry with 103 shots. The residuals between the two inversions can be seen below them. It is clear, according to the residual plot, velocity profile at 4000 m, and histogram, that in this case shot geometry does not make a large difference when conducting an inversion.

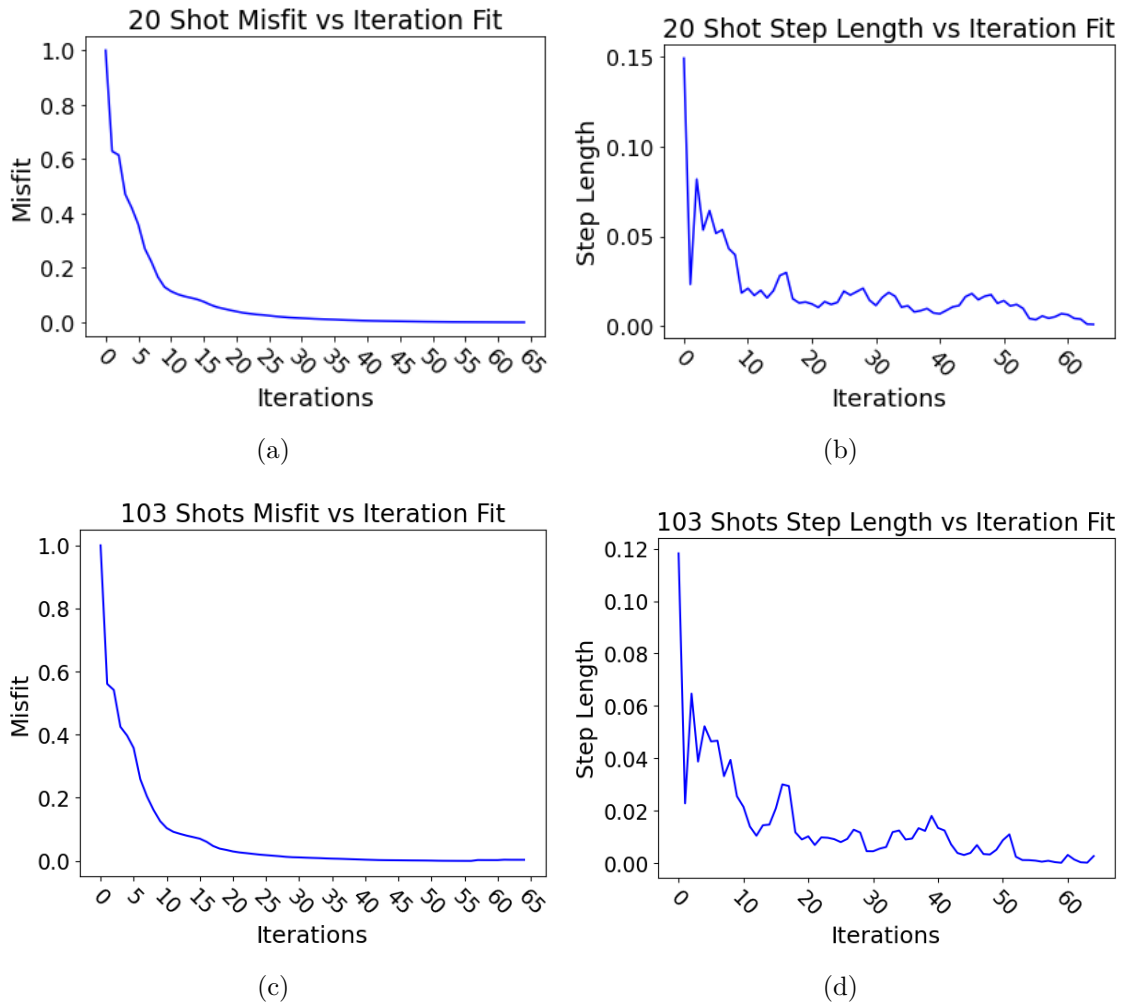


Figure 4.5: Comparison of the data fit of the 20 and 103 shot acquisition geometries. For each acquisition geometry misfit and step length have been plotted in relation to iteration.

Comparison of Acquisition Geometry - Sigma 200 Starting Model

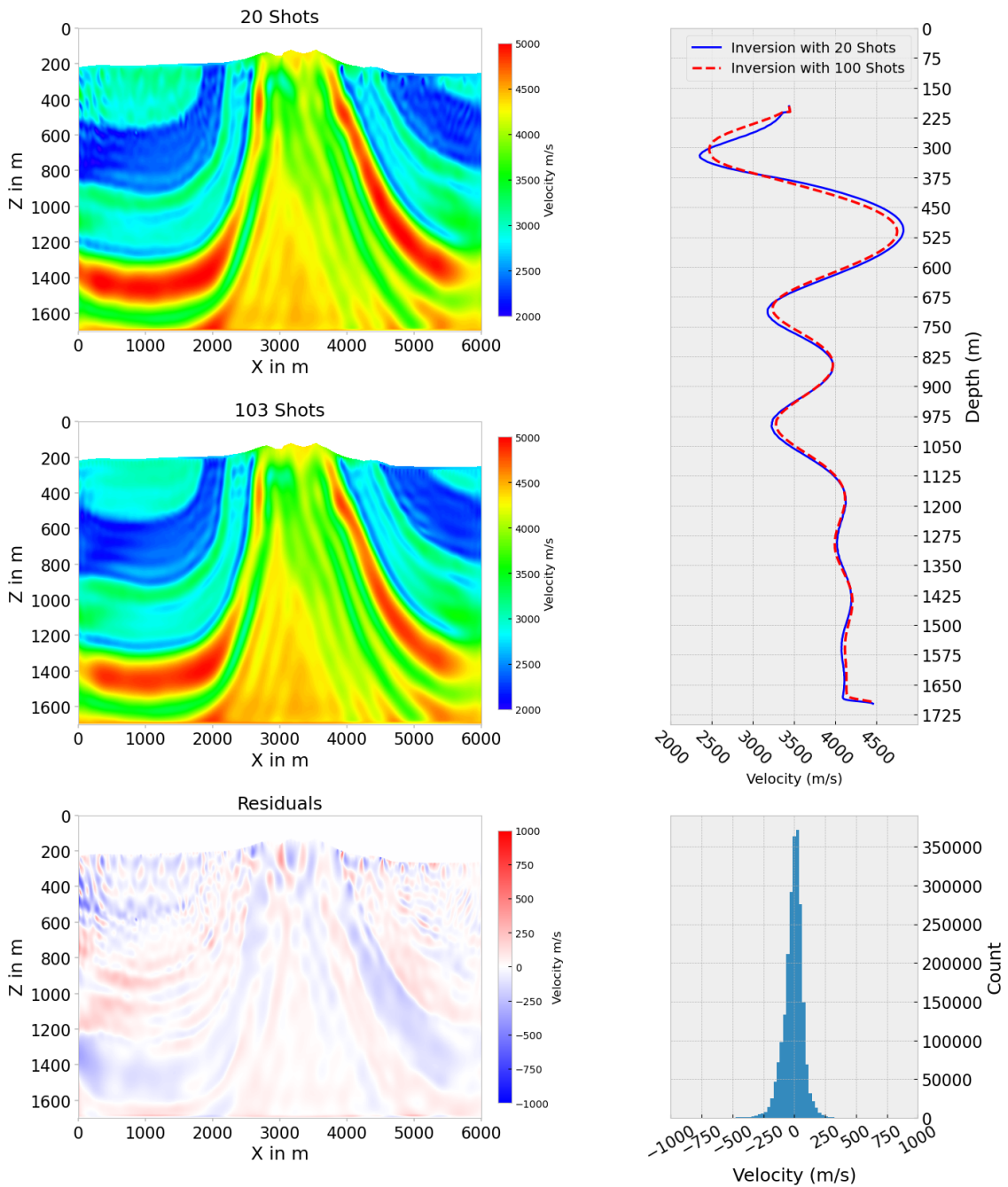


Figure 4.6: Here two inversions are shown for the sigma 200 starting model. The top left image shows an inversion with acquisition geometry with 20 shots, and the image below has an acquisition geometry with 103 shots. The residuals between the two inversions can be seen below them. In this case it can be seen that the denser shot geometry makes a larger impact than on the inversion with the sigma 100 starting model. The profile is located at 4000 m.

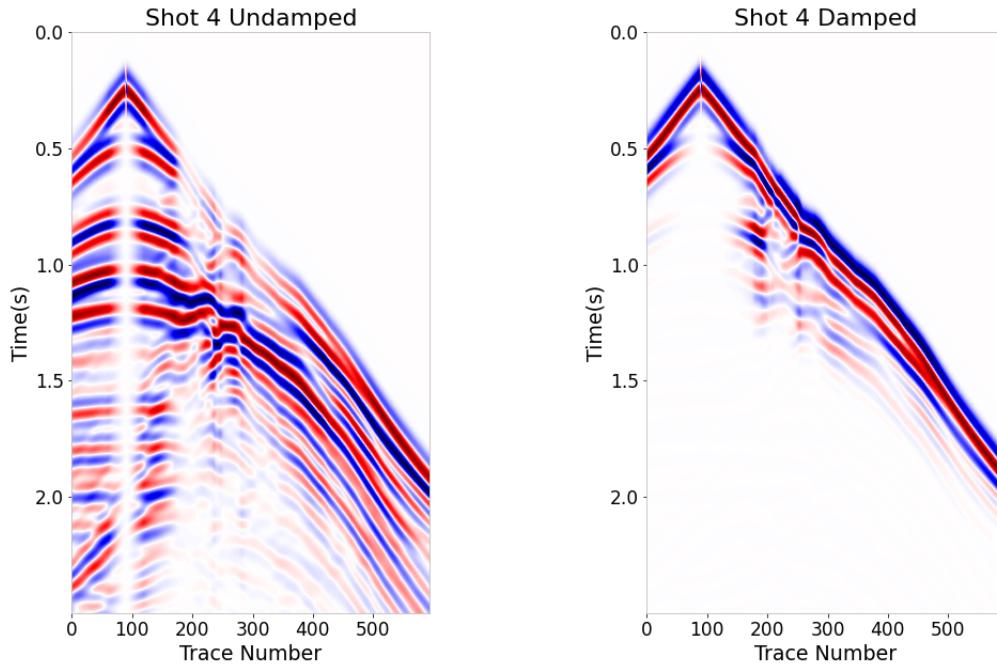


Figure 4.7: Time windowing for shot 4 of the acquisition geometry.

4.3.4 Inversions with Time Windowing

In order to isolate the first arrivals of the shots, time windowing was used in the inversion process. For every trace of every shot, picks were made to determine which portions of the seismic waves would be passed and which would be dampened. All seismic energy outside of the specified time window in equation 4.2 was dampened.

$$d_{damped} = e^{-\gamma t} d \quad (4.2)$$

Here d is data, γ is the damping factor, and t is the time window. In this case, d are the seismograms, γ is 10, and t is 0.2 s. The difference between an undamped shot and damped shot can be seen in figure 4. This same damping was applied to every shot of an acquisition geometry. When analyzing this picture it becomes clear that an inversion with damping will suffer from lower resolution due to the lower amount of seismic energy in each shot. Despite this, time windowing offers the advantage that it strengthens the energy of first arrivals. This is clear in figure 4 as well. The results from damping the shots in an inversion can be seen in figure 4.8.

When comparing the inversions with a time window and without a time window, there are several things that are distinguishable between the two. Firstly, the geologic artifacts present in the inversions without a time window are no longer visible in the damped inversions. This is desirable as it is more similar to the observed synthetic model.

As previously stated, time windowing unfortunately also causes a decrease in model resolution. Some boundaries may become more clear during time window inversions, but overall resolution of the models decrease. This is very clear when examining figure A.6. In general, the edges and deeper part of the model have poorer resolution than the inversions without the time window. The only thing that has improved is the removal of the unwanted geologic artifacts between the 4000 m and 5000 m mark.

Comparison of Without and with a Time Window

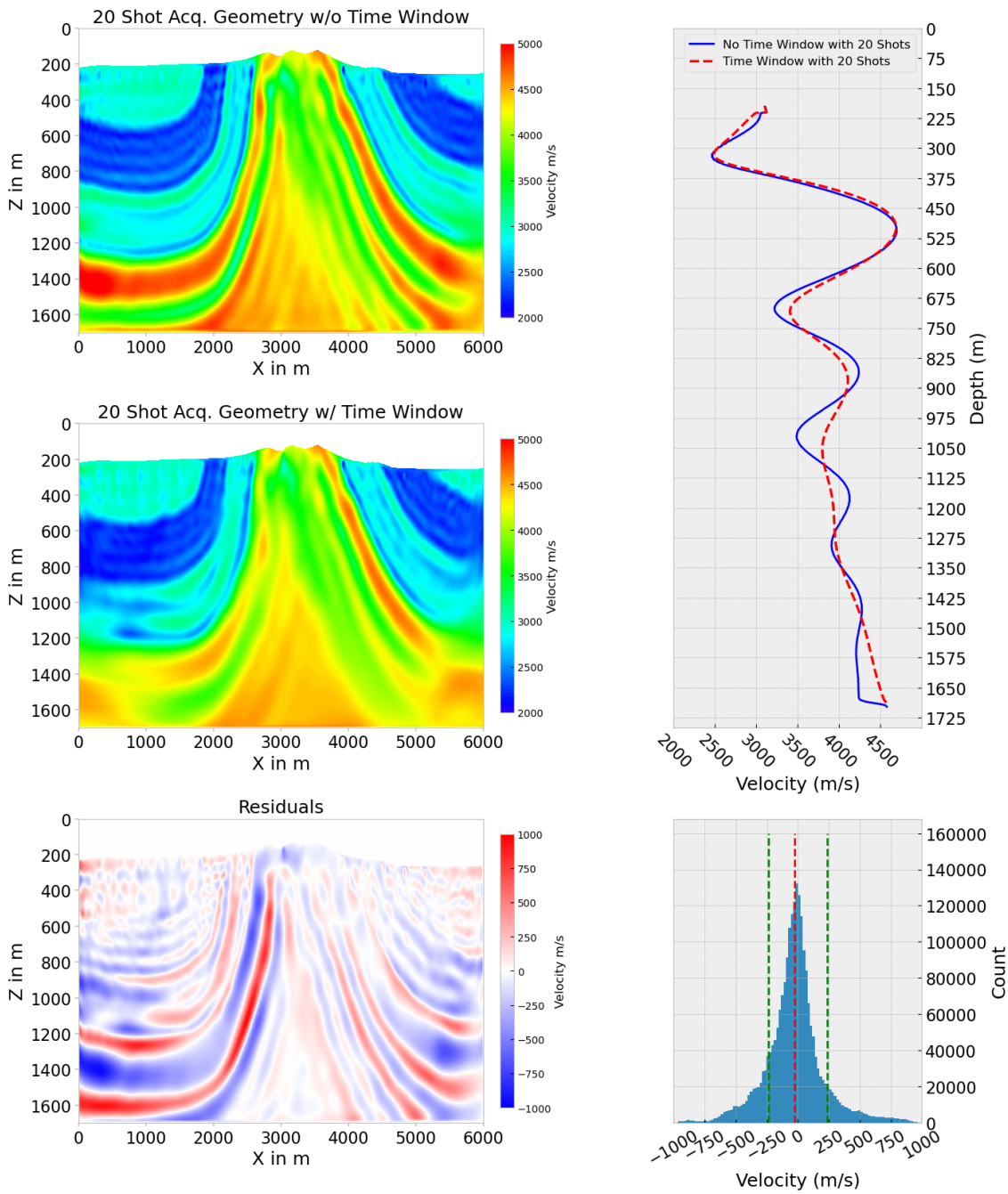


Figure 4.8: A comparison between an inversion without and with a time window. Here an acquisition geometry with 20 shots for both inversions is shown. To get a better understanding between the differences of the two models, the residuals have been plotted. A velocity profile at 4000 m and a histogram have been plotted as well. They show they a considerable difference between the inversions without and with a time window.

Comparison of Shot Geometries with a Time Window

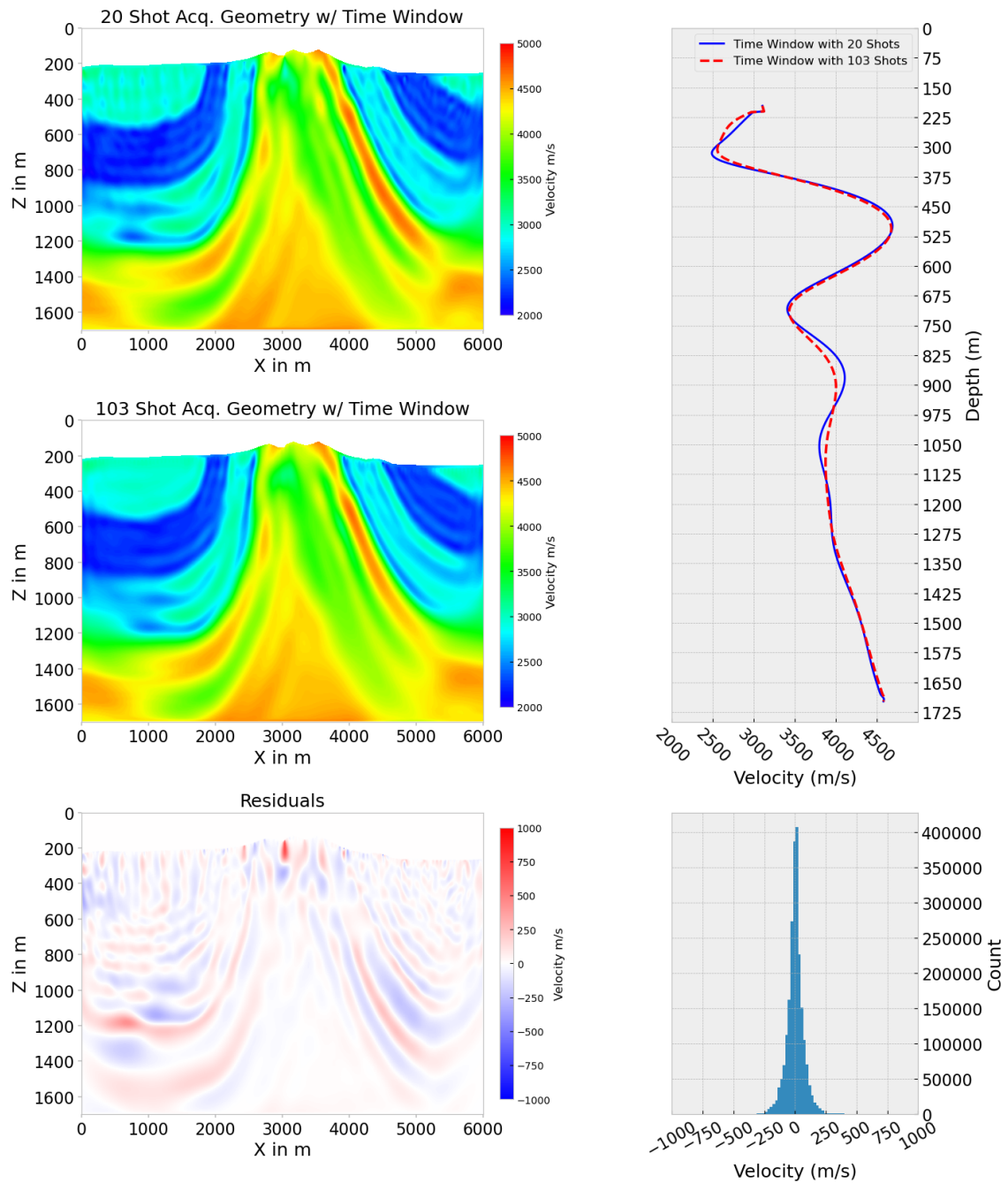


Figure 4.9: A comparison between an time window inversion with different shot geometries. The 20 shot acquisition geometry is shown above and the 103 shot acquisition geometry is shown below. Here it can be seen that a denser shot geometry improves the model more than in an inversion without a time window. In the residual model the greatest residuals occur between 0 m - 2000 m and 4000 m - 6000 m. The histogram in figure 4.4 has count of about 500 000 zeros while this histogram has 400 000. Indicative of a greater improvement from 20 shots to 103 shots than in figure 4.4.

4.4 Comparison to Observed Model

To determine the accuracy of the inversions it is necessary to compare them to the observed model, and analyze the residuals of the two models. For this analysis, the best models from each inversion were compared. The 103 shot inversions for the sigma 100 and 200 models, and time window inversions are analyzed as well as the 103 shot time window inversion. All inversions were compared to the observed model via a visual analysis, velocity profile, residual model plot, and histogram of the residuals. These comparisons can be seen in figure 4.10, 4.12, and 4.11, respectfully.

In the first comparison, figure 4.10, the inversion shows accurate reconstruction of the low velocity layers. These for the most part are the Keuper and Kriede layers. The higher velocity Muschelkalk layers surrounding the Röt formation on the southwest and Bundsandstein on the northeast flank are defined as single high layer velocity layers with well defined boundaries. Between the Muschelkalk and Zechstein salt, the Röt formation and Bundsandstein layers are less well defined. Particularly on the northwest flank, the boundaries between a high velocity Anhydrit and lower velocity Bundsandstein boundary are not well defined. In the inversion, the higher velocity layer, starting at about 5500 m in x and 1600 m in z direction, is only partially resolved. It is more transparent at shallower depths. Close to this partially resolved layer, between 4000 m and 5000 m in the x direction, are geologic artifacts which do not exist in the observed model. The main Zechstein salt formation in the center of the observed model is recreated fairly well. When analyzing the residual model, it can be seen that as explained above, the greatest areas of error lie within the boundaries of the numerous higher velocity Muschelkalk layers, and Bundsandstein on the northwestern flank of the Zechstein. All the interfaces also seem to have a higher degree of error deeper in the model. This would align with the inference that resolution will decrease with depth. The histogram of residuals shows a good distribution that instill confidence in the inversion model.

Continuing on to figure 4.12, it can be seen that the time windowed inversion recreates the main aspects of the geology of the observed model, it is of a lower quality than the inversion without a time window. This however is expected. The lower velocity geologic layers show a poor resolution that takes on the appearance of smearing, and there is less resolution of the geologic structures in the deeper parts of the model. The basic shape of the Muschelkalk and Zechstein high velocity layers are however visible. An improvement from the inversion without the time window is that the high velocity layer between the Bundsandstein and Röt on the northwestern flank is now continuous. In addition, it can be seen that the geologic artifacts between the 4000 m and 5000 m mark are no longer visible. This is an improvement that proves that time windowing an inversion can result in positive developments. The histogram of the residuals has a skewed distribution towards the positive velocities. This is due to the fact that the high velocity layers in the damped inversion are of a lower velocity than the undamped inversion. Here velocities are predominately below 4500 m/s. It seems quite clear that the inversion without a time window better represents the observed synthetic model than the inversion with a time window. A comparison of the traces from the sigma 100 and sigma 200 models to the observed model can be seen in figures 4.13, 4.14, 4.15, 4.16, and 4.17.

The final comparison, figure 4.6, generally looks similar to the comparison made in figure 4.10. However when looking at the residual model and histogram it is clear

that the sigma 200 starting model recreates a less accurate inversion than the sigma 100 starting model. The histogram of figure 4.6 shows less zero values and higher count of residuals than the histogram in the sigma 100 inversion comparison.

The error for the inversions has been included in table 4.2. It can be seen that the inversion with no time window has an error of 6.7%, the time window inversion 7.6% error, and the sigma 200 starting model inversion has an error of 8.3%. These percentages align with previously stated observations that were made from analyzing figures 4.10, 4.12, and 4.6.

Table 4.2: The relative model error of the best inversion for each investigated scenario. Equation 4.1 is used to calculate the error.

Relative Model Error	
Model	Error
103 shots Sigma 100 65 iterations Center frequency = 6 Hz No Time Window Frequency Filter = 5-12 Hz	6.7%
103 shots Sigma 200 65 iterations Center frequency = 6 Hz No Time Window Frequency Filter = 5-12 Hz	8.3%
103 shots Sigma 100 65 iterations Center frequency = 6 Hz Time Window Frequency Filter = 5-12 Hz	7.6%

Analysis of Sigma 100 Inversion

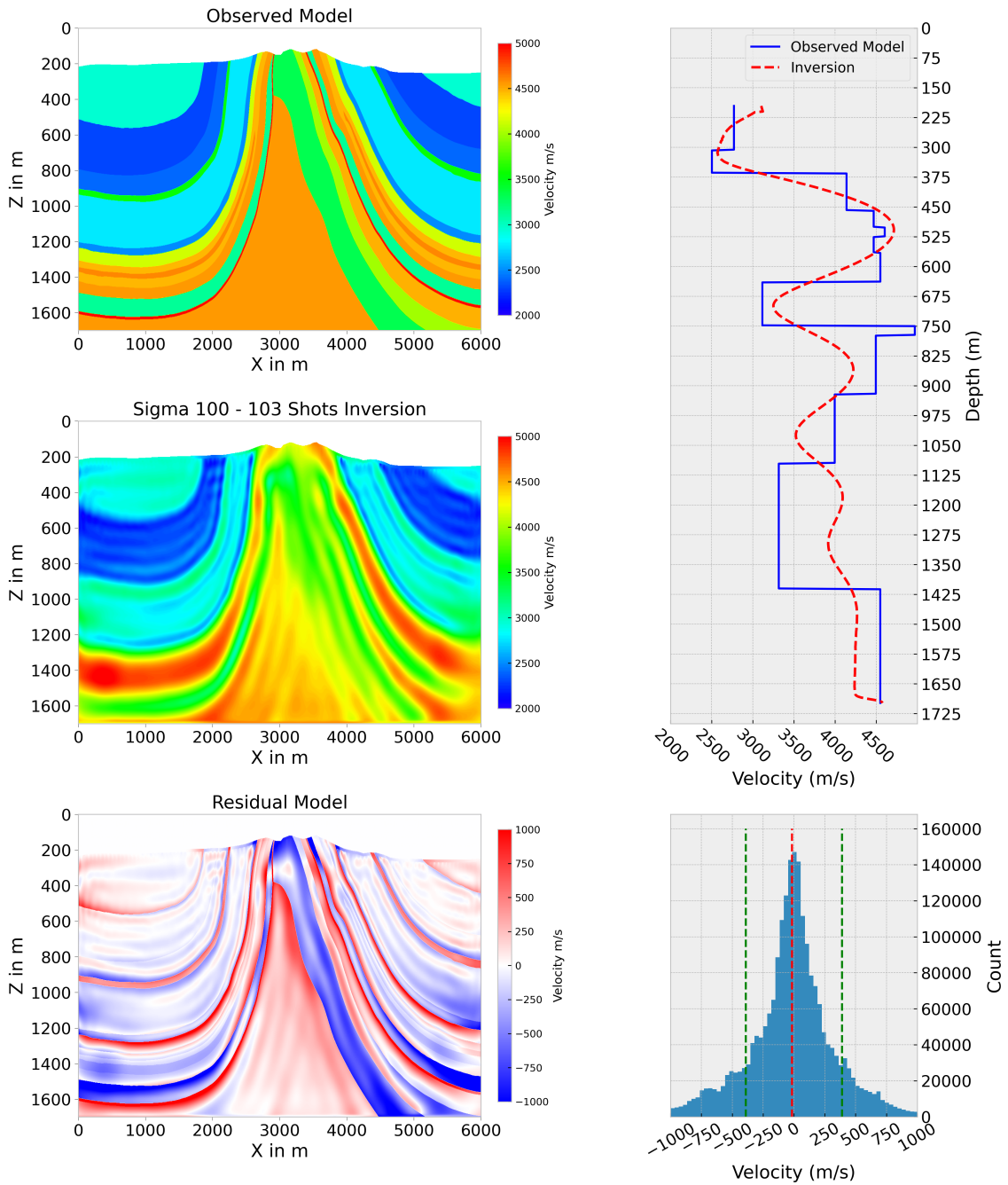


Figure 4.10: A comparison between the observed synthetic model and an inversion without a time window. An acquisition geometry with 103 shots is shown. The residuals of the comparison are shown below the models. A histogram of the residuals, and a velocity profile at 4000 m is shown as well.

Analysis of Sigma 200 - 103 Shots Inversion

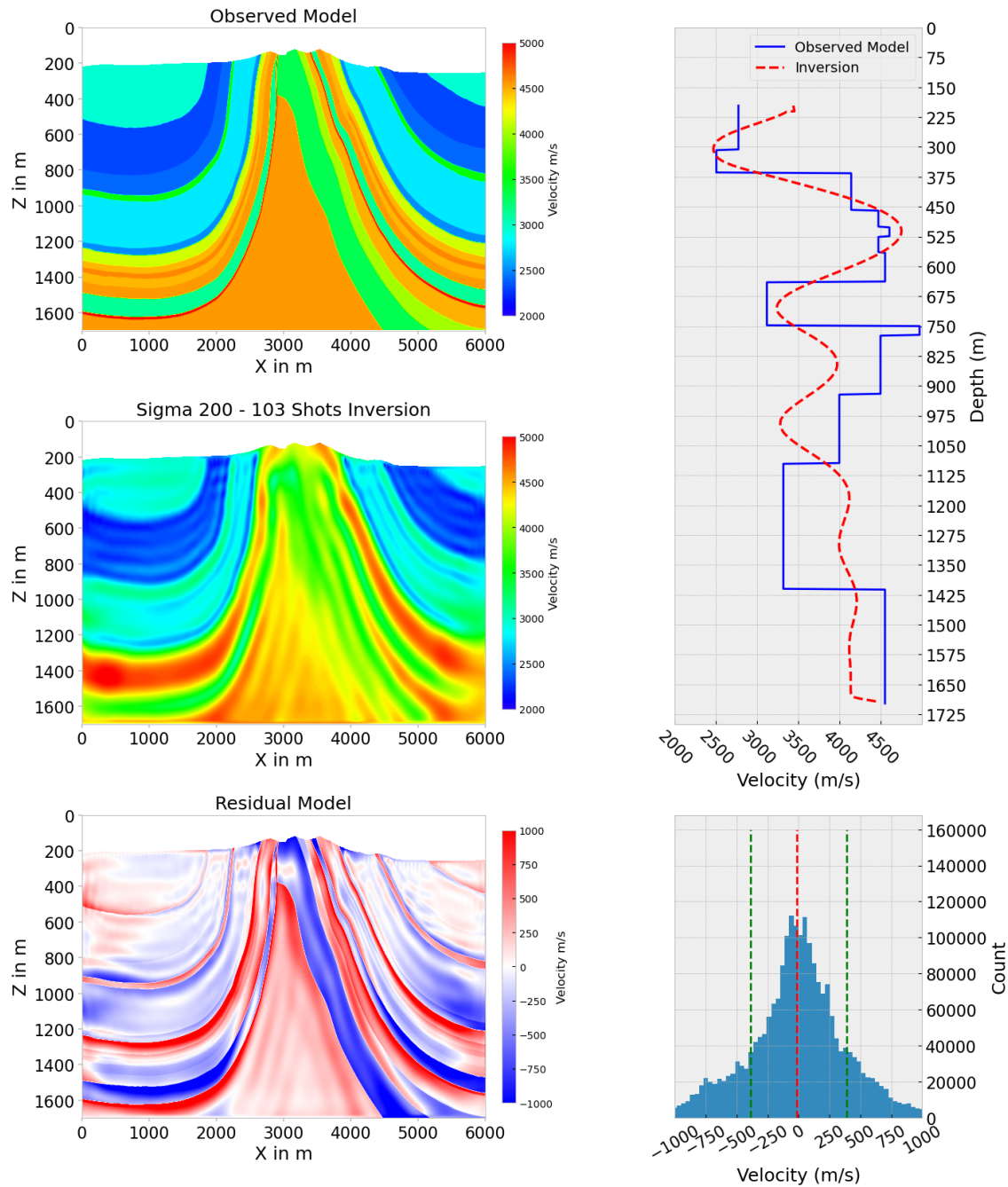


Figure 4.11: A comparison between the observed synthetic model and a sigma 200 inversion without a time window. An acquisition geometry with 103 shots is shown. The residuals of the comparison are shown below the models. A histogram of the residuals, and a velocity profile at 4000 m is shown as well.

Analysis of Sigma 100 - 103 Shots Time Window Inversion

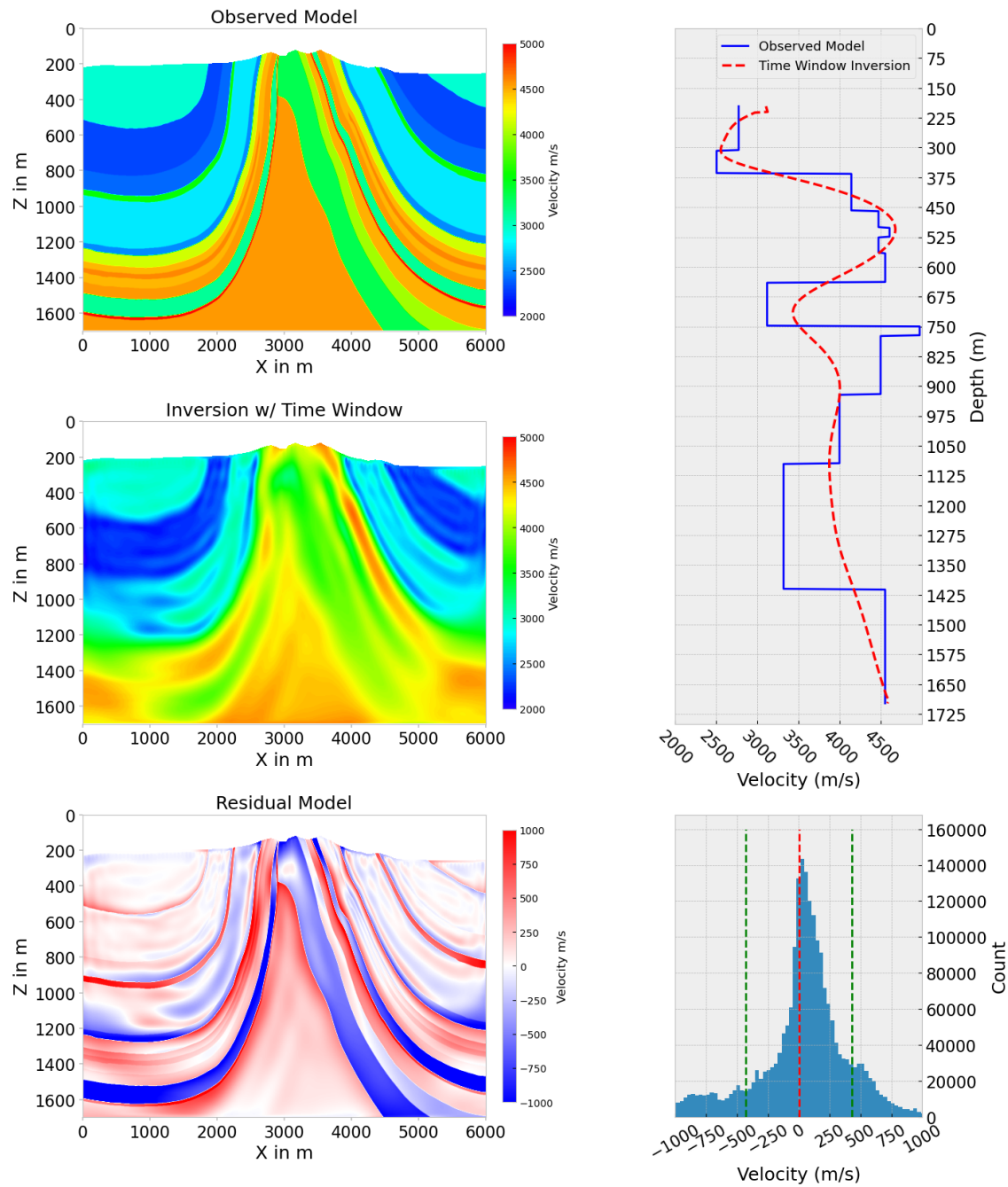


Figure 4.12: A comparison between the observed synthetic model and the the window inversion. An acquisition geometry with 103 shots is shown. The residuals of the comparison are shown below the models. A histogram of the residuals, and a velocity profile at 4000 m is shown as well.

Obs. vs Sigma 100 Inv. Traces

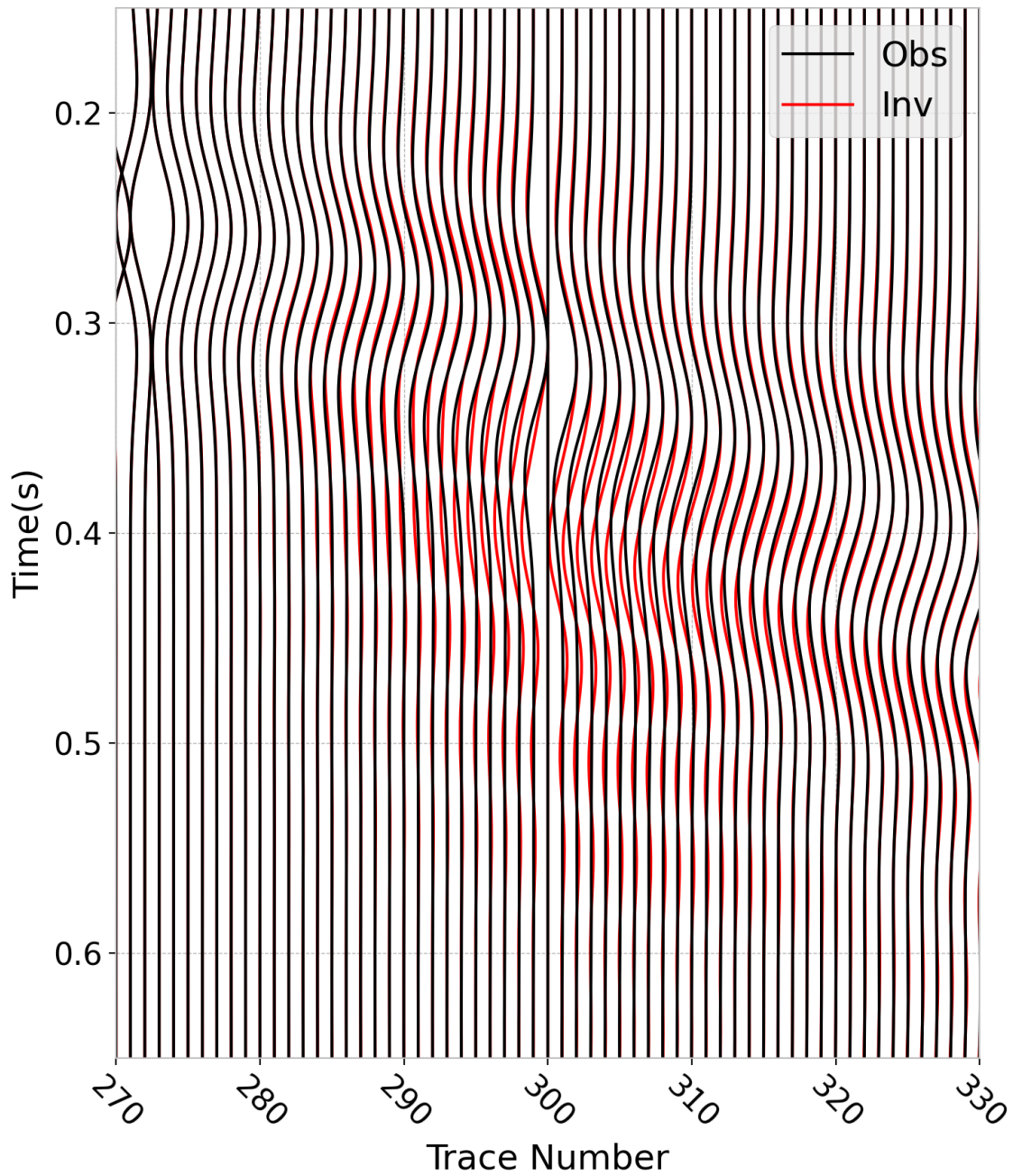


Figure 4.13: Here is a comparison of a range of traces from 270 to 330 are shown. The intention of this plot is to show the similarity of the traces from the observed to the sigma 100 inversion traces. A more detailed comparison is shown in figure 4.14 and 4.15.

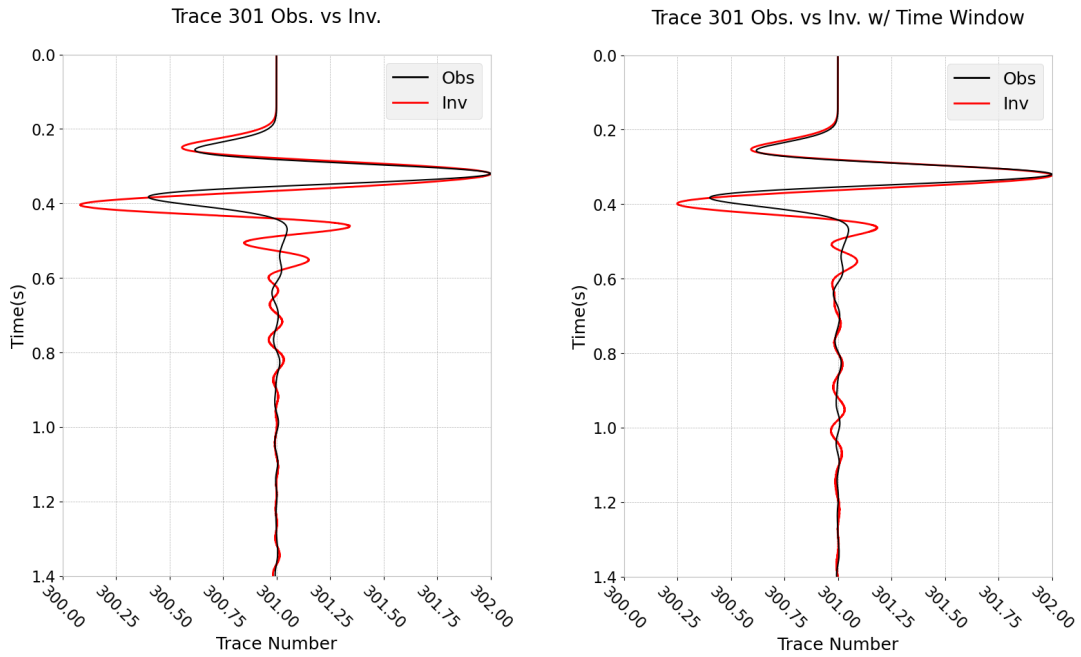


Figure 4.14: A comparison of trace 301 of the observed model and two sigma 100 inversion models from shot 10. When comparing the two plots it can be seen that while the first arrival of the time windowed inversion fits the observed trace better.

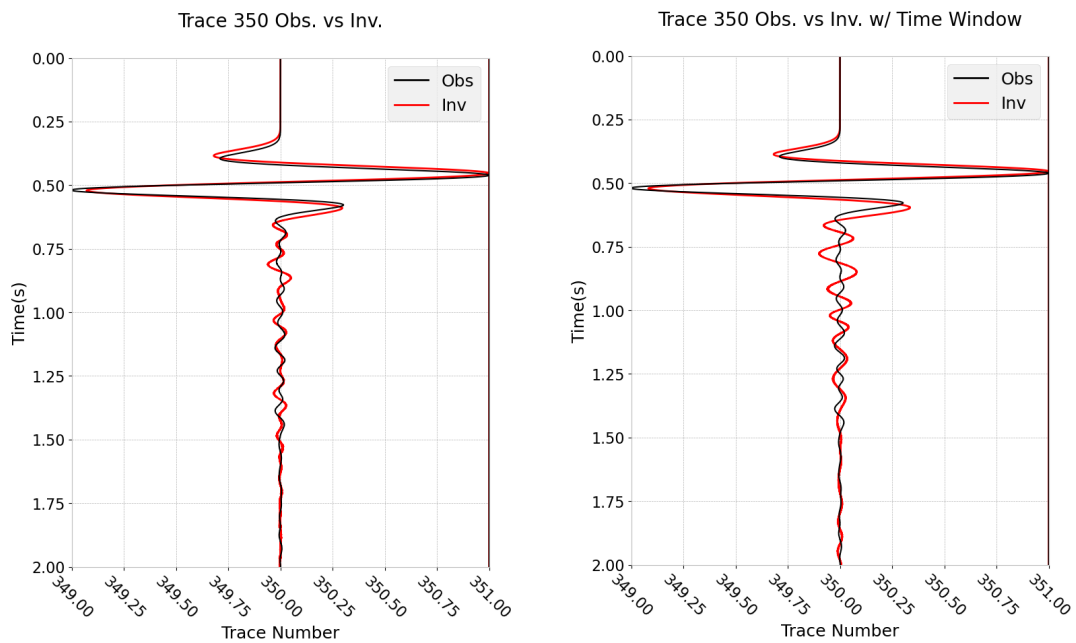


Figure 4.15: A comparison of trace 350 of the observed model and two sigma 100 inversion models from shot 10. When comparing the two plots it can be seen that as in figure 4.14 the first arrival of the time windowed inversion fits better. However, beyond the first arrival, in the 0.5 s to 1.5 s range, the inversion without a time window fits the observed trace better.

Obs. vs Sigma 200 Inv. Traces

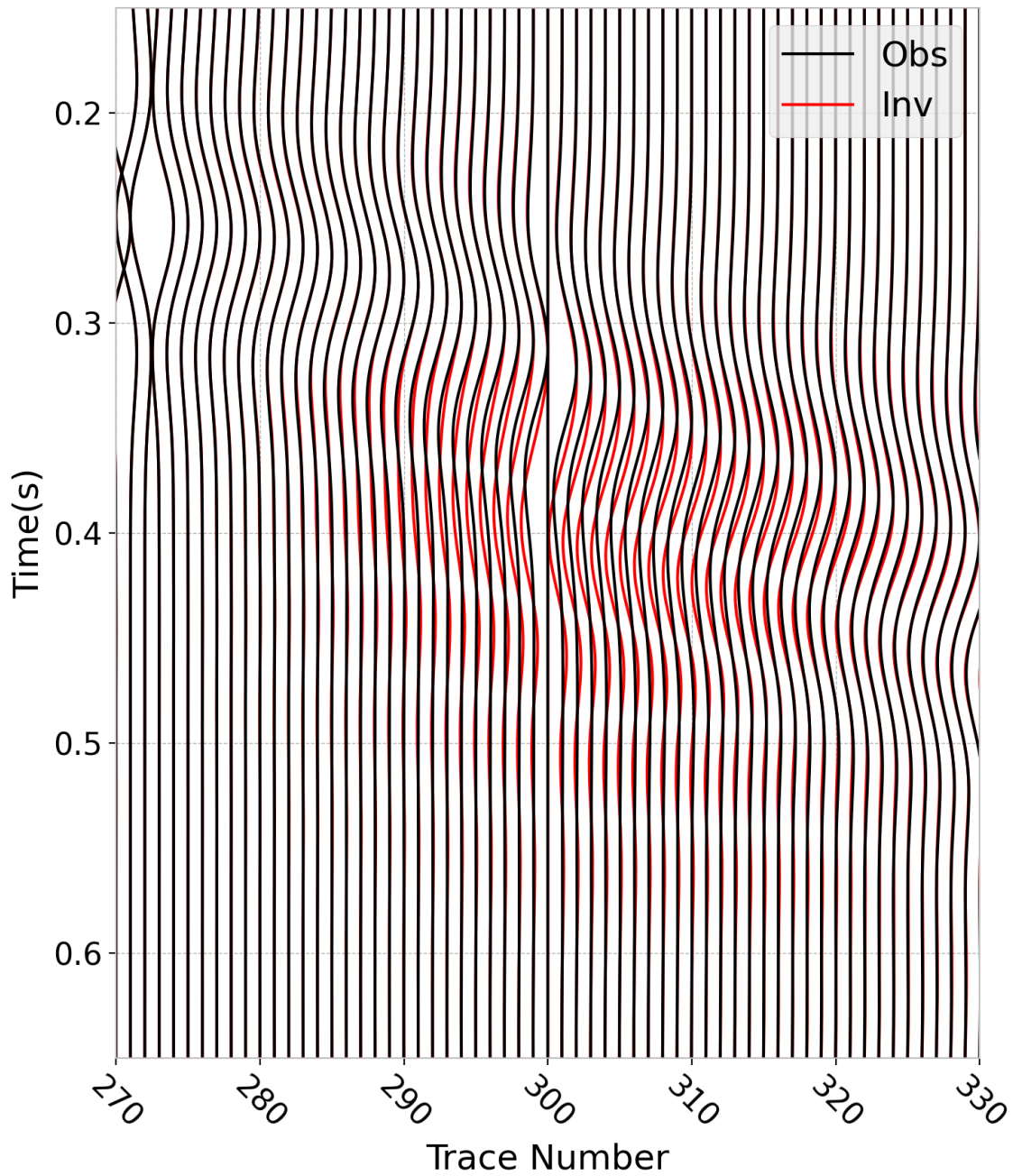


Figure 4.16: Here a comparison of a range of traces from 270 to 330 for the observed and sigma 200 model is shown. The intention of this plot is to show the similarity of the traces from the observed to the sigma 200 inversion traces, and the difference between the sigma 100 and 200 model traces. A single trace from this figure is shown in figure 4.17.

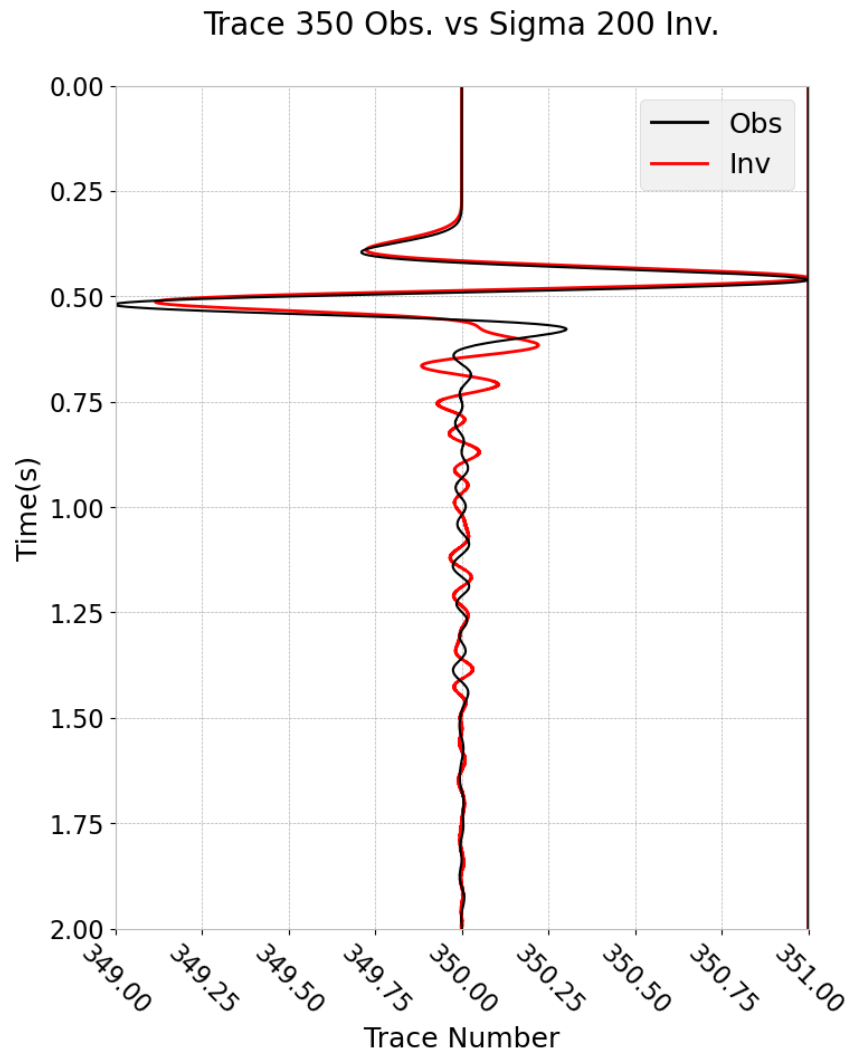


Figure 4.17: A comparison of trace 350 of the observed model and the sigma 200 inversion model from shot 10. When comparing this plot to trace 350 of the sigma 100 no time window inversion, it can be seen that the first arrival is better than that of the sigma 100 inversion trace. However from 0.6 s to 2.0 s the sigma 200 trace is less accurate than the sigma 100 trace.

5. Conclusion & Outlook

The inverse modelling results that were obtained are indicative that the Asse II Mine Model is capable of handling FWI problems. The results distinctly show that the inverse modelling performed in this thesis had adequate illumination and depth resolution to resolve the geologic features. By targeted manipulation of the inverse parameters, precise inverse models were produced. To properly expand on the understanding and relationship of FWI and the Asse II Mine Model, the following should be taken into account.

During inversion parameter testing, inversion with a varying number of total iterations should be done. While this initially may be very time expensive, an analysis of the misfit and step length afterwards will reveal the iteration at which misfit and step length no longer change. Thus a decision on the proper iteration number can be made. The gradient method and LNORM, should be decided based upon the type of inversion being conducted. This can be determined by reading literature of similar studies or through a trail and error approach. For most FWI tests a L2 norm is used. To determine the appropriate step length, it was found that the Eps scale percentage of between 1% - 5% gave the best search results. A step max and scalefac should be determined that does not cause the simulation to break off, but allows the program enough time to search for a misfit. To determine an appropriate frequency filter, view the amplitude spectrum of the shot frequency. The range of the frequency of the shot can be used as a guideline for determining the frequency filter. Using a wide or improper range for frequency filtering will result in poor inversion results. In regard to the abort criteria, a small percentage which allows the simulation to run, but draws a limit to the percentage of change accepted by the user should be implemented.

To determine a stable shot frequency a range of frequencies from 2 Hz to 12 Hz was tested. Only lower frequencies were tested as is practice in full waveform inversion. Ultimately, a shot frequency of 6 Hz was the most stable and gave the best result. This frequency returned detailed inversions that converged for all shot geometries and model parameters. A frequency of 8 Hz was considered, however when using a acquisition geometry higher than 20 shots the inversions became unstable. Smoothing functions for creating starting models should not exceed a window size of about 400 grid points. Window sizes larger than this could cause cycle skipping. The starting models used in this thesis were sigma 100 and 200 models.

The best illumination for all different models was obtained by using the densest reasonable shot geometry possible. In every case, there was an improvement when using the 103 shot acquisition geometry. This percentage of improvement varied depending on the starting model sigma value, and whether or not time windowing was active. Thus, if computational time is not a limiting factor, then using a denser acquisition geometry is always beneficial. When dealing with unwanted artifacts,

time windowing can be advantageous. The emphasis on first arrivals and damping of later seismic energy will lead to poorer resolution but can also lead to unexpected improvements. To properly implement the windowing effect, a small value for time is encouraged as the focus is to isolate the first arrivals. Anything between the 1.0 s to 2.0 s range is encouraged. The dampening strength depends on the variable gamma. In some cases, gamma may be squared or cubed. This will greatly influence the dampening strength and should be checked before implementation to avoid confusion. In this thesis, below the 1200 m mark the resolution of the model began to decrease significantly. However, despite the resolution difficulties, the model was successful in removing unwanted geologic artifacts between the 4000 m and 5000 m mark. By combining these inversion parameters; reliable shot frequency, a dense acquisition geometry, various starting models, and a fitting time window, the model resolution of an inversion can be properly tested.

Due to the dense grid spacing of the Asse II Mine Model, a high computational time was necessary for running simulations on the model. The 3000 by 850 grid point model was split into thirty, 100 grid point blocks in the x direction and five, 170 grid point blocks in the z direction. The computational time was also influenced by the shot number and iteration number. For a 20 shot inversion with 65 iterations, about 24 hours were needed for an inversion. While a 100 shot inversion with 100 iterations could take up to 4 days. These computation times could be shortened significantly by increasing the grid spacing.

The models and insight gained from the FWI done in this thesis has further increased the understanding of what is possible with the Asse II Mine Model. It opens the door to future use of full waveform inversion in understanding the model of the mine. Future studies could use this thesis as an expansion into numerous directions. A look into elastic modelling of the Asse II Mine Model could be possible. There tests with anisotropy and attenuation would have varying results with potentially more error than the inversions done in this study. In this case, some inversion parameters may have to be changed due to elastic modelling. Other ways to build upon what has been done in thesis are an expansion into a 3D version of the Asse II Mine Model and an application to field data. If this were to be done for the acoustic case, many of the parameters used in thesis could potentially be used.

In conclusion, the results obtained from the FWI conducted in this thesis outlines the potential of this technique in enhancing our comprehension of subsurface environments within the context of the Asse II Mine Model. The robustness demonstrated by the FWI, coupled with the insights gained, not only advances our understanding of FWI and the area, but also paves the way for future applications.

6. Acknowledgements

All of this would not have been possible without the support of my family. They encouraged and supported me on this journey of moving from the United States to Germany to obtain my masters of science. Without their support, the idea of continuing my studies in Germany would never have become a reality. I would like to thank Professor Thomas Bohlen, Dr. Thomas Hertweck, Dr. Laura Gassner, Dr. Lars Haupt, and all further staff at the Karlsruhe Institute of Technology Geophysics Institute. Their patience and knowledge gave me the guidance to work through the challenges and unexpected hurdles that I encountered during my time here at the institute. Furthermore, I would like to thank the other masters students that I met during my time here. Their friendship and presence helped me get through the challenges accompanied with moving to a new country. Lastly, I would like to thank my girlfriend Anni for her support during this academic journey.

Bibliography

- Bohlen, T. (1998). „Viskoelastische FD-Modellierung seismischer Wellen zur Interpretation gemessener Seismogramme“. PhD thesis. Christian Albrechts Universität zu Kiel.
- (2022). „Full Waveform Inversion“. Full Waveform Inversion lectures notes.
- Brandes, C., C. Schmidt, D.C. Tanner, and J. Winsemann (2013). „Paleostress pattern and salt tectonics within a developing foreland basin (north-western Subhercynian Basin, Northern Germany)“. In.
- Brink, H.-J. (2011). „The crustal structure around the Harz Mountains (Germany): review and analysis“. In.
- Bundesamt für Strahlenschutz (2016). *Atlas Asse*. Collection of reports, stories, graphics.
- Bundesanstalt für Geowissenschaften und Rohstoffe (2014). *3D geological model of the Asse salt structure*. Last Access: 17.12.23. URL: https://www.bgr.bund.de/EN/Themen/Endlagerung/Projekte/Endlagerstandorte/laufend/3D-Lagerstaettenmodell_Asse_en.html?nn=12006608.
- Bundesgesellschaft für Endlagerung (2023). Last Access: 15.12.23. URL: <https://www.bge.de/de/>.
- Bundesministerium für Umwelt, Naturschutz, nukleare Sicherheit und Verbraucherschutz (2013). *Lex Asse*. Last Access: 12.12.23. URL: <https://www.bmu.de/themen/nukleare-sicherheit/endlagerung/schachtanlage-asse-ii>.
- Cacace, M., U. Bayer, and A. Marotta (2009). „Late Cretaceous–Early Tertiary tectonic evolution of the Central European Basin System (CEBS): Constraints from numerical modelling“. In.
- Choi, Y. and T. Alkhalifah (2012). „Application of multi-source waveform inversion to marine streamer data using the global correlation norm“. In: *Geophysical Prospecting* 60, pp. 748–758.
- Courant, R., K. Friedrichs, and H. Lewy (1928). „On the Partial Difference Equations of Mathematical Physics“. In: *Mathematische Annalen* 100, pp. 32–74.
- Gauto, A. (2023). *Deutschland nimmt die letzten Atomkraftwerke vom Netz*. Ed. by Handelsblatt.com. Last Access: 27.11.23. URL: <https://www.handelsblatt.com/unternehmen/energie/energie-deutschland-nimmt-die-letzten-atomkraftwerke-vom-netz/29085488.html>.
- Geckeis, H. (2017). *Retrieving waste from the Asse salt mine – facts and challenges*. Tech. rep. Karlsruhe Institute of Technology.
- Hindle, D. and J. Kley (2021). „The Subhercynian Basin: An example of an intraplate foreland basin due to a broken plate“. In: *Solid Earth* 12, pp. 2425–2438.
- Igel, H. (2017). *Computational Seismology*. 1st ed. Oxford University Press.
- K. Müller and U. Polom and J. Winsemann and H. Steffen and S. Tsukamoto and T. Günther and J. Igel and T. Spies and T. Lege and M. Frechen and H.-J.

- Franzke and C. Brandes (2020). „Structural style and neotectonic activity along the Harz Boundary Fault, northern Germany: a multimethod approach integrating geophysics, outcrop data and numerical simulations“. In: *International Journal of Earth Sciences* 109, pp. 1811–1835.
- Köhn, D. (2011). „Time Domain 2D Elastic Full Waveform Tomography“. PhD thesis. Kiel University.
- Köhn, D., D. De Nil, and A. Kurzmann (2005). *IFOS Manual*. Karlsruher Institut für Technologie und Christian-Albrechts- Universität Kiel.
- Komatitsch, D. and R. Martin (2007). „An unsplit convolutional Perfectly Matched Layer improved at grazing incidence for the seismic wave equation“. In: *Geophysics* 72, 1S0–Z83.
- Mendez, L. (2024). *Seismic Signatures of fluid pathways along the southern flank of the Asse salt structure*.
- Moczo, P., J. Robertson, and L. Eisner (2007). „The finite-difference time-domain method for modeling of seismic wave propagation“. In: *Advances in Geophysics* 48, pp. 421–516.
- Morse, P. (1953). *Methods of theoretical physics*. McGraw-Hill.
- Mortimore, R. and B. Pomerol (1997). „Upper Cretaceous tectonic phases and end Cretaceous inversion in the Chalk of the Anglo-Paris Basin“. In: *Proceedings of the Geologists' Association* 108, pp. 231–255.
- Müller, G. (2007). *Theory of Elastic Waves*. Tech. rep. Deutsches GeoForschungsZentrum.
- Nocedal, J. and S. Wright (2006). *Numerical Optimization*. 2nd ed. Springer.
- Peng, S., J. Tan, Z. Liu, X. Zhang, B. Liu, K. Yu, D. Xia J. Li, and C. Xie (2019). „Time-Domain Full Waveform Inversion Using the Gradient Preconditioning Based on Transmitted Wave Energy“. In: *Journal of Ocean University of China* 18, pp. 859–867.
- Plessix, R.-E. (2006). „A review of the adjoint-state method for computing the gradient of a functional with geophysical applications“. In: *Geophysical Journal International* 167, pp. 495–503.
- Plessix, R.-E. and W.-A. Mulder (2004). „Frequency-domain finite-difference amplitude-preserving migration“. In: *Geophysical Journal International* 157, pp. 975–987.
- Pollok, L., M. Saßnowski, T. Kühnlentz, V. Gundelach, J. Hammer, and C. Pritzkow (June 2018). „Geological exploration and 3D model of the Asse salt structure of SE expansion of the Asse II mine“. In: *Mechanical Behavior of Salt IX* 223, pp. 57–76.
- Pontius, M. (2016). *Joint acoustic full-waveform inversion and gravity inversion - development of synthetic application to a salt dome*.
- Pratt, R. and C. Shin (1998). „Gauss-Newton and full Newton methods in frequency-space seismic waveform inversion“. In: *Geophysical Journal International* 133(2), pp. 341–362.
- Ritter, J. (2020). „Inversion and Tomography“. Lecture Manual.
- Sahin, M., M. Ali, J. Park, and G. Destgeer (2023). „Fundamentals of Acoustic Wave Generation and Propagation“. In: *Acoustic Technologies in Biology and Medicine*, pp. 1–36.
- Sortan, S. (2022). *Effects of seismic anisotropy and attenuation on first-arrival waveforms recorded at the Asse ii nuclear repository*.
- Szymaniak, T. and M. Shaefer (2002). „Geologisch-tektonische Kartierung der Salzstruktur Asse im Subhercynen Becken“. In.

- T. Voigt and H. Eynatten and H.-J. Franzke (2004). „Late Cretaceous unconformities in the Subhercynian Cretaceous Basin“. In: *Acta geologica Polonica* 54(4).
- Tarantola, A. (1984). „Inversion of seismic reflection data in the acoustic approximation.“ In: *Geophysics* 49(8), pp. 1259–1266.
- (2005). *Inverse Problem Theory and Methods for Model Parameter Estimation*. SIAM.
- Thiel, N. (2013). *Imaging of subsalt structures with acoustic and elastic Full Waveform Inversion (FWI)*.
- Trela, J., V. Massaka, P. Pote, F. Bilgili, G. Gärtner, and L. Teichmann (Jan. 2018). „Quantum nodal system - Asse 3D survey success story“. In: *First Break* 39, pp. 61–68.
- Virieux, J. (1986). „p-sv wave propagation in heterogeneous media: Velocity-stress finite-difference method“. In: *Geophysics* 51, pp. 889–901.
- Virieux, J. and S. Operto (2009). „An overview of full-waveform inversion in exploration geophysics“. In: *Geophysics* 74(6), WCC1–WCC26.
- W. Voigt (1910). *Lehrbuch der Kristallphysik mit Ausschluss der Kristalloptik*. B.G. Teubner.

Appendix

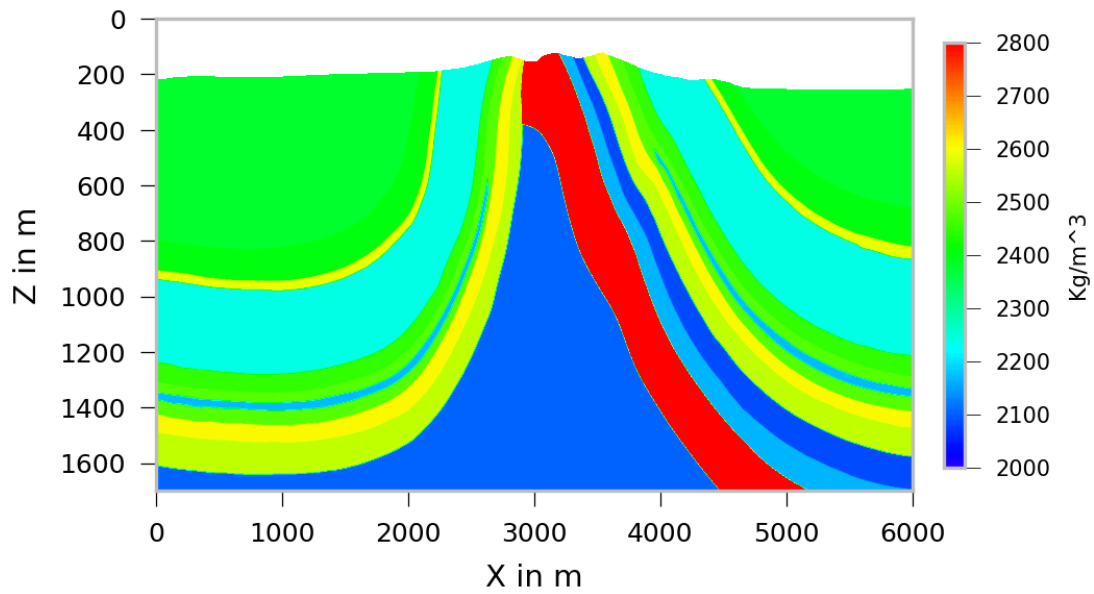


Figure A.1: The observed density model. It can be seen that the Bundsandstein on the northwestern flank of the Zechstein has a high density compared to the other geologic features.

Comparison of Different Density Starting Models

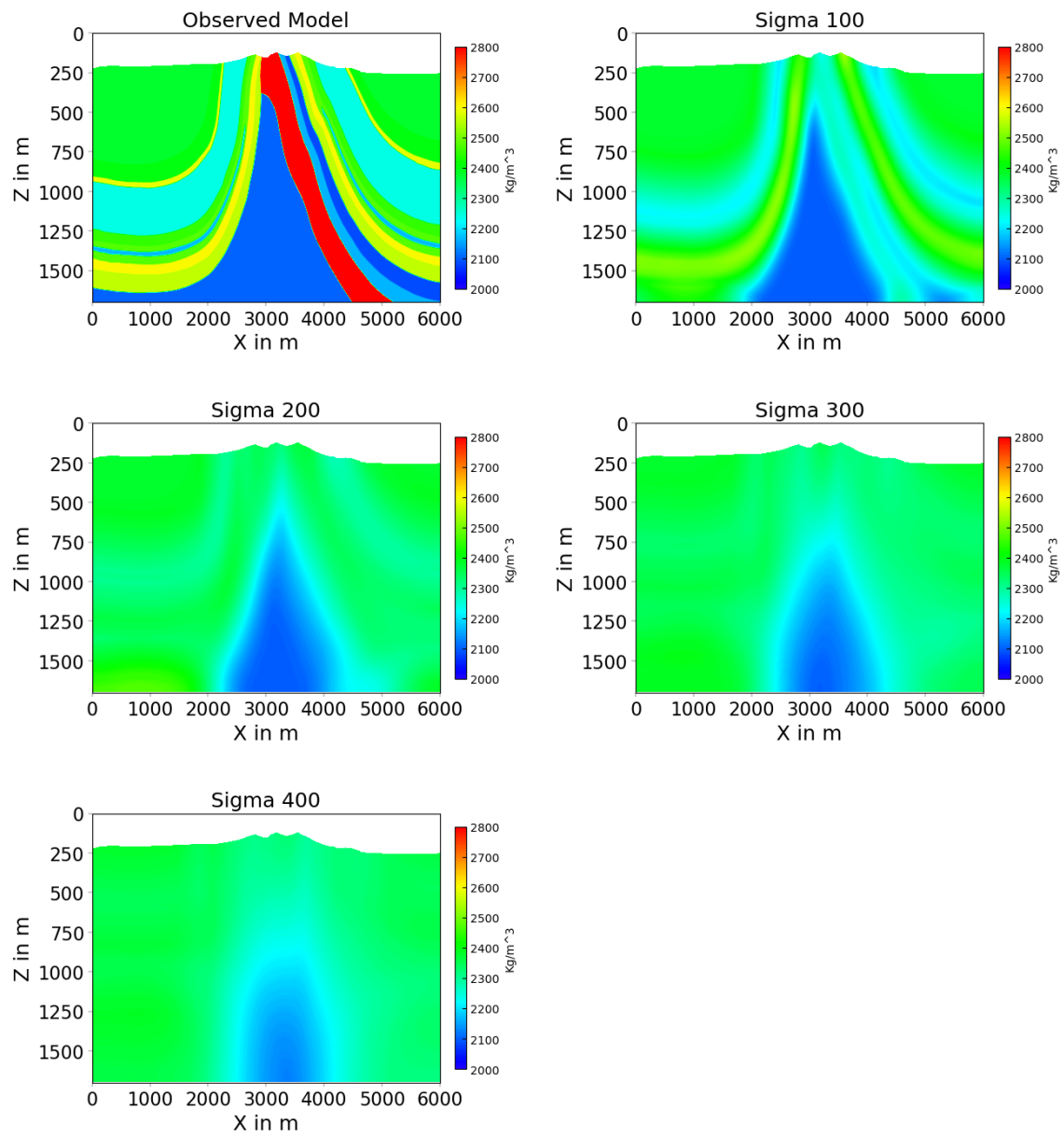


Figure A.2: A comparison of the starting models created from using different values of sigma in the Gaussian function for the density models. The observed model is shown as a comparison to display how the model changes due to smoothing.

Inversion Histograms of Different Starting Models

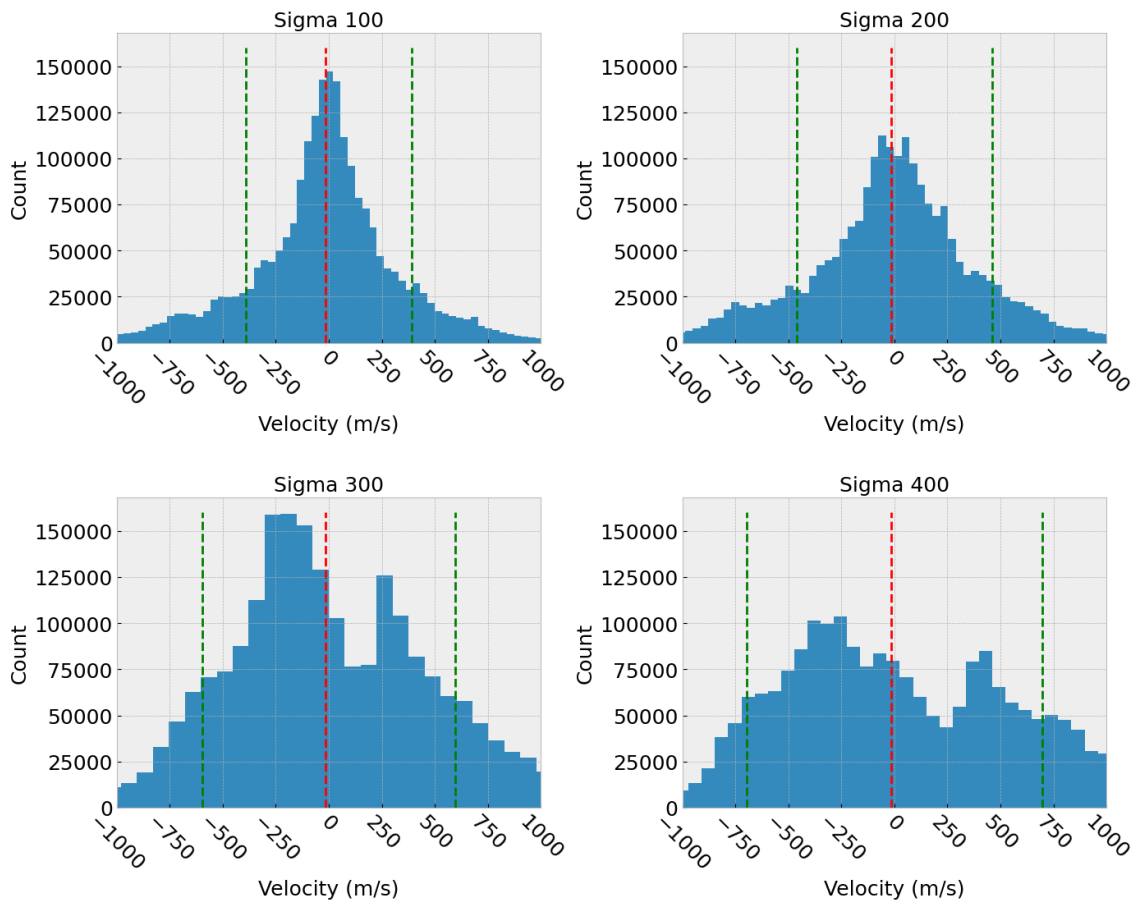


Figure A.3: Histograms of all inversions of the different starting models. The corresponding inversions can be found in figure 4.3. Sigma 100 and 200 show a normal distribution of the residuals.

Comparison of Different Shot Numbers

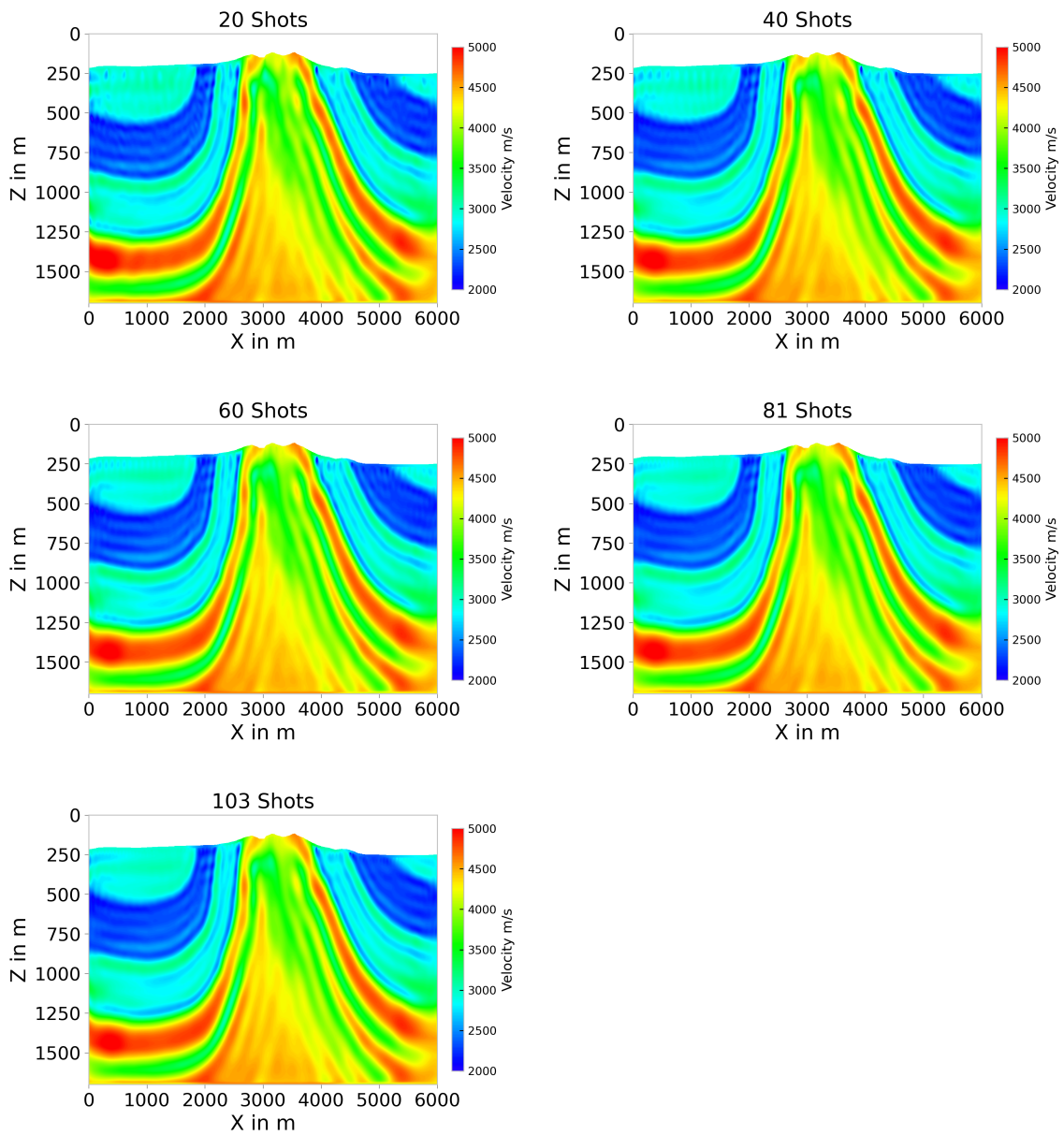


Figure A.4: All shot geometries tested are shown in this figure. These are 20, 40, 60, 81, and 103. Only the 20 shot and 103 shot models were shown in the main text of the thesis due to high level of similarity between the models.

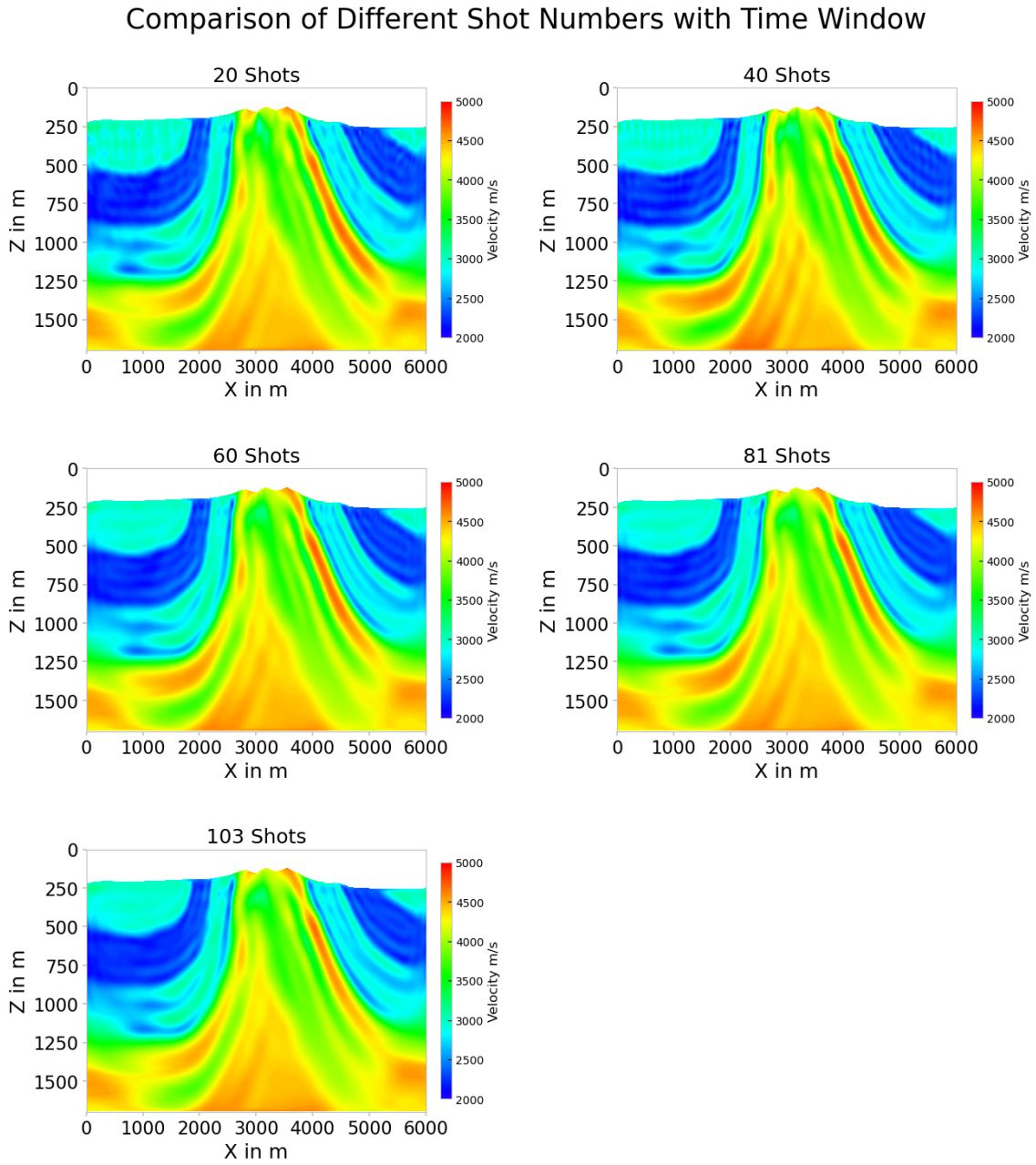


Figure A.5: All shot geometries with a time window tested are shown in this figure. These are 20, 40, 60, 81, and 103. Only the 20 shot and 103 shot models were shown in the main text of the thesis. The time windowed inversions show a higher percentage of improvement depending with higher shot geometries.

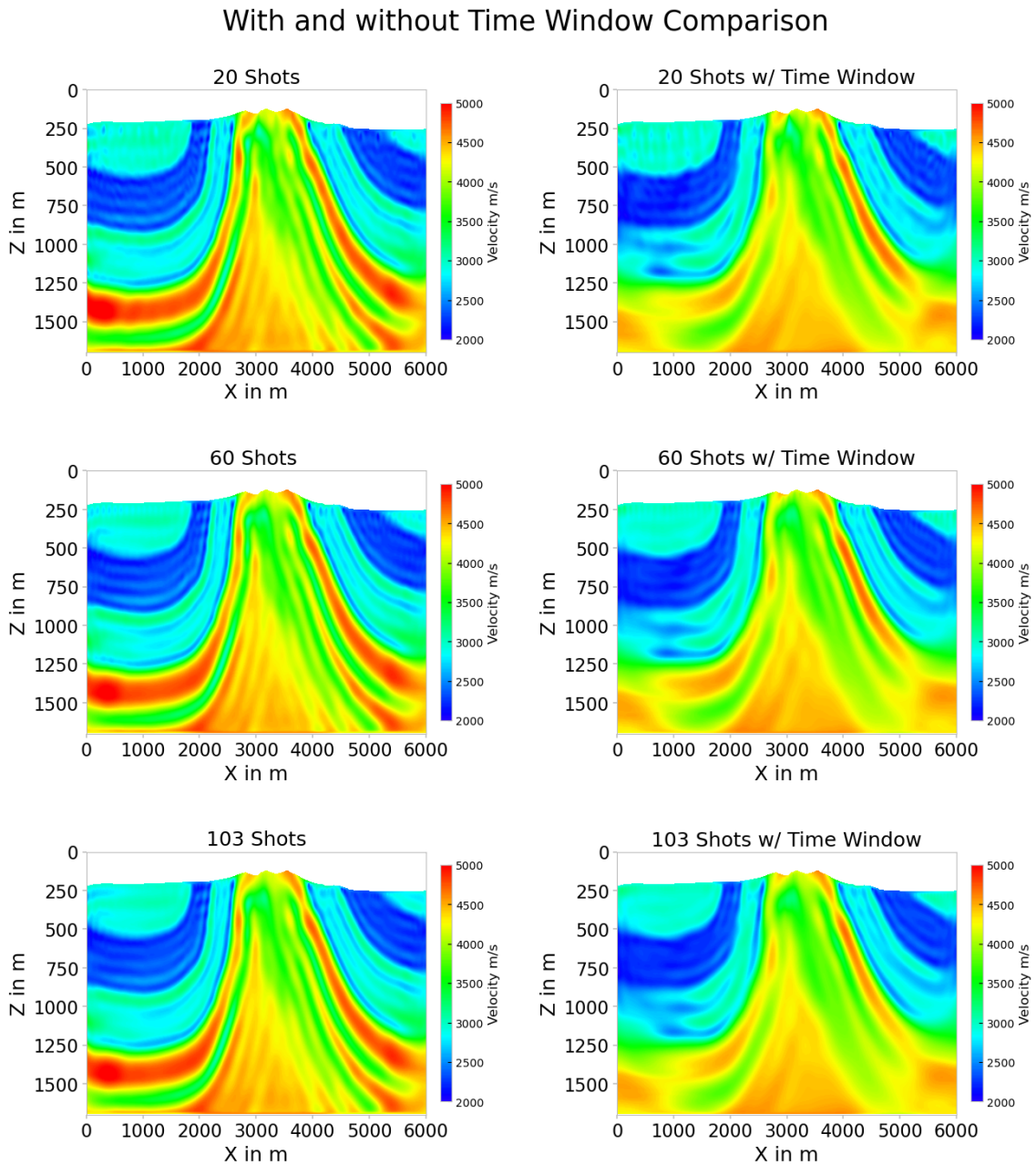


Figure A.6: A comparison between an inversion without and with a time window. Shown are the three different acquisition geometries: 20, 60, and 103 shots. The time windowed inversions all have poorer overall quality than the inversions without the time window. The increase in quality of the time windowed inversions due to a higher shot count is more clear than in the inversions without a time window.

Analysis of Sigma 300 Inversion

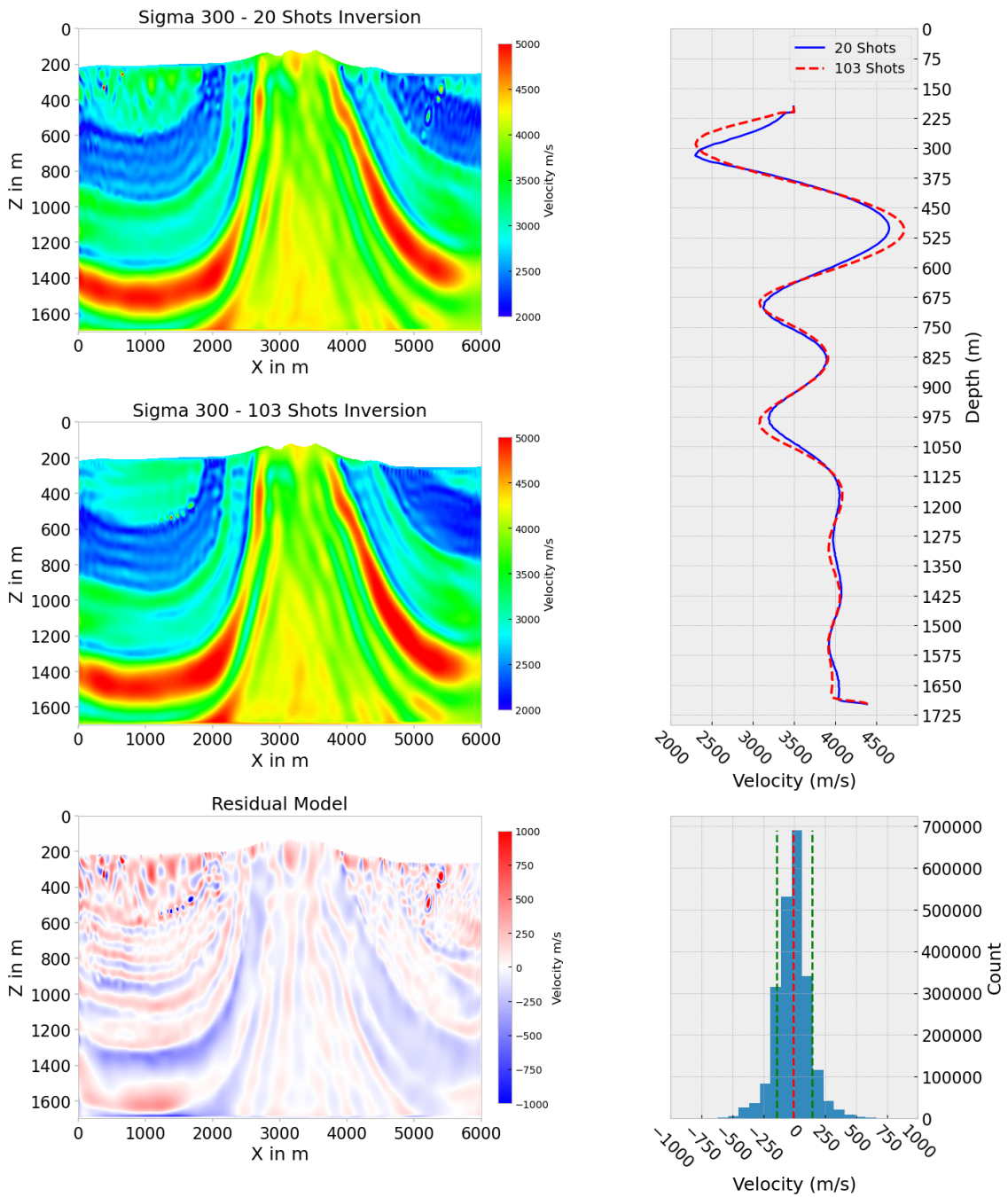


Figure A.7: A comparison between the observed synthetic model and a sigma 300 inversion without a time window. An acquisition geometry with 103 shots is shown. The residuals of the comparison are shown below the models. A histogram of the residuals, and a velocity profile at 4000 m is shown as well.